



SILESIAN UNIVERSITY OF TECHNOLOGY  
Faculty of Automatic Control, Electronics and Computer Science  
Institute of Automatic Control

## **Modelling and control of device casing vibrations for active reduction of acoustic noise**

Doctoral Dissertation

by

**Stanisław Wrona**

Supervisor  
**prof. dr hab. inż. Marek Pawełczyk**

June 2016  
Gliwice, POLAND

© 2016  
Stanisław Wrona  
All Rights Reserved

*To my Family*



# Abstract

Some of the most common noise sources in the human environment are devices and machinery. In an industrial scale, a high-level noise may lead to hearing losses and health problems. On the other hand, noise generated by domestic appliances do not represent a health threat, but may obstruct work or leisure. Passive methods are commonly applied to reduce the excessive device noise, however, they are ineffective for low frequencies and often are inapplicable due to increase of size and weight of the device and its potential overheating. When passive methods are exhausted, alternatively, active control methods can be applied. They efficiently complement the passive methods in their weak points—low-frequency noise and heat transfer problems.

The classical active noise control uses loudspeakers and microphones to reduce noise, but in three-dimensional space it often results in only local zones of quiet. In case of the device noise, global noise reduction is more desired. To obtain this goal, an active structural acoustic control can be applied, which uses vibrational inputs to reduce the actual noise emission. In the literature, such technique was successfully used for individual noise barriers. The objective of this dissertation is to extend this approach to whole device casings, hereinafter called an active casing approach.

To graduate the complexity, initially a rigid casing is examined, which limits the couplings between walls to the acoustic field. Then, a light-weight casing is considered, characterized by strong additional vibrational couplings. The introduced structures are analysed from the vibroacoustic and control-related point of view.

The mathematical model of the casing walls is developed and experimentally validated for a wide range of cases. The model unifies the mathematical formulation of various aspects that were dealt with separately in earlier works available in the literature. These include thin and thick plate theory, elastically restrained boundary conditions, thermoelastic damping model, and additional elements mounted to the casing surface—masses, ribs, actuators and sensors.

The developed model is widely used for a series of optimization problems. Starting with finding efficient locations for actuators and sensors based on controllability and observability measures. Then, a frequency response shaping method of casing walls is proposed. It is validated in both simulation and laboratory experiments.

Finally, the developed structures are used for active control experiments. The rigid casing is evaluated for single- and double-panels. Different error sensors are employed. The light-weight casing is examined utilizing the previous experiences to properly configure the control system. High levels of reduction are obtained, exceeding 20 dB of global noise reduction, what confirms a high practical potential of the developed approach. When examining different active control techniques, a set of recommendations is formulated for efficient implementation of the active casing method.



# Streszczenie

Maszyny i urządzenia są często dominującym źródłem hałasu w otoczeniu człowieka. W skali przemysłowej, wysoki poziom dźwięku może prowadzić do utraty słuchu lub innych problemów zdrowotnych. Urządzenia domowe również mogą być źródłem hałasu, choć nie charakteryzują się poziomem dźwięku, który wprost zagrażałyby zdrowiu. Mogą one jednak skutecznie utrudniać pracę lub wypoczynek. Częstym sposobem ograniczenia nadmiernego hałasu urządzeń są metody pasywne. Jednak są one nieskuteczne dla niskich częstotliwości. Często nie można ich też zastosować ze względu na nadmierne zwiększenie wymiarów i masy urządzenia, a także ryzyko przegrzania. Kiedy możliwości metod pasywnych zostają wyczerpane, alternatywnie zastosować można metody aktywne. Skutecznie uzupełniają one metody pasywne w ich najsłabszych punktach—niskim paśmie częstotliwości oraz problemach związanych z odprowadzaniem ciepła.

W klasycznej aktywnej redukcji hałasu stosowane są głośniki i mikrofony w celu osiągnięcia redukcji, jednak w przestrzeni trójwymiarowej często skutkuje to utworzeniem jedynie lokalnych stref ciszy. W przypadku hałasu urządzeń, redukcja globalna jest zdecydowanie bardziej pożądana. W tym celu można zastosować aktywną strukturalną redukcję hałasu, w której stosowane są wzbudniki drgań redukujące samą emisję akustyczną drgającej struktury. W literaturze znane są zastosowania tego podejścia dla pojedynczych barier. Celem niniejszej pracy jest rozszerzenie tego podejścia dla całych obudów urządzeń, dalej nazywając je metodą aktywnej obudowy.

Aby stopniować złożoność rozważanego problemu, początkowo badano ciężką obudowę o sztywnej konstrukcji szkieletowej, która ogranicza sprzężenia pomiędzy ścianami głównie do pola akustycznego. Następnie, rozważono lekką obudowę pozabawioną sztywnej ramy, która charakteryzuje się dodatkowo silnymi sprzężeniami vibacyjnymi. Przedstawione obudowy poddano analizie z punktu widzenia wibroakustyki i metod sterowania.

Wyprowadzono model matematyczny ścian obudowy, który następnie zweryfikowano eksperymentalnie dla szerokiej gamy przypadków. Model ten łączy opis matematyczny wielu zjawisk, które do tej pory w literaturze były rozpatrywane oddzielnie. Obejmują one teorie cienkich i grubych płyt, elastyczne warunki brzegowe, model tłumienia termoelastycznego, i obciążenie płyty dodatkowymi elementami—masami, usztywnieniami, elementami wykonawczymi i pomiarowymi.

Opracowany model wykorzystano dla szeregu różnych problemów optymalizacji. Najpierw dla optymalizacji rozmieszczenia elementów wykonawczych i pomiarowych, bazując na miarach sterowalności i obserwonalności układu. Następnie, zaproponowano metodę kształtowania odpowiedzi częstotliwościowej drgających płyt, którą zweryfikowano zarówno symulacyjne, jak i eksperymentalnie.

Przedstawione i zbadane obudowy zostały użyte w eksperymentach aktywnej redukcji. Obudowę sztywną zbadano w konfiguracjach ze ścianami jedno- i dwupanelowymi. Różne czujniki zostały wykorzystane, aby pozyskać sygnał błędu. Dla obudowy elastycznej wykorzystano wcześniejsze doświadczenia, aby właściwie skonfigurować obiekt. Osiągnięto wysokie poziomy redukcji, przekraczające 20 dB redukcji globalnej, co potwierdza wysoki potencjał metody do praktycznego zastosowania. Badając efektywność wielu metod sterowania, sformułowano wnioski i rekomendacje pomocne w efektywnej implementacji metody aktywnej obudowy.

# Acknowledgements

The author would like to thank Professor Marek Pawełczyk for his supervision, excellent support and guidance.

The author would also like to thank members of the Measurement and Control Systems Group for precious comments, hints and friendly atmosphere.

The research has been partially supported by the National Science Centre, Poland, decision no. DEC-2012/07/B/ST7/01408.

The greatest thanks are to my wife Natalia and my entire family for their huge support, patience and given motivation.



# Contents

<b>Abstract</b>	<b>v</b>
<b>Streszczenie</b>	<b>vii</b>
<b>Acknowledgements</b>	<b>ix</b>
<b>Contents</b>	<b>xi</b>
<b>List of Figures</b>	<b>xv</b>
<b>List of Tables</b>	<b>xxi</b>
<b>List of Abbreviations</b>	<b>xxiii</b>
<b>List of Symbols</b>	<b>xxv</b>
<b>1 Introduction</b>	<b>1</b>
1.1 Background . . . . .	1
1.2 Device and machinery noise . . . . .	1
1.3 Passive methods . . . . .	2
1.3.1 Device modification . . . . .	2
1.3.2 Additional passive components . . . . .	2
1.3.3 Personal protection . . . . .	3
1.4 Active methods . . . . .	3
1.4.1 Active Noise Control . . . . .	3
1.4.2 Active Structural Acoustic Control . . . . .	5
1.4.3 Active casing . . . . .	5
1.5 Motivation for the research . . . . .	6
1.6 Objective and thesis of the dissertation . . . . .	6
1.7 Contents of the dissertation . . . . .	6
<b>2 Laboratory setup</b>	<b>9</b>
2.1 Background . . . . .	9
2.2 Rigid casing . . . . .	9
2.2.1 Actuators and sensors . . . . .	10
2.2.2 Secondary paths analysis . . . . .	14
2.3 Light-weight casing . . . . .	14

2.3.1	Actuators and sensors . . . . .	16
2.3.2	Frequency response functions . . . . .	18
2.3.3	Secondary paths analysis . . . . .	19
2.4	Summary . . . . .	21
<b>3</b>	<b>Modelling of the device casings</b>	<b>23</b>
3.1	Background . . . . .	23
3.2	Vibration of individual plates . . . . .	24
3.2.1	Kirchhoff–Love plate theory . . . . .	24
Isotropic Kirchhoff plate	. . . . .	25
Orthotropic Kirchhoff plate	. . . . .	25
3.2.2	Mindlin–Reissner plate theory . . . . .	26
Isotropic Mindlin plate	. . . . .	27
Orthotropic Mindlin plate	. . . . .	28
3.3	Boundary conditions . . . . .	29
3.4	Additional elements . . . . .	32
3.4.1	Energy related to additional masses . . . . .	33
3.4.2	Energy related to ribs . . . . .	33
3.5	Total energy functional . . . . .	36
3.6	The Rayleigh–Ritz method . . . . .	36
3.6.1	Energy definition . . . . .	37
3.6.2	Stiffness matrix . . . . .	37
3.6.3	Mass matrix . . . . .	38
3.6.4	Equation of the vibrating structure and a harmonic solution . . . . .	38
3.7	State space model . . . . .	39
3.8	Controllability and observability . . . . .	41
3.9	Summary . . . . .	42
<b>4</b>	<b>Validation and analysis of the model</b>	<b>43</b>
4.1	Background . . . . .	43
4.2	Comparison with the individual plates . . . . .	43
4.2.1	Unloaded plate . . . . .	44
Isotropic thin plate with classical boundary conditions . . . . .	44	
Isotropic thick plate with classical boundary conditions . . . . .	44	
Isotropic plate with elastically restrained boundary conditions . . . . .	46	
Orthotropic plate . . . . .	48	
4.2.2	Plate loaded with additional elements . . . . .	49
Isotropic plate stiffened with ribs . . . . .	50	
Isotropic plate loaded with concentrated masses . . . . .	52	
4.3	Comparison for active casing walls . . . . .	54
4.3.1	Rigid casing walls . . . . .	54
Unloaded casing wall . . . . .	55	

Casing wall with additional mass . . . . .	57
Casing wall with inertial actuators . . . . .	57
Casing wall with ribs and additional masses . . . . .	61
4.3.2 Light-weight casing walls . . . . .	65
Unloaded casing walls . . . . .	67
4.4 Summary . . . . .	71
<b>5 Optimization process</b>	<b>73</b>
5.1 Background . . . . .	73
5.2 Memetic algorithm . . . . .	74
5.2.1 Comparison of evolutionary and memetic algorithms . . . . .	75
5.3 Identification of model boundary conditions . . . . .	76
5.3.1 Formulation of the optimization problem . . . . .	76
5.3.2 Cost function . . . . .	77
5.3.3 Preparation of experimental data . . . . .	77
5.3.4 Results . . . . .	77
5.4 Optimization of a vibrating structure . . . . .	78
5.4.1 Formulation of the optimization problem . . . . .	78
5.4.2 Cost function . . . . .	79
5.4.3 Actuators and sensors arrangement for the rigid casing . . . . .	80
5.4.4 Actuators and sensors arrangement for the light-weight casing .	82
5.4.5 Frequency response shaping method . . . . .	83
Minimization of the fundamental frequency . . . . .	85
Maximization of the fundamental frequency . . . . .	87
Setting natural frequencies at desired values . . . . .	88
Setting natural frequencies away from the given value . . . . .	89
Simultaneous optimization of arrangement of actuators, sensors, and passive elements . . . . .	90
5.5 Summary . . . . .	93
<b>6 Active control</b>	<b>95</b>
6.1 Background . . . . .	95
6.2 Adaptive feedforward control system . . . . .	96
6.2.1 Switched-error modification . . . . .	97
6.3 Active control of the rigid casing . . . . .	98
6.3.1 Experiments description . . . . .	98
6.3.2 Experiments results and discussion . . . . .	98
6.4 Active control of the light-weight casing . . . . .	105
6.4.1 Experiments description . . . . .	105
6.4.2 Experiments results and discussion . . . . .	108
6.5 Summary . . . . .	110

<b>7 Summary</b>	<b>111</b>
7.1 Conclusions . . . . .	111
7.2 Author's contribution . . . . .	112
7.3 Active casing project and motivation for future research . . . . .	112
<b>A Stiffness matrix elements</b>	<b>115</b>
<b>B Mass matrix elements</b>	<b>119</b>
<b>Bibliography</b>	<b>121</b>
<b>Index</b>	<b>129</b>

# List of Figures

1.1	Reproduced diagram from Paul Lueg's patent (Lueg, 1936). . . . .	4
2.1	A schematic representation of the rigid active casing. All dimensions are given in [mm]. . . . .	10
2.2	A photograph of the rigid active casing (Wrona and Pawelczyk, 2014b). . . . .	11
2.3	A schematic representation of the laboratory setup with the rigid active casing. All dimensions are given in [mm]. . . . .	11
2.4	Photographs of the rigid active casing with mounted sensors and actuators (Wrona and Pawelczyk, 2015). . . . .	12
2.5	Photographs of an actuator and sensors, along with their relevant parameters. . . . .	13
2.6	Exemplary amplitude responses of secondary paths for the rigid casing.	15
2.7	The light-weight active casing—a photograph and a schematic representation (Wrona and Pawelczyk, 2016d). All dimensions are given in [mm].	16
2.8	Photographs of the light-weight active casing with mounted sensors and actuators (Wrona and Pawelczyk, 2016b). . . . .	17
2.9	A schematic representation of the laboratory setup with the light-weight active casing. All dimensions are given in [mm]. . . . .	17
2.10	Spatially averaged frequency responses of casing walls. Two pairs of walls are symmetrical (left and right, front and back), hence only one of each pair is presented in the Figure. Initial 12 eigenmodes originating at each wall are marked: eigenmodes originating at left wall are marked with red circle, at front wall with blue diamond, at top wall with green square. . . . .	18
2.11	Exemplary amplitude responses of secondary paths for the light-weight casing. . . . .	20
3.1	A multiview orthographic projection of the rectangular plate with boundary conditions represented as rotational and translational springs. . . . .	31
3.2	Rectangular plate (1) with actuators (2), sensors (3), additional masses (4) and ribs (5) bonded to its surface—a visualization in an isometric projection. . . . .	32
3.3	Rectangular plate with the $i$ -th rib bonded to the plate surface, utilizing global and local coordinates systems. . . . .	34

4.1	Configuration of stiffened plate for comparisons with (Olson and Hazell, 1977), (Koko and Olson, 1992) and (Barrette et al., 2000). . . . .	50
4.2	The initial 6 eigenmodes shapes and frequencies calculated by the developed model for case 1a (size of the plate is in [m], and the z-axis depicts normalized amplitude). . . . .	52
4.3	The initial 7 eigenmodes shapes and frequencies calculated by developed model for case 2b (size of the plate is in [m], and the z-axis depicts normalized amplitude). . . . .	54
4.4	The laboratory setup with the laser vibrometer and the rigid casing used to measure modeshapes of the casing walls. . . . .	55
4.5	A comparison of initial 11 natural frequencies and modeshapes of rigid casing wall, calculated with the mathematical model and experimentally measured—1 mm thick aluminium unloaded plate. . . . .	56
4.6	A comparison of initial 11 natural frequencies and modeshapes of rigid casing wall, calculated with the mathematical model and experimentally measured—1 mm thick aluminium plate with an additional mass of $m_{m,1} = 0.080$ kg mounted at $x_{m,1} = 0.340$ m and $y_{m,1} = 0.340$ m. . . . .	58
4.7	A comparison of initial 12 natural frequencies and modeshapes of rigid casing wall, calculated with the mathematical model and experimentally measured—1 mm thick aluminium plate with an inertial actuator EX1 of mass $m_{a,1} = 0.115$ kg mounted at $x_{a,1} = 0.340$ m and $y_{a,1} = 0.340$ m. . . . .	59
4.8	A comparison of initial 12 natural frequencies and modeshapes of rigid casing wall, calculated with the mathematical model and experimentally measured—1 mm thick aluminium plate with three inertial actuators EX1 mounted to the surface. . . . .	60
4.9	A comparison of initial 12 natural frequencies and modeshapes of rigid casing wall, calculated with the mathematical model and experimentally measured—1 mm thick steel unloaded plate. . . . .	62
4.10	A comparison of initial 12 natural frequencies and modeshapes of rigid casing wall, calculated with the mathematical model and experimentally measured—1 mm thick steel plate with ribs and additional masses mounted to the surface. . . . .	63
4.11	The laboratory setup with the rigid casing to measure natural frequencies and modeshapes of the casing walls with ribs and additional mass mounted to the plate surface. . . . .	64
4.12	Experimentally measured frequency response of the plate (solid line—loaded plate; dashed line—unloaded plate) and visualization of additional elements mounted on the plate (circle—a mass; lines—ribs). . . . .	64
4.13	The laboratory setup with the laser vibrometer and the light-weight casing to measure modeshapes of the structure. . . . .	65

4.14	Three-dimensional visualization of experimentally measured modeshape of the whole light-weight casing, for an exemplary frequency of 155 Hz. All dimensions are given in [m]. . . . .	66
4.15	A comparison of initial 12 natural frequencies and modeshapes of the top wall of the light-weight casing, calculated with the mathematical model and experimentally measured. The red arrow marks well recognized modes selected for model fitting. . . . .	68
4.16	A comparison of initial 12 natural frequencies and modeshapes of the front wall of the light-weight casing, calculated with the mathematical model and experimentally measured. The red arrow marks well recognized modes selected for model fitting. . . . .	69
4.17	A comparison of initial 12 natural frequencies and modeshapes of the left wall of the light-weight casing, calculated with the mathematical model and experimentally measured. The red arrow marks well recognized modes selected for model fitting. . . . .	70
5.1	A memetic algorithm flowchart. . . . .	74
5.2	Multiple runs of optimization algorithms. . . . .	76
5.3	Results of the optimization. . . . .	81
5.4	Magnitudes of surface-averaged frequency responses of the plate due to excitation by individual actuators (the numbers in parentheses depict eigenfrequencies). . . . .	81
5.5	Arrangement of actuators on the light-weight casing walls. Two pairs of walls are symmetrical (left and right, front and back), hence only one of each pair is presented. . . . .	82
5.6	The frequency response of unloaded plate and visualization of additional elements mounted on the plate (there are no elements for the unloaded plate). . . . .	85
5.7	Results of optimization of cost function (5.12) for $N_m = N_r = 1$ . The frequency response of the plate (solid line - plate with elements; dashed line - unloaded plate) and visualization of additional elements mounted on the plate (circles - additional masses; lines - ribs). . . . .	86
5.8	Results of optimization of cost function (5.12) for $N_m = N_r = 2$ . The frequency response of the plate (solid line - plate with elements; dashed line - unloaded plate) and visualization of additional elements mounted on the plate (circles - additional masses; lines - ribs). . . . .	86
5.9	Results of optimization of cost function (5.13) for $N_m = N_r = 1$ . The frequency response of the plate (solid line - plate with elements; dashed line - unloaded plate) and visualization of additional elements mounted on the plate (circles - additional masses; lines - ribs). . . . .	87

5.10	Results of optimization of cost function (5.14) for $N_m = N_r = 3$ . The frequency response of the plate (solid line - plate with elements; dashed line - unloaded plate) and visualization of additional elements mounted on the plate (circles - additional masses; lines - ribs). . . . .	88
5.11	Results of optimization of cost function (5.15) for $N_m = N_r = 2$ . The frequency response of the plate (solid line - plate with elements; dashed line - unloaded plate) and visualization of additional elements mounted on the plate (circles - additional masses; lines - ribs). . . . .	90
5.12	Results of optimization of cost function (5.16) for $N_m = N_r = 2$ and $N_a = N_s = 1$ . The frequency response of the plate (solid line - plate with elements; dashed line - unloaded plate) and visualization of additional elements mounted on the plate (circles - additional masses; lines - ribs; circles with "X" inside - actuators; diamonds - sensors). . . . .	91
5.13	Results of optimization of cost function (5.16) for $N_m = N_r = 2$ and $N_a = N_s = 1$ . Values of the diagonal elements of the controllability and observability Gramian matrices. . . . .	91
5.14	Results of optimization of cost function (5.17) for $N_m = 2$ and $N_r = N_a = N_s = 3$ . The frequency response of the plate (solid line - plate with elements; dashed line - unloaded plate) and visualization of additional elements mounted on the plate (circles - additional masses; lines - ribs; circles with "X" inside - actuators; diamonds - sensors). . . . .	92
5.15	Results of optimization of cost function (5.17) for $N_m = 2$ and $N_r = N_a = N_s = 3$ . Values of the diagonal elements of the controllability and observability Gramian matrices. . . . .	92
6.1	Multi-channel feedforward control system with the FxLMS algorithm. . .	97
6.2	Time plots for the experiment performed for primary disturbance of 96 Hz and double-panel casing with ASAC algorithm. Microphones placed in cavities of the side walls and the outer top microphone were used as error sensors. . . . .	99
6.3	Frequency characteristics for the experiment performed for single-panel casing with ASAC algorithm. The outer microphones were used as error sensors. . . . .	100
6.4	Frequency characteristics for the experiment performed for single-panel casing with AVC algorithm. Accelerometers were used as error sensors. . . . .	101
6.5	Frequency characteristics for the experiment performed for double-panel casing with ASAC algorithm. Microphones placed in cavities of the side walls and the outer top microphone were used as error sensors. . . . .	102
6.6	Frequency characteristics for the experiment performed for double-panel casing with ASAC algorithm. The outer microphones were used as error sensors. . . . .	103

6.7	Frequency characteristics for the experiment performed for double-panel casing with AVC algorithm. Accelerometers were used as error sensors.	104
6.8	Comparison of mean reduction measured by room microphones. Frequency characteristics for experiments performed for single-panel casing.	105
6.9	Comparison of mean reduction measured by room microphones. Frequency characteristics for experiments performed for double-panel casing.	105
6.10	Time plots for the experiment performed for primary disturbance of 129 Hz and light-weight casing with ASAC-SE algorithm. The outer microphones were used as error sensors.	106
6.11	Frequency characteristics for the experiment performed for light-weight casing with ASAC algorithm. The outer microphones were used as error sensors.	107
6.12	Frequency characteristics for the experiment performed for light-weight casing with ASAC-SE algorithm. The outer microphones were used as error sensors.	108
6.13	Comparison of mean reduction measured by room microphones. Frequency characteristics for experiments performed for light-weight casing.	109



# List of Tables

3.1	Summary of different boundary conditions, depending on spring constants, at the exemplary plate edge $x = 0$ . The dashed line represents the reference state of the plate. . . . .	30
4.1	Frequency parameters $\lambda = \omega\sqrt{2(1+\nu)\rho_p a^2/E}$ for thin square <b>SSSS</b> plate: $h/a = \mathbf{0.01}$ , $\nu = 0.3$ , $\kappa = 0.822$ . . . . .	45
4.2	Frequency parameters $\lambda = \omega\sqrt{2(1+\nu)\rho_p a^2/E}$ for thin square <b>SCSC</b> plate: $h/a = \mathbf{0.01}$ , $\nu = 0.3$ , $\kappa = 0.822$ . . . . .	45
4.3	Frequency parameters $\lambda = \omega\sqrt{2(1+\nu)\rho_p a^2/E}$ for thin square <b>CCCC</b> plate: $h/a = \mathbf{0.01}$ , $\nu = 0.3$ , $\kappa = 0.860$ . . . . .	45
4.4	Frequency parameters $\lambda = \omega\sqrt{2(1+\nu)\rho_p a^2/E}$ for thin square <b>CCCF</b> plate: $h/a = \mathbf{0.01}$ , $\nu = 0.3$ , $\kappa = 0.860$ . . . . .	45
4.5	Frequency parameters $\lambda = \omega\sqrt{2(1+\nu)\rho_p a^2/E}$ for thick square <b>SSSS</b> plate: $h/a = \mathbf{0.1}$ , $\nu = 0.3$ , $\kappa = 0.822$ . . . . .	46
4.6	Frequency parameters $\lambda = \omega\sqrt{2(1+\nu)\rho_p a^2/E}$ for thick square <b>SCSC</b> plate: $h/a = \mathbf{0.1}$ , $\nu = 0.3$ , $\kappa = 0.822$ . . . . .	46
4.7	Frequency parameters $\lambda = \omega\sqrt{2(1+\nu)\rho_p a^2/E}$ for thick square <b>CCCC</b> plate: $h/a = \mathbf{0.1}$ , $\nu = 0.3$ , $\kappa = 0.860$ . . . . .	46
4.8	Frequency parameters $\lambda = \omega\sqrt{2(1+\nu)\rho_p a^2/E}$ for thick square <b>CCCF</b> plate: $h/a = \mathbf{0.1}$ , $\nu = 0.3$ , $\kappa = 0.860$ . . . . .	47
4.9	Frequency parameters $\lambda = \omega\sqrt{2(1+\nu)\rho_p a^2/E}$ for square plate with edges elastically restrained against rotation: $k_{rx0} = k_{rx1} = k_{ry0} = k_{ry1} = \mathbf{10D/a}$ , $h/a = 0.1$ , $\nu = 0.3$ , $\kappa = 0.822$ . . . . .	47
4.10	Frequency parameters $\lambda = \omega\sqrt{2(1+\nu)\rho_p a^2/E}$ for square plate with edges elastically restrained against rotation: $k_{rx0} = k_{rx1} = k_{ry0} = k_{ry1} = \mathbf{50D/a}$ , $h/a = 0.1$ , $\nu = 0.3$ , $\kappa = 0.822$ . . . . .	47
4.11	Frequency parameters $\lambda = \omega\sqrt{2(1+\nu)\rho_p a^2/E}$ for square plate with edges elastically restrained against rotation: $k_{rx0} = k_{rx1} = k_{ry0} = k_{ry1} = \mathbf{100D/a}$ , $h/a = 0.1$ , $\nu = 0.3$ , $\kappa = 0.822$ . . . . .	48
4.12	Frequency parameters $\lambda = \omega\sqrt{2(1+\nu)\rho_p a^2/E}$ for square plate with edges elastically restrained against rotation: $k_{rx0} = k_{rx1} = k_{ry0} = k_{ry1} = \mathbf{1000D/a}$ , $h/a = 0.1$ , $\nu = 0.3$ , $\kappa = 0.822$ . . . . .	48
4.13	Frequency parameters $\lambda = a^4\rho_p h \omega^2 / D_x$ for <b>graphite/epoxy</b> <b>SSCC</b> plate: $a/b = 0.833$ , $E_x = 185$ GPa, $E_y = 10.5$ GPa, $G_x = 7.3$ GPa, $\nu_x = 0.28$ , $\kappa = 0.860$ . . . . .	48

4.14 Frequency parameters $\lambda = a \sqrt[4]{\rho_p h \omega^2 / D_x}$ for <b>graphite/epoxy SCCC</b> plate: $a/b = 0.833, E_x = 185 \text{ GPa}, E_y = 10.5 \text{ GPa}, G_x = 7.3 \text{ GPa}, \nu_x = 0.28,$ $\kappa = 0.860.$ . . . . .	49
4.15 Frequency parameters $\lambda = a \sqrt[4]{\rho_p h \omega^2 / D_x}$ for <b>graphite/epoxy CCCC</b> plate: $a/b = 0.833, E_x = 185 \text{ GPa}, E_y = 10.5 \text{ GPa}, G_x = 7.3 \text{ GPa}, \nu_x = 0.28,$ $\kappa = 0.860.$ . . . . .	49
4.16 Frequency parameters $\lambda = a \sqrt[4]{\rho_p h \omega^2 / D_x}$ for <b>boron/epoxy CCCC</b> plate: $a/b = 0.5, E_x = 208 \text{ GPa}, E_y = 18.9 \text{ GPa}, G_x = 5.7 \text{ GPa}, \nu_x = 0.23,$ $\kappa = 0.860.$ . . . . .	49
4.17 Natural frequencies for case 1a (Hz). . . . .	51
4.18 Natural frequencies for case 1b (Hz). . . . .	51
4.19 Fundamental frequencies of the plate with an additional mass, case 2a (Hz). . . . .	53
4.20 Natural frequencies for case 2b (Hz). . . . .	54
5.1 Comparison of characteristic values. . . . .	76
5.2 Natural frequencies of unloaded plate. . . . .	85
5.3 Results of optimization of cost function (5.12) for $N_m = N_r = 1$ . Natural frequencies of the plate and placement of additional elements. . . . .	85
5.4 Results of optimization of cost function (5.12) for $N_m = N_r = 2$ . Natural frequencies of the plate and placement of additional elements. . . . .	86
5.5 Results of optimization of cost function (5.13) for $N_m = N_r = 1$ . Natural frequencies of the plate and placement of additional elements. . . . .	87
5.6 Results of optimization of cost function (5.14) for $N_m = N_r = 3$ . Natural frequencies of the plate and placement of additional elements. . . . .	88
5.7 Results of optimization of cost function (5.15) for $N_m = N_r = 2$ . Natural frequencies of the plate and placement of additional elements. . . . .	89
5.8 Results of optimization of cost function (5.16) for $N_m = N_r = 2$ and $N_a =$ $N_s = 1$ . Natural frequencies of the plate and placement of additional elements. . . . .	91
5.9 Results of optimization of cost function (5.17) for $N_m = 2$ and $N_r = N_a =$ $N_s = 3$ . Natural frequencies of the plate and placement of additional elements. . . . .	92

# List of Abbreviations

<b>ANC</b>	Active Noise Control
<b>ASAC</b>	Active Structural Acoustic Control
<b>ASAC-SE</b>	Active Structural Acoustic Control with Switched-Error modification
<b>AVC</b>	Active Vibration Control
<b>EA</b>	Evolutionary Algorithm
<b>FEM</b>	Finite Elements Method
<b>FIR</b>	Finite Impulse Response
<b>FxLMS</b>	Filtered-x Least Mean Squares
<b>IMC</b>	Internal Model Control
<b>LMS</b>	Least Mean Squares
<b>LNFxLMS</b>	Leaky Normalised Filtered-x Least Mean Squares
<b>MA</b>	Memetic Algorithm
<b>MFC</b>	Macro Fiber Composite
<b>PVDF</b>	PolyVinylidene DiFluoride
<b>PZT</b>	lead zirconate titanate ( $\text{Pb}[\text{Zr}_x\text{Ti}_{1-x}]\text{O}_3$ )
<b>VMC</b>	Virtual Microphone Control



# List of Symbols

$a$	length of the plate
$A_{r,i}$	cross-sectional area of the $i$ -th rib
<b>A</b>	state matrix
$b$	width of the plate
<b>B</b>	control matrix
<b>C</b>	output matrix
<b>D</b>	feedthrough matrix
$D_x, D_y, D_{xy}$	bending/twisting rigidities of the plate
$E_x, E_y$	Young moduli of the plate
$E_{r,i}$	Young modulus of the $i$ -th rib
$f_i$	force generated by a $i$ -th actuator
$G_{xy}, G_{xz}, G_{yz}$	shear moduli of the plate
$G_{r,i}$	shear modulus of the $i$ -th rib
$h$	plate thickness
$I_{ax,i}, I_{sx,i}, I_{mx,i},$ $I_{ay,i}, I_{sy,i}, I_{my,i}$	moments of inertia of the $i$ -th actuator, sensor and additional mass
$I_{r,i}$	second moment of inertia about the plate mid-plane of the $i$ -th rib
$J_{r,i}$	torsional constant of the $i$ -th rib
$k_{tx0}, k_{tx1},$ $k_{ty0}, k_{ty1}$	translational spring constants
$k_{rx0}, k_{rx1},$ $k_{ry0}, k_{ry1}$	rotational spring constants
$k_{r,i}$	radius of gyration of the $i$ -th rib
<b>K</b>	stiffness matrix
$m_{a,i}, m_{s,i}, m_{m,i}$	mass of the $i$ -th actuator, sensor and additional mass, respectively
<b>M</b>	mass matrix
$N$	number of Ritz functions
$N_a, N_s, N_m, N_r$	number of actuators, sensors, additional masses and ribs
<b>q</b>	generalized plate displacement vector
$\mathbf{p}_x, \mathbf{p}_y$	generalized plate rotations vectors
<b>Q</b>	vector of generalized forces
$t$	time
$T$	overall kinetic energy of the system
$T_m, T_p, T_r$	kinetic energy of additional masses, plate and ribs

<b>u</b>	control vector
$U$	overall potential energy of the system
$U_b, U_p, U_r$	potential energy corresponding to elastic boundary restraints, plate and ribs
<b>v</b>	modal displacement vector
$w(x, y, t)$	plate transverse displacement
$\mathbf{W}_c, \mathbf{W}_o$	Gramian matrices of controllability and observability, respectively
<b>y</b>	output vector
$i, j, k$	positive integers
$(x, y)$	global coordinates
$(\tilde{x}_{r,i}, \tilde{y}_{r,i})$	local coordinates, corresponding to $i$ -th rib
$(\xi, \eta)$	non-dimensional global coordinates
$\alpha_p$	non-dimensional parameter equal $\frac{a}{b}$
$\beta_{r,i}$	shape factor of the $i$ -th rib
$\Theta_x(x, y, t),$ $\Theta_y(x, y, t)$	cross-sectional rotations of the plate
$\kappa_x, \kappa_y$	shear coefficients of the plate
$\nu_x, \nu_y$	Poisson ratios of the plate
<b>E</b>	Damping matrix
$\xi_{d,i}$	Damping ratio of $i$ -th eigenmode
$\rho_p$	mass density of the plate material
$\rho_{r,i}$	mass density of the $i$ -th rib
$\phi, \psi_x, \psi_y$	trial functions vectors
<b>Φ</b>	eigenvector matrix
<b>Ω</b>	eigenfrequency matrix
$\omega_i$	$i$ -th eigenfrequency

# **Chapter 1**

## **Introduction**

### **1.1 Background**

Acoustic noise has been defined as "sound which is undesired by the recipient" (IEC 60050-801, 1994) and it is consequently a subjective notion. What is sound to one person, it can very well be noise to somebody else, although from the acoustics point of view, sound and noise is the same phenomenon of atmospheric pressure fluctuations about the mean value.

The noise is a natural consequence of almost everything that people do. Usually it is not perceived by them, or at least tolerated. Nevertheless, it has been considered as an issue since ancient times. First documented noise ordinance dates back to the 6th century BC, when the council of the province of Sybaris, a Greek colony, decreed that potters, tinsmiths, and other tradesmen must live outside the city walls because of the noise they make (Goldsmith, 2012). One of the earliest attempts to define noise regulation policy in the modern era dates back to 1929, when the Noise Abatement Commission was established in New York. Since then, many other attempts have been made to use legal instruments for noise regulation (Wolf and Stanley, 2013).

Alongside the technological development the amount of noise sources in the human environment is constantly growing, making the problem of noise pollution highly important and better noticed. Also, the tendency towards lightweight solutions makes the problem of excessive noise more frequent. People are becoming aware of the negative consequences of prolonged exposure to noise and more often seek to reduce it (Wolf and Stanley, 2013).

### **1.2 Device and machinery noise**

One of the kinds of noise that is of particular interest in the present work, is the noise generated by devices and machinery. It can be a significant issue for their users. In an industrial scale (like in case of factories, electricity plants, etc.), high-level noise or prolonged exposure can lead to hearing damage (Talbot-Smith, 2013). Noise often causes exasperation, negatively affects the nervous system, and as shown by a recent studies, it affects even a clarity of vision (Lin, 2014). In industrial environments noise is frequently a cause of difficulties in communication between staff, thereby reducing the

efficiency of the work performed. The inability to hear alarms or sounds associated with the work of other devices significantly increases the risk of an accident. The exceeding of current noise regulations results in the necessity to reduce working time, thereby increasing the costs.

Household appliances can also be a source of noise. Although it is not characterized by the sound pressure level which can lead to hearing damage, it causes annoyance and significantly obstructs work or leisure. Also, the noise level is gaining significance as a criterion in product selection by the consumers.

In order to reduce the noise emitted by devices and machinery, many techniques have been developed, which can be broadly classified into passive and active control methods.

## **1.3 Passive methods**

Passive methods are mainly characterized by the fact that they do not require any external source of energy. Among the passive methods, several main approaches can be distinguished.

### **1.3.1 Device modification**

The best practice to reduce noise is to act directly at the source. Noise and vibration issues should be always integrated in the design of a device, as then there are more options available to make the final product quieter. Modification of assembled, working devices and machinery is much more complicated and expensive (Crocker, 2007). However, device modification alone is insufficient in many cases, as apart from some benefit, further improvement requires too far-going redesign of the device, which is very expensive or even infeasible, and may degrade its other parameters.

### **1.3.2 Additional passive components**

Together with the modification of the device, additional passive components can be employed to improve the sound quality. If the emitted noise is mainly a structure-borne sound, excessive vibrations can be treated in the first place. Vibration isolators are used to reduce the vibratory forces or motions that are transmitted from one structure or component to another. Also damping materials can be added to increase dissipation of energy in vibrations. On the other hand, additional components can be added that directly affects the paths of noise transmission to the environment. Sound-absorbing materials are used to absorb most of the sound energy striking them and convert it into the heat. Also sound-insulating barriers can be employed to reflect the incident sound energy back toward the source.

Aforementioned components, often combined, provide an acceptable solution to many noise problems. However, their effectiveness is mostly limited to high frequencies (Nelson and Elliott, 1993). Moreover, such passive components are often inapplicable due to increase in size and weight of the device, and its potential overheating related to high thermal insulation properties of many materials mentioned.

### 1.3.3 Personal protection

When all other possibilities are exhausted, personal passive means of protection can be employed. Earplugs, earmuffs or even complete personnel enclosures are used to mitigate the impact of excessive noise in the areas where humans have to be present.

However, such means of protection often limit the ability to work effectively and are simply inconvenient to device users or workers. Moreover, they possess a major disadvantage that the wanted sound is also reduced, including communication and possible alarm signals (unless active personal hearing protectors are used that supports verbal communication (Engel et al., 2001; Latos, 2011)).

## 1.4 Active methods

An alternative way to reduce noise is to use active control methods, which can be explained by the principle of superposition, acoustic energy absorption or acoustic impedance modification. In contrast to passive methods, additional energy is introduced to the system through a set of control inputs to obtain a secondary response that adds to the primary disturbance field. In result, the total response of the system can be reduced (destructive interference) or altered in the desired manner.

Typically, active control systems consist of a set of sensors and actuators, and an electronic controller, which drives actuators, basing on sensor signals. The controller often runs in an adaptive way to follow changes in the primary disturbance field. Active control is especially effective for the low-frequency noise, where passive methods are insufficient (Preumont, 2012). Hence, the complementary use of active and passive methods is an attractive solution. Alternatively, passive components can be replaced with an appropriate active control system to reduce the weight or size of the device, or to improve heat exchange capabilities.

### 1.4.1 Active Noise Control

The active control approach was first proposed in the 1930s, when Paul Lueg patented a method to reduce sound with an additional sound (Lueg, 1936). His idea is illustrated in Fig. 1.1. The noise source  $A$  produces a sound wave  $S_1$ , which propagates downstream from left to right. The noise is measured in advance by a microphone  $M$ , it is later processed by an electronic controller  $V$  and drives a loudspeaker  $L$ . If the control system operates correctly, the loudspeaker produces a sound wave  $S_2$  identical

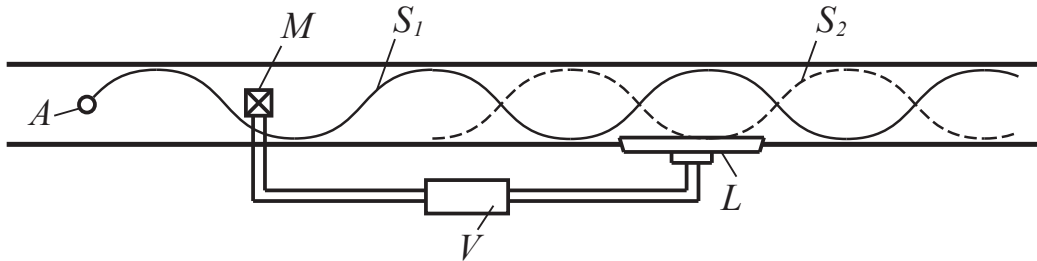


Figure 1.1: Reproduced diagram from Paul Lueg's patent (Lueg, 1936).

in amplitude and opposite in phase ( $180^\circ$  difference) to  $S_1$ , cancelling the the original wave. It was a classical feed-forward Active Noise Control (ANC) system.

In 1950s, Olson proposed an electronic sound absorber using a feedback control (Olson and May, 1953). He employed a collocated microphone and loudspeaker to produce a "zone of silence" around the microphone. Two years later, Conover proposed sound cancellation to reduce noise from a transformer (Conover and Ringlee, 1955).

Although the principles of ANC has been known, those analogue controllers did not allow to develop truly practical solutions. It was not until the the 1980s, when with the introduction of an adaptive digital filter (Burgess, 1981; Roure, 1985) and the Filtered-x Least Mean Squares (FxLMS) algorithm (Morgan, 1980; Widrow and Stearns, 1985), the active control became more feasible and modern methods for ANC were developed (Nelson and Elliott, 1993; Hansen et al., 2012).

Since then, there has been considerable interest in the commercial application of active noise control (Morzynski and Makarewicz, 2003; Krukowicz, 2013). Some of the already available products are active headrests or headsets (e.g. by Bose, Sennheiser or Silentium), active Heating, Ventilation, and Air Conditioning (HVAC) system add-ons (e.g. by Silentium), or active system to reduce car engine noise and road noise in the vehicle cabin (e.g. by Lotus Engineering and Harman).

However, classical ANC in three-dimensional enclosures encounters many problems related to complicated physical phenomena, generation of local zones of quiet instead of global reduction, high interference with the enclosure, and very high power consumption. It is especially troublesome, when the noise source is distributed over multiple surfaces, as in case of structure-borne sound emitted by devices and machinery (e.g. by vibrating plates, walls or casings). Then, numerous loudspeakers and microphones are required to provide global noise reduction, which is infeasible for many practical application. Alternatively, control inputs (e.g. mechanical shakers or piezoelectric actuators) can be applied directly to the vibrating structure responsible for the sound radiation/transmission. This technique is referred to as Active Structural Acoustic Control (ASAC) and it was introduced by Fuller in late 1980s (Jones and Fuller, 1989; Fuller, 1990). In such approach the sound propagating both in air and in structures have to be considered jointly. The field that consider all vibration and acoustic phenomena together is called "vibroacoustics" (Engel, 2010) or "structural acoustics" in the US (Fahy and Gardonio, 2007).

### 1.4.2 Active Structural Acoustic Control

The ASAC approach derives partially from both the ANC and Active Vibration Control (AVC) methods, which were developed in parallel to ANC. ASAC aims to reduce or change vibration distribution in order to minimize sound pressure or a pressure-related variable. In contrast to AVC that aims at vibration reduction to the best possible extent, with no concern regarding the overall sound, ASAC focuses only on vibrations that are related to sound radiation. In some cases, overall vibration magnitude can be even amplified if it result in reduced noise radiation. The frequency range of interest is also much higher, than typically in AVC.

If the ASAC approach can be applied, it is characterized by several advantages over classical ANC to globally reduce the noise emitted by devices: (i) it requires generally a lesser number of control inputs (Mao and Pietrzko, 2013), (ii) it consumes less energy, and (iii) control inputs are integrated into the vibrating structure, which is more feasible than using loudspeakers. Under certain circumstances, as e.g. in Virtual Microphone Control (VMC) technique, sensors can be integrated also, instead of using microphones (Pawelczyk, 2004). These features makes the ASAC approach well fitted to solve the problem of excessive noise generated by devices and machinery.

The first applications of ASAC considered a sound radiated by a single plate or cylindrical structure (Fuller, 1990; Fuller et al., 1991). It was applied also for double-panel structures, e.g. double glazed windows (Kaiser, 2001; Pietrzko, 2009). Applications of such active barriers were considered for vehicle cabin, air plane fuselage or ship hull (Liu et al., 2006; Carneal and Fuller, 2004; Keir et al., 2005). However, there is a lack of reports in the literature, nor commercial products concerning active control of multiple walls of a structure (e.g. device casing) to reduce the emitted noise.

### 1.4.3 Active casing

In cases, where a device generating noise is surrounded by a thin-walled casing, or if it can be enclosed in an additional casing, such structure as a whole can be used as a barrier for ASAC system application to enhance acoustic isolation of the device. When appropriately implemented, it results in a global noise reduction instead of local zones of quiet. Such solution does not require structural modifications of the device nor affects its regular operations, but it allows to enclose the source of noise inside the casing, isolating it acoustically from the environment. Given advantages constituted a motivation to undertake and develop in this dissertation a technique that is referred to as active casing approach.

## **1.5 Motivation for the research**

For numerous environments, structurally radiated noise from devices and machinery is a persistent problem. The active casing approach is a highly interesting alternative if passive methods are either ineffective or unfeasible. The active casing method allows a device to maintain original heat transfer capabilities. Additionally, it preserves the original size and weight of the device.

Moreover, this approach can also be used in cooperation with other means of noise reduction. If the device needs to possess ventilation channels, additional ANC systems can be applied to avoid acoustic leakage through the openings. On the other hand, to deliver a highest acoustical isolation, an active casing system can be applied together with passive sound-insulating material.

Considering mentioned above advantages, a high practical potential of the active casing method is clearly visible. It is also an important topic from the scientific point of view, because there are no previous research in the literature, known to the author, that would consider an active control of entire device casings.

## **1.6 Objective and thesis of the dissertation**

The objective of this dissertation is to develop the concept of active casing, as a way to reduce noise generated by devices and machinery. The main thesis is formulated as:

**It is possible to reduce vibrations of device casing walls by the passive method with optimally arranged additional masses and ribs mounted to the casing walls, and to decrease globally device noise emission to the environment by the active method with optimally arranged vibration actuators and sensors.**

## **1.7 Contents of the dissertation**

This dissertation consists of seven chapters. The first chapter contains the introduction.

In Chapter 2 the laboratory setup for active control experiments, consisting of several different device casings is discussed. To graduate the complexity, initially a rigid casing is considered, which limits the cross couplings between walls. Then, a light-weight casing is undertaken, characterized by strong vibrational coupling between the casing walls. The discussion includes practical application-related aspects of the laboratory stand assembly, vibroacoustic analysis of the introduced structures based on secondary paths and frequency response functions, and selection of sensors and actuators for the active control systems.

In Chapter 3 the mathematical model of the device casing walls is developed. The model includes thin and thick plate theory, elastically restrained boundary conditions,

structural thermoelastic damping model, and additional elements mounted to the casing surface—masses, ribs, actuators and sensors. These aspects are integrated in a feasible state space model form, which facilitates further analysis. The measures of controllability and observability of the system are also considered.

In Chapter 4 the developed model of a casing wall is validated by means of a comparison with the examples known from literature and laboratory experiments performed by the author. The comparison includes natural frequencies, modeshapes and frequency response functions. Among multiple results of simulation and experiments, the laboratory measurement procedure is also described.

In Chapter 5 the developed model is widely used for a series of optimization problems. The memetic algorithm is used as an effective optimization algorithm for problems with complex search spaces and multiple local optima. Initially, a method of identification of model boundary conditions is proposed and practically evaluated, utilizing experimental data and the memetic algorithm. Then, the optimization algorithm is employed to find efficient locations for actuators and sensors based on controllability and observability measures. Finally, a frequency response shaping method of casing walls is proposed. It is validated for a set of passive and active control scenarios, including both simulation and a laboratory experiment.

In Chapter 6 utilizing the previous analysis and considerations, the developed structures are used to perform active control experiments. Initially, the rigid casing is evaluated for single- and double-panel configurations. Different sensors are employed to provide the error signals. Then, the light-weight casing is examined, utilizing the previous experiences to properly configure the control system. The obtained results are presented and discussed to formulate a set of recommendations for efficient implementation of the active casing approach.

In Chapter 7 conclusions, author's contribution and an outlook are presented.

In Appendix A definitions of elements of stiffness submatrices are given.

In Appendix B definitions of elements of mass submatrices are provided.



# Chapter 2

## Laboratory setup

### 2.1 Background

The performed research is divided into two main stages. Each of them is characterised by an investigated vibrating structure.

In the first research stage, the *rigid casing* is evaluated (see Section 2.2), since the employed heavy frame limits vibrational couplings between walls, facilitating initial attempts to control their vibrations. Moreover, the structure is designed to be easily reconfigurable, enabling experiments with different panel materials, thickness, and single- or double-panel walls.

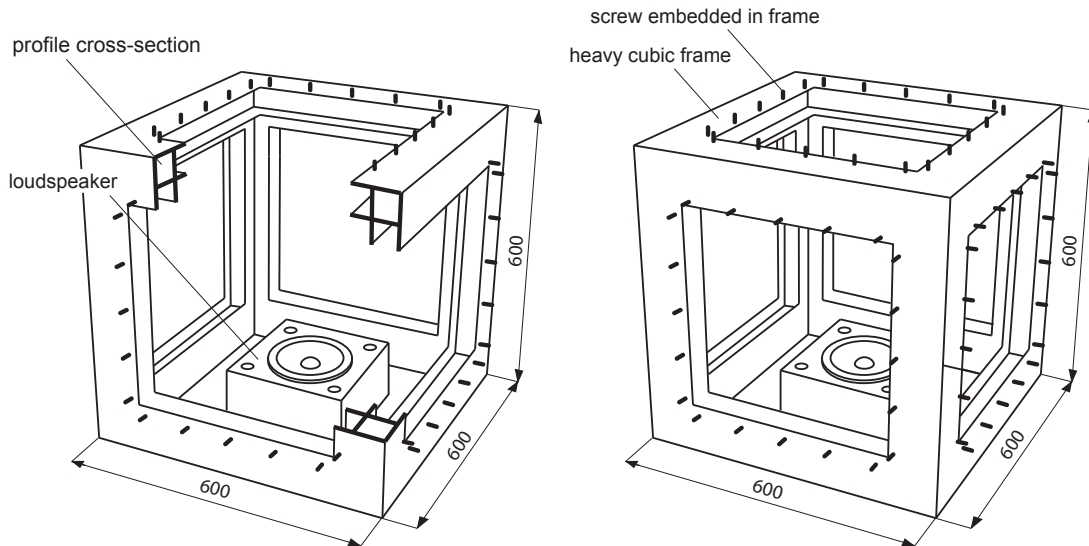
In the second stage, the *light-weight casing* is used (see Section 2.3), which in contrast to previously employed structure, is made without an explicit frame, resulting in greater vibrational couplings. The casing is made of metal plates bolted directly together, therefore the structure is not reconfigurable. However, several versions of different plate thickness and geometrical dimensions are prepared.

Each of aforementioned casings is described in this Chapter, starting with details of a mechanical structure. Then, selection and arrangement of applied actuators and sensors are discussed. Finally, vibroacoustical analysis of the structures based on secondary paths and frequency response functions is presented.

### 2.2 Rigid casing

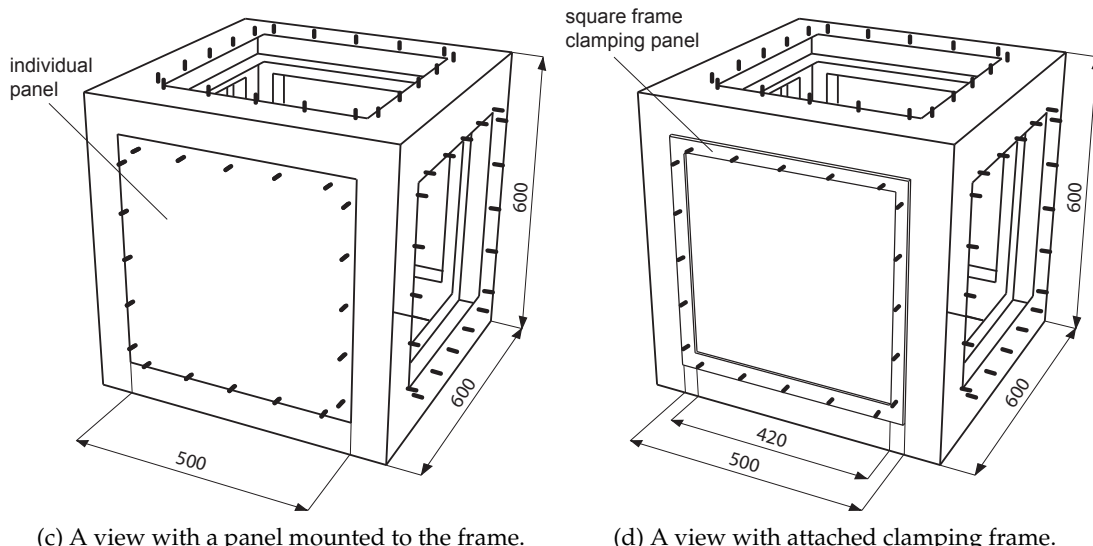
The rigid casing discussed in this Section is presented in Fig. 2.1, where dimensions, cross-sections and the method of mounting of casing walls are visualised. A photograph of the casing is given in Fig. 2.2. The casing has a heavy cubic frame made of 3 mm thick welded steel profiles. The high rigidity of the frame results in its resonance frequencies to be far above frequencies of the noise considered. The bottom of the casing is vibrationally and acoustically insulated. All walls of the casing are made of single or double panels. Each panel is attached to the structure by 20 screws embedded in the frame, and clamped with an additional steel square frame. Fully-clamped boundary conditions can be then assumed for the panels, achieving satisfactory modelling accuracy. For double panels the distance between them is 50 mm. The

panel closer to the casing interior is called the *incident panel*, and the outer panel is referred to as the *radiating panel* (Pietrzko, 2009). To avoid unobservable resonances in the cavity between the double panels (Kaiser, 2001), the incident and radiating panels are of different thickness (e.g. 1 mm and 2 mm steel plates, respectively, as in (Wrona and Pawelczyk, 2016a)). Panels of any material can be attached—aluminium, steel, wood, etc (Wrona and Pawelczyk, 2014a).



(a) A view of the enclosure interior with a loudspeaker. The cross-section of profiles is also visible.

(b) A view of the whole frame.



(c) A view with a panel mounted to the frame.

(d) A view with attached clamping frame.

Figure 2.1: A schematic representation of the rigid active casing.  
All dimensions are given in [mm].



Figure 2.2: A photograph of the rigid active casing (Wrona and Pawelczyk, 2014b).

### 2.2.1 Actuators and sensors

In this stage of research, a loudspeaker placed on the casing floor is used as the primary noise source. It allows for creating an environment more suitable for the research than a real operating device, which is used in due course. For feedforward control system implementations, the reference signal is obtained by a microphone placed next to the

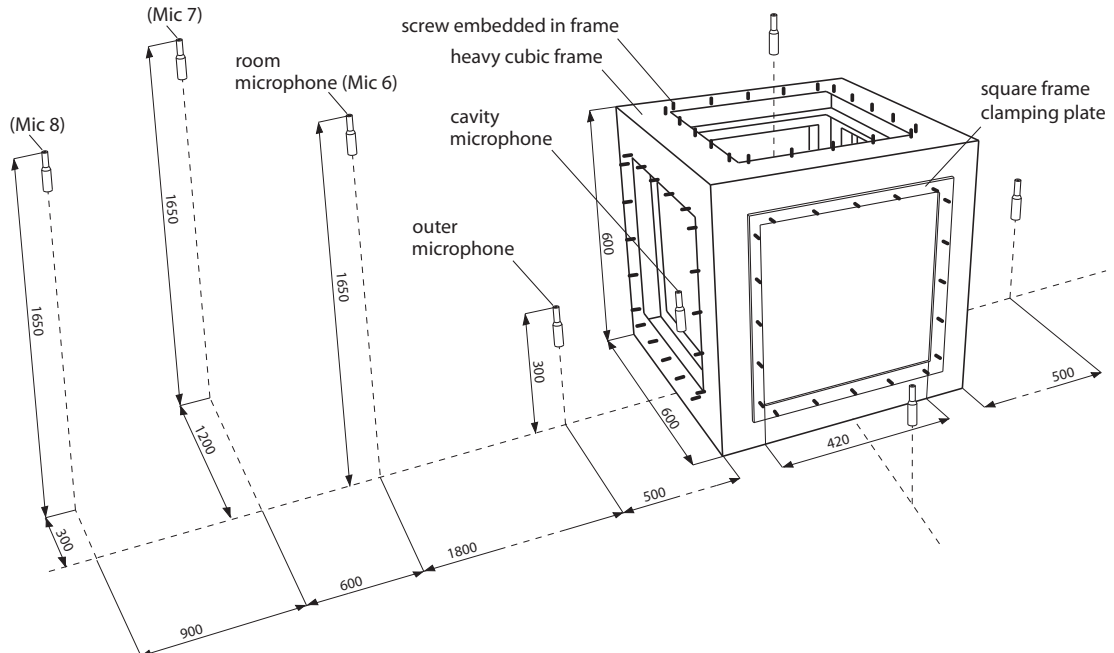


Figure 2.3: A schematic representation of the laboratory setup with the rigid active casing.  
All dimensions are given in [mm].

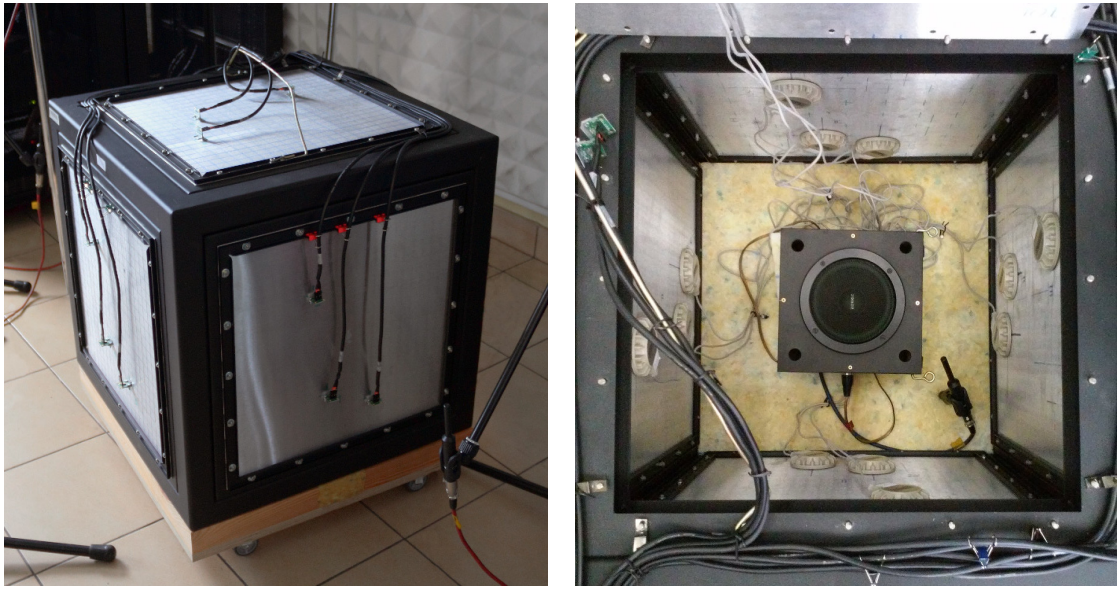


Figure 2.4: Photographs of the rigid active casing with mounted sensors and actuators (Wrona and Pawelczyk, 2015).

loudspeaker inside the casing enclosure (referred to further as the *reference microphone*). In front of each casing wall, a microphone is placed in the distance of 500 mm (referred to as the *outer microphone*). If double panels are used, a microphone is also placed in the cavity between them (referred to as the *cavity microphone*). These microphones are used mainly for control-related purposes. Additionally, to evaluate the noise reduction efficiency, three microphones are placed at several larger distances from the casing, corresponding to potential locations of the user (referred to as the *room microphones*). The laboratory setup is presented schematically in Fig. 2.3. Photographs of the rigid casing with mounted sensors and actuators are given in Fig. 2.4.

To control vibrations of the casing walls, inertial exciters NXT EX-1 are used (depicted in Fig. 2.5a). They weight 115 g and they are of small dimensions (70 mm), comparing to the size of the casing. In the performed control experiments, they are mounted on the incident plates from the inner side, three actuators per panel. Their placement has been optimized using a method that maximizes a measure of the controllability of the system. The impact of the mass of the actuators is included in the optimization procedure, as it is comparable with the mass of the casing walls and substantially affects their dynamical behaviour. The method of actuators positioning is described in details in Subsection 5.4.3 and in previous publications of the author (Wrona and Pawelczyk, 2013b; Wrona et al., 2014). The spillover effect has been also considered, e.g. in (Pawelczyk and Wrona, 2013).

As sensors for control purposes, microphones (Beyerdynamic MM-1, depicted in Fig. 2.5b) or accelerometers (Analog Devices ADXL203, presented in Fig. 2.5c) are used,



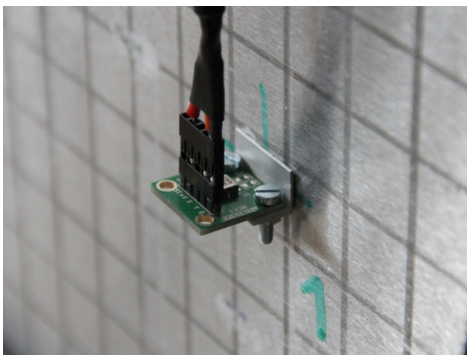
(a) The inertial exciter NXT EX-1 (Wrona and Pawelczyk, 2016b).

Properties	EX-1
Size, mm	$\varnothing 70$
Thickness, mm	19
Mass, g	115
Power handling, W	5



(b) The microphone Beyerdynamic MM-1.

Properties	MM-1
Size, mm	$\varnothing 19/9$
Height, mm	133
Mass, g	88
Polar pattern	Omnidirectional
Frequency range, Hz	20 to 20,000
Max. SPL, dB	128



(c) The accelerometer Analog Devices ADXL203.

Properties	ADXL203
Size, mm	$20 \times 20 \times 4$
Mass, g	5
Measurement range, g	$\pm 1.7$
Frequency range, Hz	0.5 to 2,500



(d) The laser vibrometer Polytec PDV-100.

Properties	PDV-100
Size, mm	$300 \times 63 \times 129$
Mass, g	2600
Frequency range, Hz	0.5 to 22,000
Velocity resolution, $\mu\text{m}/\text{s}$	< 0.02
Working distance, m	0.1 to 30

Figure 2.5: Photographs of an actuator and sensors, along with their relevant parameters.

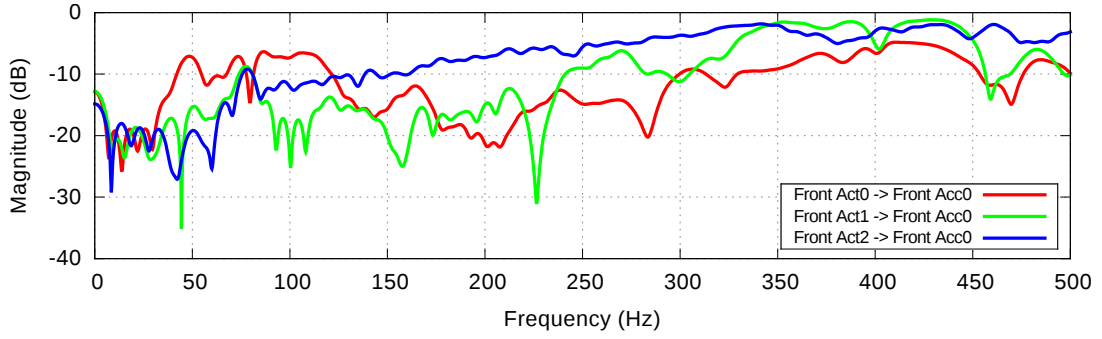
depending on the chosen control configuration. In case of single panels, the accelerometers are collocated with the actuators. For double panels, they are mounted on the radiating plate at locations calculated according to the method that maximizes a measure of the observability of the system (Wrona and Pawelczyk, 2013a). The placement of actuators and sensors is identical for each wall. In contrast to the inertial excitors, the employed accelerometers are light-weight (5 g) comparing to the mass of the casing walls, and therefore they have a marginal loading effect and their mass can be safely neglected in the mathematical modelling. However, if heavier sensors were used or an application would require a highest modelling accuracy, their mass could be modelled analogously as in the case of inertial excitors.

An additional type of the sensors used, is a laser vibrometer Polytec PDV-100, depicted in Fig. 2.5d. As a specialized laboratory equipment, it is not used for active control experiments as a signal source (it would be infeasible in commercial applications). But it is used for highly precise non-contact measurement of vibrations in laboratory environment, strictly for the research purposes (the obtained data have been used mainly to validate the mathematical modelling accuracy). Utilizing that the measurement does not affect anyhow the dynamical behaviour of the vibrating panel, all of experimentally measured modeshapes of casing walls presented in this dissertation, are obtained with the laser vibrometer.

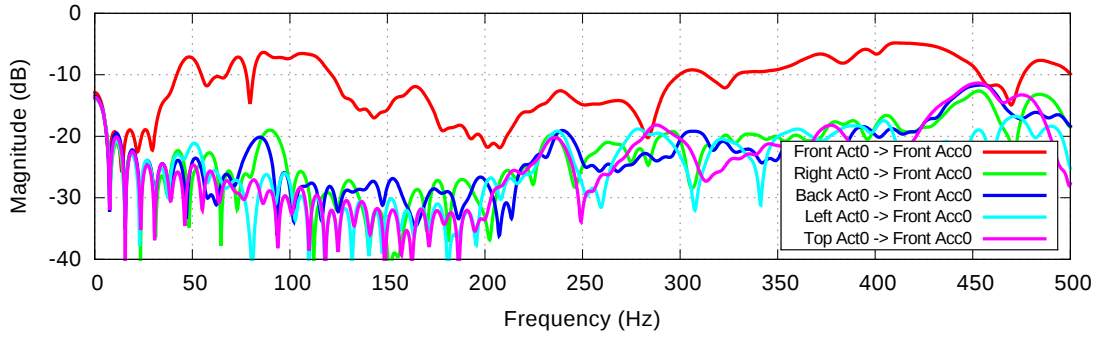
### 2.2.2 Secondary paths analysis

To present the vibroacoustical properties of the structure, a set of exemplary amplitude responses of secondary paths obtained for the rigid casing with single panels is shown in Figs. 2.6a-2.6d. It follows from the analysis that the direct paths between actuators and accelerometers mounted on the same wall are of similar magnitude in whole frequency range considered (see Fig. 2.6a). In turn, the magnitudes of cross paths between actuators mounted on one wall and accelerometers mounted on the other wall are many times weaker, comparing to magnitudes of direct paths within the same wall (see Fig. 2.6b). This is due to the heavy and rigid frame of the casing, isolating vibrationally individual walls. Hence, the interference with each other is mainly through the acoustic field. Therefore, since such separation has been noticed, for the mathematical modelling and control purposes, it is justified to consider each of the walls separately.

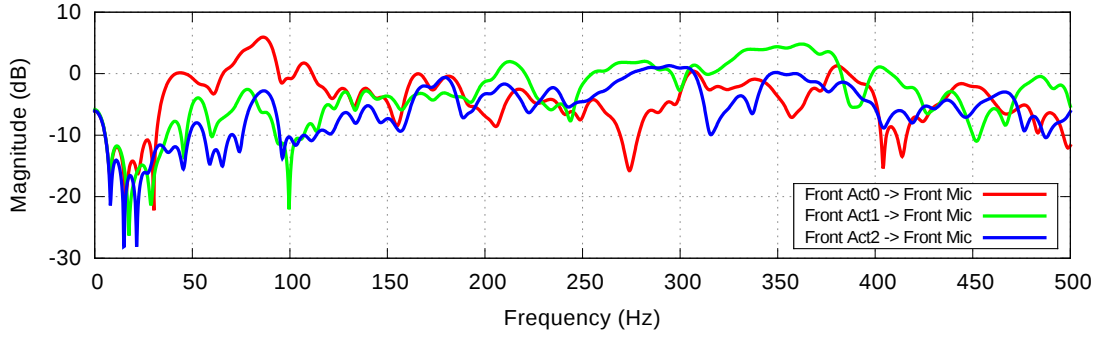
Analogous behaviour can be observed for the paths between actuators and outer microphones, but only for low frequencies up to approximately 250 Hz. Above this frequency, the cross paths between actuators mounted to one wall and an outer microphone placed in front of another wall become of similar magnitude, as the direct paths between actuators and an outer microphone assigned for the same wall (see Figs. 2.6c-2.6d). Such couplings affect the performance of active noise control systems and it is referred to in Section 6.3, where active control experiments for rigid casing are presented and discussed.



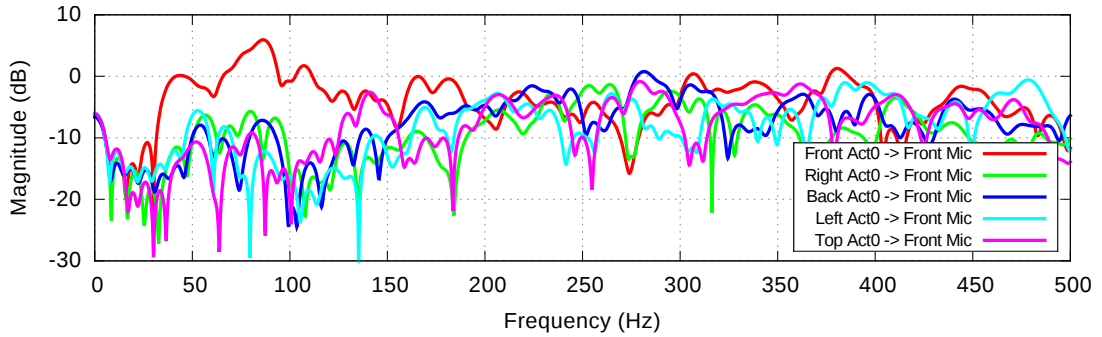
(a) Direct paths between actuators no. 0-2 and the accelerometer no. 0 mounted on the front wall.



(b) Cross paths between actuators no. 0 mounted on different walls and the accelerometer no. 0 mounted on the front wall.



(c) Direct paths between actuators no. 0-2 and the outer microphone assigned to the front wall.



(d) Cross paths between actuators no. 0 mounted on different walls and the outer microphone assigned to the front wall.

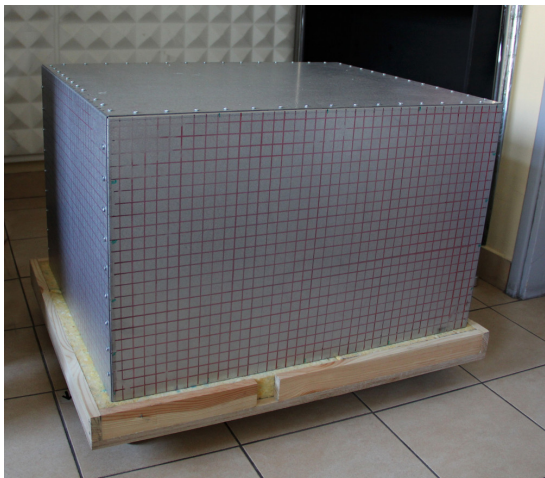
Figure 2.6: Exemplary amplitude responses of secondary paths for the rigid casing.

## 2.3 Light-weight casing

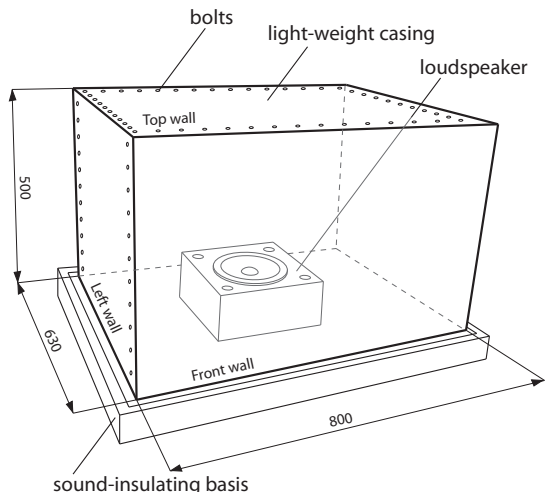
The light-weight device casing used in this stage of research is presented in Fig. 2.7. In contrast to the rigid casing used in the previous stage, the light-weight casing is made without an explicit frame. It is made of steel plates (of 1.0 mm or 1.5 mm thick, depending on version) bolted together, forming a closed cuboid of dimensions 500 mm × 630 mm × 800 mm or a cube of dimensions 500 mm × 500 mm × 500 mm, depending on version. Such structure results in greater vibrational couplings between individual walls, in addition to couplings through the acoustic field inside and, to a lesser extends, outside the casing. Moreover, due to the absence of the rigid frame, the walls are connected directly to each other, what results in boundary conditions which no longer behave as fully clamped—boundary conditions elastically restrained against both rotation and translation are more appropriate. Identification of spring constants representing elastic boundary conditions of light-weight device casing walls are performed using experimental data and a memetic algorithm. The procedure is described in details in Section 5.3 and in (Wrona and Pawelczyk, 2016c).

### 2.3.1 Actuators and sensors

Similarly as in the previous stage, a loudspeaker placed on the sound-insulating basis is used as the primary noise source. A reference microphone placed next to the loudspeaker is used to obtain the reference signal. In front of each casing wall, a microphone is placed in the distance of 500 mm (also referred to as the outer microphone). The room microphones are placed in similar configuration as in case of the rigid casing.



(a) A photograph of the light-weight casing.



(b) A schematic representation of the light-weight casing.

Figure 2.7: The light-weight active casing—a photograph and a schematic representation (Wrona and Pawelczyk, 2016d). All dimensions are given in [mm].

Photographs of the light-weight active casing with mounted sensors and actuators are given in Fig. 2.8. The laboratory setup is presented schematically in Fig. 2.9.

Inertial exciters NXT EX-1 are used to control vibrations of the casing walls. They are mounted on the walls from the inner side. The number of actuators depends on the particular wall—four actuators are mounted to front, right, back and left wall, and five actuators to the top wall. Their placement has been optimized using a method that maximizes a measure of the controllability of the system. The optimization process is

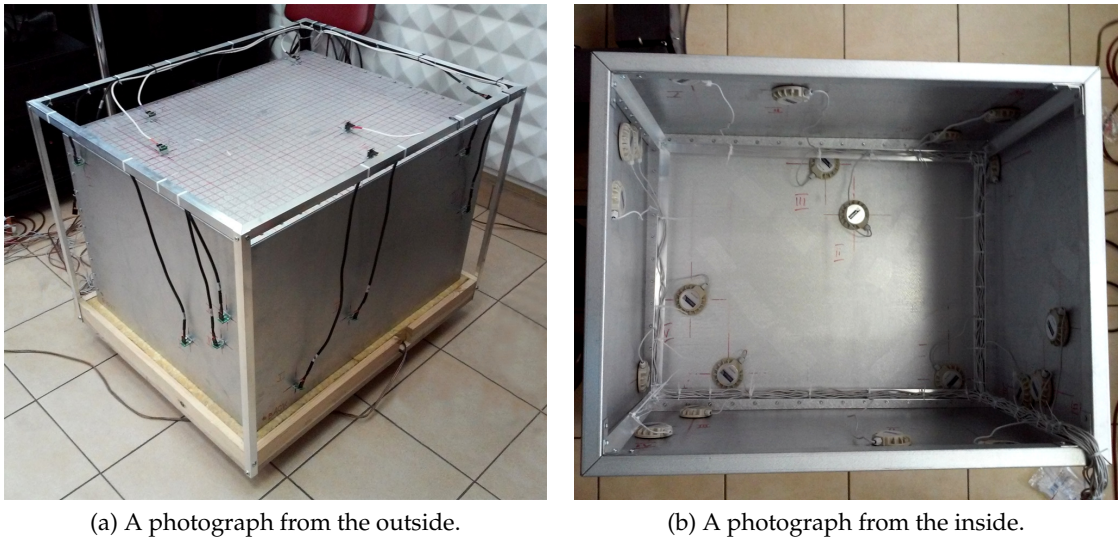


Figure 2.8: Photographs of the light-weight active casing with mounted sensors and actuators (Wrona and Pawelczyk, 2016b).

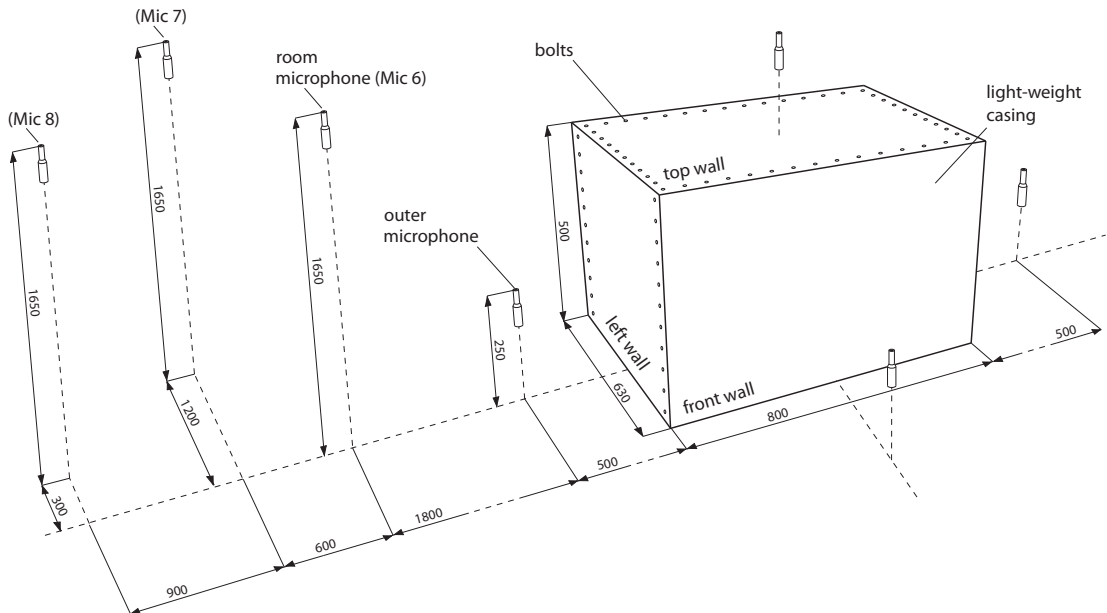


Figure 2.9: A schematic representation of the laboratory setup with the light-weight active casing. All dimensions are given in [mm].

described in Subsection 5.4.4 and in (Wrona and Pawelczyk, 2016d). Boundary conditions elastically restrained against both rotation and translation are used in the mathematical modelling (Wrona and Pawelczyk, 2016c). As shown in Fig. 2.8, light-weight frames are added to the laboratory stand to support the actuators cables (inside the casing) and sensors cables (outside the casing). These frames are made in such a manner that they do not affect the vibrational or acoustical behaviour of the casing. The accelerometers used for control purposes (Analog Devices ADXL203) are collocated with the actuators.

### 2.3.2 Frequency response functions

The described light-weight casing is a three-dimensional structure. The couplings between individual walls, of both vibrational and acoustical nature, are significant. However, noteworthy is an analysis of spatially averaged (over the area of each wall) frequency responses of three walls of the casing, presented in Fig. 2.10 (left, front and top

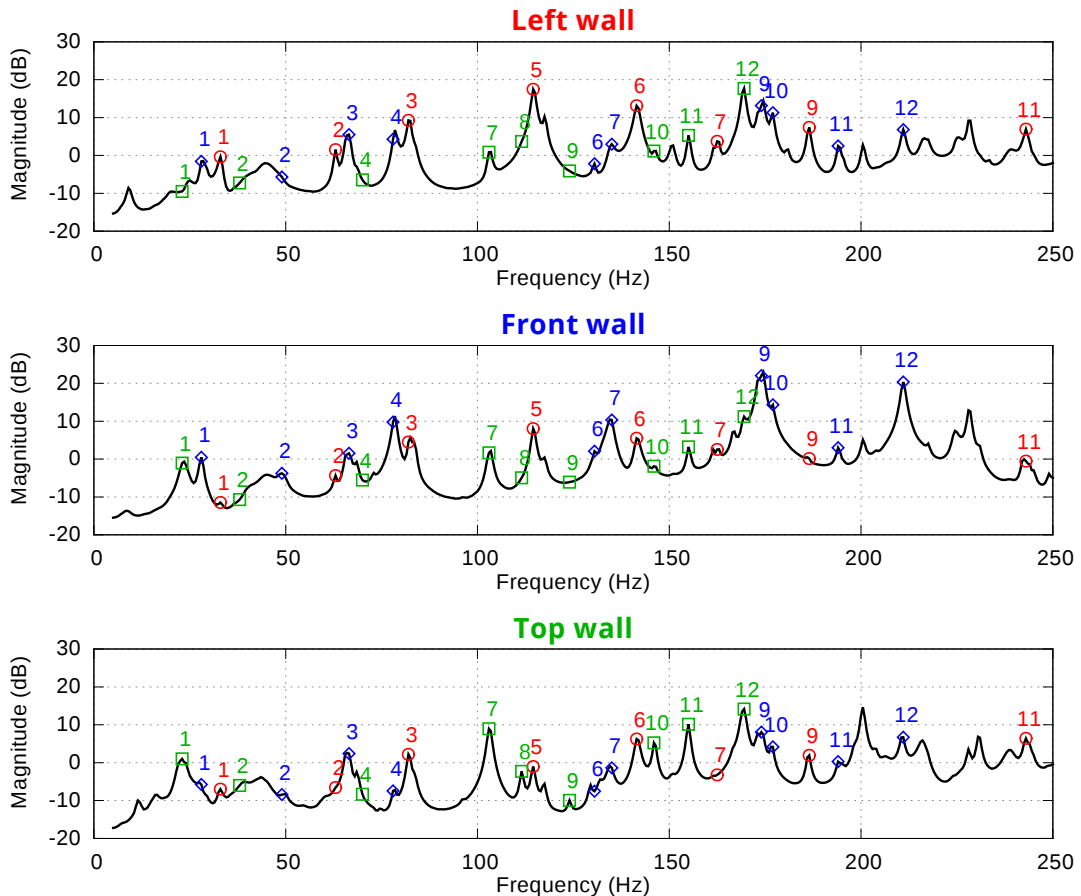


Figure 2.10: Spatially averaged frequency responses of casing walls. Two pairs of walls are symmetrical (left and right, front and back), hence only one of each pair is presented in the Figure. Initial 12 eigenmodes originating at each wall are marked: eigenmodes originating at left wall are marked with red circle, at front wall with blue diamond, at top wall with green square.

walls; right and back walls are omitted as they are symmetrical to the left and front walls, respectively). Resonances that originate on one wall, are clearly visible on the others. However, all of resonances visible as peaks in the given frequency range can be assigned to one of the walls where they originate. Such assignment of the eigenmodes is consistent with the mathematical model developed in Chapter 3 and validated for the light-weight casing in Subsection 4.3.2.

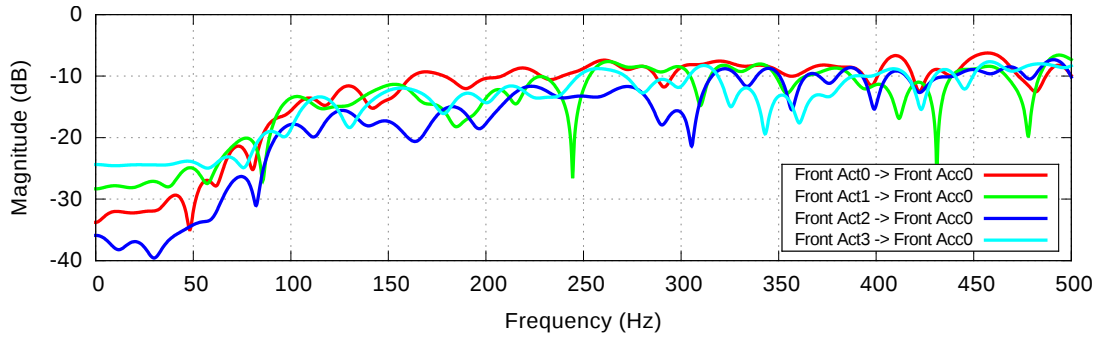
It leads to a conclusion that observed natural frequencies and modeshapes of the whole structure are a consequence of superposition of resonances of each wall excited individually (but as a part of the structure). Therefore, it is justified to analyse the walls separately for the purpose of optimization of actuators locations, considering only eigenmodes due to the given wall—if the resonance is appropriately modelled at the wall where it originates, it will be accordingly included in the process of sensors and actuators arrangement optimization for the whole casing. It means also that if the given mode is controlled with actuators at the wall where it originates, it will be reduced for the whole casing.

But it is also worth noting at this point that for the control purposes (see Section 6.4), separate control of each wall has more strict limitations, than in case of the rigid casing—a multichannel control system for the whole casing is more appropriate.

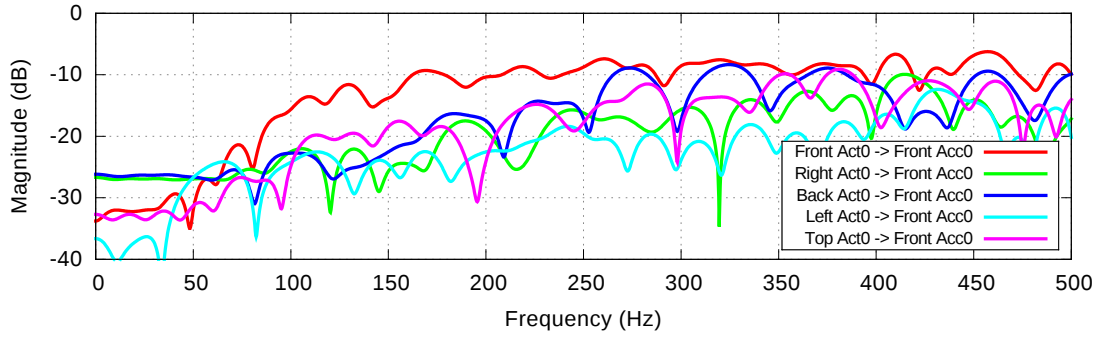
### 2.3.3 Secondary paths analysis

It follows from the analysis of secondary paths given in Fig. 2.11 that magnitudes of cross paths between actuators mounted on one wall and accelerometers mounted on the other wall are weaker than magnitudes of direct paths within the same wall only up to frequency of approximately 250 Hz (see Figs. 2.11a-2.11b). Above this frequency, magnitudes of cross paths and direct paths are similar. It confirms, as expected, higher vibrational couplings between individual walls than in case of the rigid casing (where cross paths are many times weaker than direct paths in whole frequency range considered).

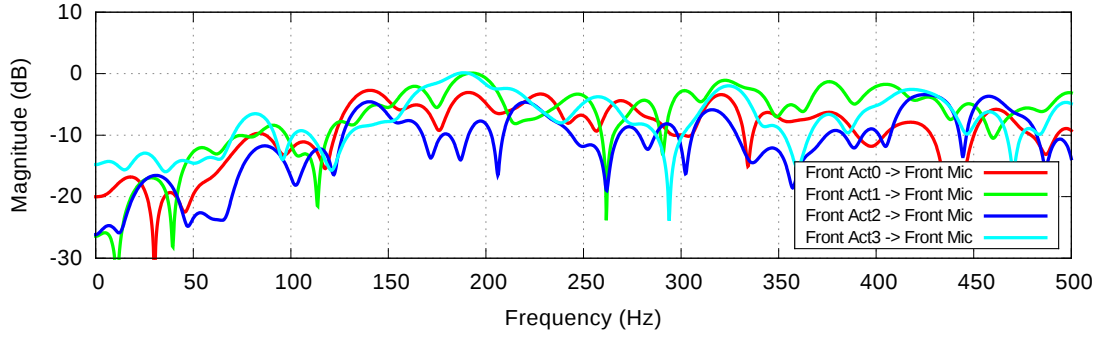
On the other hand, for the paths between actuators and outer microphones, cross paths and direct paths represent a similar magnitude in the whole frequency range (in contrast to the case of the rigid casing, where for low frequencies direct paths dominated over cross paths). Direct paths between actuators no. 0-3 and the outer microphone assigned to the front wall are shown in Fig. 2.11c. Cross paths between actuators no. 0 mounted on different walls and the outer microphone assigned to the front wall are presented in Fig. 2.11d. Such strong couplings generally make the synthesis of active noise control systems more difficult and it will be discussed to in Section 6.4.



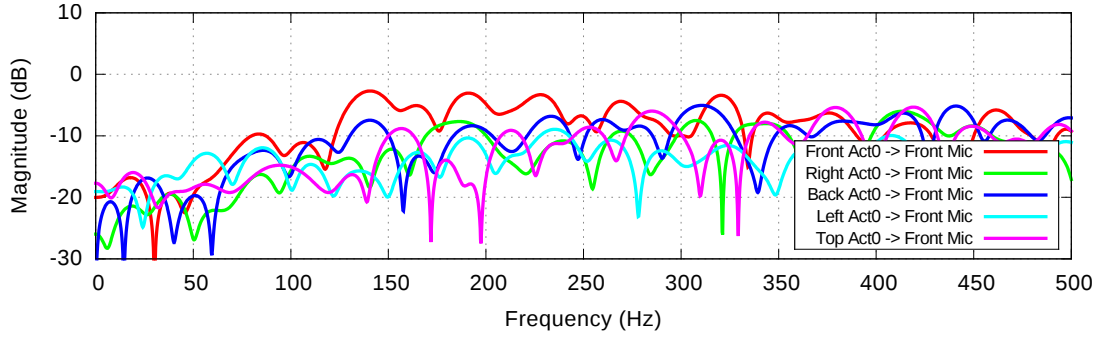
(a) Direct paths between actuators no. 0-3 and the accelerometer no. 0 mounted on the front wall.



(b) Cross paths between actuators no. 0 mounted on different walls and the accelerometer no. 0 mounted on the front wall.



(c) Direct paths between actuators no. 0-3 and the outer microphone assigned to the front wall.



(d) Cross paths between actuators no. 0 mounted on different walls and the outer microphone assigned to the front wall.

Figure 2.11: Exemplary amplitude responses of secondary paths for the light-weight casing.

## 2.4 Summary

The laboratory setup for active control experiments consisting of several different device casings has been discussed in this Chapter. The discussion have included practical application-related aspects of the laboratory stand assembly, vibroacoustic analysis of the introduced structures and selection of sensors and actuators for the active control systems.

Initially the rigid casing has been examined. Following conclusions are formulated basing on the analysis of secondary paths:

- the direct paths between actuators and accelerometers mounted on the same wall significantly dominate the cross paths between actuators mounted on one wall and accelerometers mounted on the other wall, what confirms high vibrational isolation between walls;
- for the paths between actuators and outer microphones, direct paths dominate the cross paths only for low frequencies up to approximately 250 Hz (above this frequency, they become of similar magnitude).

Afterwards, the light-weight casing has been considered. Studying its secondary paths and frequency response functions, following conclusions are formulated:

- direct vibrational paths dominate the cross paths only up to approximately 250 Hz. (above this frequency, magnitudes of cross paths and direct paths are similar, what confirms higher vibrational couplings);
- for the paths between actuators and outer microphones, cross paths and direct paths represent a similar magnitude in the whole frequency range considered;
- observed natural frequencies and modeshapes of the whole structure are a consequence of superposition of resonances of each wall excited individually (but as a part of the structure)—therefore, it is justified to analyse the walls separately for the purpose of optimization of actuators locations, considering only eigenmodes due to the given wall.



# Chapter 3

## Modelling of the device casings

### 3.1 Background

Formulation of a mathematical model of the considered device casings brings a set of benefits. Firstly, if the model is properly validated, it can be used for simulation and analysis of the vibrating casing dynamical behaviour what facilitates a better understanding of the structure. It can be also used for preliminary evaluations of active control strategies. Moreover, what is of particular interest in this dissertation, the model can be used for optimization of the structure—to shape its frequency response to improve its passive properties or to maximize the susceptibility of the plant to the active control. Also, it can be used to efficiently apply actuators and sensors, so the maximum advantage could be taken of them. All of the aforementioned benefits constitutes a significant value, what justify the undertaken effort to formulate the appropriate model.

The successful application of the mathematical model depends on its accuracy, as it should appropriately reflect real behaviour of the plant. On the other hand, to facilitate practical applicability, the model should not be complicated more than it is necessary. Therefore, usually the model constitutes a trade-off between accuracy and complexity. In the presented modelling of the device casing, there are several simplifying assumptions adopted to obtain such balance.

Most importantly, basing on the vibroacoustical analysis given in the previous Chapter, each wall of the casing is considered separately. It is an intuitive approach for the rigid casing where the separation of the walls is clearly visible. However, same approach is adopted in case of the light-weight casing, as its frequency response can be decomposed into responses of individual walls (see Subsection 2.3.2). Therefore, when modelling each of the walls separately, the overall behaviour of the casing is also sufficiently reflected. Other assumptions are related to the employed theories of individual vibrating panels—the assumption of small deflections of the panels, homogeneity of the panel material, etc. They are described in more details in the following sections.

This Chapter is organized as follows. In Section 3.2 fundamental issues of the thin and thick plate theories are recalled to set a reference for further reading. Section 3.3 defines the elastically restrained boundary conditions of the casing walls. Section 3.4 describes an impact of additional elements bonded to the wall surface—masses, ribs, actuators and sensors. In Section 3.5 the total energy functional is formulated. It is

used in Section 3.6, where the Rayleigh-Ritz method is used to find an approximate solution of the developed model. Then, in Section 3.7 the model is presented in state space, what facilitates further application and analysis. Finally, taking advantage of such representation, in Section 3.8 measures of controllability and observability of the system are defined.

## 3.2 Vibration of individual plates

A plate is a structural element with a small thickness compared to the planar dimensions. In most cases, the thickness is no greater than one-tenth of the smaller in-plane dimension (Reddy, 2006). The theory of plates is an approximation of the three-dimensional elasticity theory to two dimensions, which assumes that a mid-surface plane can be used to represent deformation of every point of the plate. The aim of the plate theory is to study the deformation and stresses in plate structures subjected to loads.

In this Section, fundamental issues of two-dimensional mathematical models of plates are recalled to set a reference for further reading, where the final form of a model used for analysis of the casing walls is presented. Detailed derivations of presented models can be found, e.g. in (Timoshenko and Woinowsky-Krieger, 1959; Reddy, 2006; Rao, 2007).

### 3.2.1 Kirchhoff–Love plate theory

The Kirchhoff–Love theory is a most elementary mathematical model of plates considered in this dissertation. This theory is an extension of Euler–Bernoulli beam theory and was developed in 1888 by Love using the Kirchhoff hypothesis (Love, 1888), which consists of the following assumptions:

- straight lines perpendicular to the mid-surface (i.e. transverse normals) before deformation remain straight after deformation;
- the transverse normals rotate such that they remain perpendicular to the mid-surface after deformation;
- the transverse normals do not experience elongation (i.e. the thickness of the plate does not change during a deformation).

Such assumptions are eligible for thin plates with small deflections, where shear energy is negligible.

Due to the application of plate models for modelling of casing walls, hereinafter the plate theories are considered and presented for rectangular plates (as a most common shape of device casing walls). Hence, all following mathematical models are given in Cartesian coordinates system. However, presented theories are valid for plates of any

shape and they can be easily expressed in different form, more suitable for other plate shapes.

### Isotropic Kirchhoff plate

For an isotropic and homogeneous plate, which occupies the  $X - Y$  plane in the reference stress-free state, free vibrations are governed by a differential system:

$$D \left( \frac{\partial^4 w}{\partial x^4} + 2 \frac{\partial^4 w}{\partial x^2 \partial y^2} + \frac{\partial^4 w}{\partial y^4} \right) + \rho_p h \frac{\partial^2 w}{\partial t^2} = 0, \quad (3.1)$$

for

$$x \in (0, a), \quad y \in (0, b), \quad t > t_0 > 0, \quad (3.2)$$

where

$$D = \frac{Eh^3}{12(1 - \nu^2)}. \quad (3.3)$$

Initial conditions are defined by:

$$w(x, y, t_0) = 0, \quad \left. \frac{\partial w(x, y, t)}{\partial t} \right|_{t=t_0} = 0. \quad (3.4)$$

In Eq. (3.1)-(3.4) the function  $w(x, y, t)$  denotes the displacement of the plate from the reference state to the  $z$ -direction at time  $t > 0$  and position  $(x, y)$ ; the lengths of rectangular plate sides are assumed to be equal to  $a$  and  $b$ , respectively;  $D$  is the flexural rigidity;  $E$  is the Young's modulus;  $\nu$  is the Poisson's ratio;  $\rho_p$  is the mass density of the plate material; and  $h$  is the plate thickness.

The definitions of domains of spatial variables and time given in Eq. (3.2), for the sake of brevity, are not repeated in following considerations in this Section. However, they are the same for all presented plate models.

Considering only the transverse motion and neglecting the effect of rotary inertia, the kinetic and strain energies of the plate,  $T_p$  and  $U_p$ , can be written as:

$$T_p = \frac{\rho_p h}{2} \iint_S \left( \frac{\partial w}{\partial t} \right)^2 dx dy, \quad (3.5a)$$

$$U_p = \frac{D}{2} \iint_S \left\{ \left( \frac{\partial^2 w}{\partial x^2} \right)^2 + \left( \frac{\partial^2 w}{\partial y^2} \right)^2 + 2\nu \frac{\partial^2 w}{\partial x^2} \frac{\partial^2 w}{\partial y^2} + 2(1 - \nu) \left( \frac{\partial^2 w}{\partial x \partial y} \right)^2 \right\} dx dy, \quad (3.5b)$$

where  $S$  is the surface of the plate. The definition of the kinetic and strain energies of the plate is particularly important in this dissertation, as the Rayleigh-Ritz method (see Section 3.6) is used to find an approximate solution of the differential system (the method is based on the definition of an energy functional).

### Orthotropic Kirchhoff plate

Equation (3.1) can be extended to a case of orthotropic plates, which have material properties that differ along two orthogonal axes (in contrast to isotropic materials that have the same properties in every direction). It is an important subset of anisotropic plates. An example is a sheet metal formed by squeezing thick sections of metal between heavy rollers. Its properties differ between the direction it was rolled in and each of the two transverse directions. Sheet metal is commonly used for device casings, which are of particular interest in this dissertation.

Assuming that the orthotropic plate material have axes of symmetry along  $x$  and  $y$  directions, free vibrations of such plate are governed by the equation:

$$D_x \frac{\partial^4 w}{\partial x^4} + 2(D_x \nu_y + 2D_{xy}) \frac{\partial^4 w}{\partial x^2 \partial y^2} + D_y \frac{\partial^4 w}{\partial y^4} + \rho_p h \frac{\partial^2 w}{\partial t^2} = 0, \quad (3.6)$$

where

$$D_x = \frac{E_x h^3}{12(1 - \nu_x \nu_y)}, \quad D_y = \frac{E_y h^3}{12(1 - \nu_x \nu_y)}, \quad D_{xy} = \frac{G h^3}{12}. \quad (3.7)$$

In (3.6)-(3.7)  $D_x$ ,  $D_y$ , and  $D_{xy}$  are orthotropic rigidities of the plate;  $E_x$  and  $E_y$  are the Young moduli along the  $x$  and  $y$  directions, respectively;  $G$  is the shear modulus;  $\nu_x$  and  $\nu_y$  are the Poisson's ratios corresponding to  $x$  and  $y$  direction, respectively. Four elastic constants  $E_x$ ,  $E_y$ ,  $G$ ,  $\nu_x$  are independent (while the isotropic plate model needs only two elastic constants to be defined). The coefficient  $\nu_y$  can be determined according to the following relation:

$$\frac{\nu_x}{E_x} = \frac{\nu_y}{E_y}. \quad (3.8)$$

It can be easily shown that if  $E_x = E_y$  and  $\nu_x = \nu_y$ , then Eq. (3.6) simplifies to (3.1). It is also helpful to express the shear modulus  $G$  in terms of Young modulus  $E$  and Poisson's ratio  $\nu$  as:

$$G = \frac{E}{2(1 + \nu)}. \quad (3.9)$$

The kinetic energy of the orthotropic plate can be calculated according to Eq. (3.5a), as in case of an isotropic plate. However, the strain energy is expressed as:

$$U_p = \frac{1}{2} \iint_S \left\{ D_x \left( \frac{\partial^2 w}{\partial x^2} \right)^2 + D_y \left( \frac{\partial^2 w}{\partial y^2} \right)^2 + 2D_x \nu_y \frac{\partial^2 w}{\partial x^2} \frac{\partial^2 w}{\partial y^2} + 4D_{xy} \left( \frac{\partial^2 w}{\partial x \partial y} \right)^2 \right\} dx dy. \quad (3.10)$$

#### 3.2.2 Mindlin–Reissner plate theory

The Mindlin–Reissner theory is an extension of Kirchhoff–Love theory that takes into account rotary inertia and shear deformations of a plate (Mindlin, 1951). It is obtained by relaxing the Kirchhoff's normality restriction and allowing for arbitrary but constant

rotation of transverse normals after deformation (it is an analogy of extension of Euler–Bernoulli beam theory to Timoshenko beam theory). The Mindlin–Reissner theory is especially suitable for thick plates (i.e. with side to thickness ratios of the order of 20 or less), since Kirchhoff–Love theory tends to underpredict deflections and overpredict natural frequencies of such plates.

### Isotropic Mindlin plate

Assuming that the functions  $\Theta_x(x, y, t)$  and  $\Theta_y(x, y, t)$  denote the rotations of a transverse normal at position  $(x, y)$  in the  $x$  and  $y$  directions, respectively, free vibrations the isotropic Mindlin plate are governed by the equations:

$$\frac{\rho_p h^3}{12} \frac{\partial^2 \Theta_x}{\partial t^2} - \frac{D}{2} \left[ (1-\nu) \left( \frac{\partial^2 \Theta_x}{\partial x^2} + \frac{\partial^2 \Theta_x}{\partial y^2} \right) + (1+\nu) \left( \frac{\partial^2 \Theta_x}{\partial x^2} + \frac{\partial^2 \Theta_y}{\partial x \partial y} \right) \right] + \kappa h G \left( \frac{\partial w}{\partial x} + \Theta_x \right) = 0, \quad (3.11a)$$

$$\frac{\rho_p h^3}{12} \frac{\partial^2 \Theta_y}{\partial t^2} - \frac{D}{2} \left[ (1-\nu) \left( \frac{\partial^2 \Theta_y}{\partial x^2} + \frac{\partial^2 \Theta_y}{\partial y^2} \right) + (1+\nu) \left( \frac{\partial^2 \Theta_y}{\partial y^2} + \frac{\partial^2 \Theta_x}{\partial x \partial y} \right) \right] + \kappa h G \left( \frac{\partial w}{\partial y} + \Theta_y \right) = 0, \quad (3.11b)$$

$$\rho_p h \frac{\partial^2 w}{\partial t^2} - \kappa h G \left( \frac{\partial^2 w}{\partial x^2} + \frac{\partial^2 w}{\partial y^2} + \frac{\partial \Theta_x}{\partial x} + \frac{\partial \Theta_y}{\partial y} \right) = 0, \quad (3.11c)$$

where  $\kappa$  is the shear coefficient. Initial conditions are defined by:

$$w(x, y, t_0) = 0, \quad \left. \frac{\partial w(x, y, t)}{\partial t} \right|_{t=t_0} = 0, \quad (3.12a)$$

$$\Theta_x(x, y, t_0) = 0, \quad \left. \frac{\partial \Theta_x(x, y, t)}{\partial t} \right|_{t=t_0} = 0, \quad (3.12b)$$

$$\Theta_y(x, y, t_0) = 0, \quad \left. \frac{\partial \Theta_y(x, y, t)}{\partial t} \right|_{t=t_0} = 0. \quad (3.12c)$$

Kinetic and strain energies of the plate,  $T_p$  and  $U_p$ , can be calculated as:

$$T_p = \frac{\rho_p h}{2} \iint_S \left\{ \frac{h^2}{12} \left[ \left( \frac{\partial \Theta_x}{\partial t} \right)^2 + \left( \frac{\partial \Theta_y}{\partial t} \right)^2 \right] + \left( \frac{\partial w}{\partial t} \right)^2 \right\} dx dy, \quad (3.13a)$$

$$U_p = \frac{1}{2} \iint_S \left\{ D \left[ \left( \frac{\partial \Theta_x}{\partial x} \right)^2 + \left( \frac{\partial \Theta_y}{\partial y} \right)^2 + 2\nu \frac{\partial \Theta_x}{\partial x} \frac{\partial \Theta_y}{\partial y} + \frac{1}{2} (1-\nu) \left( \frac{\partial \Theta_x}{\partial y} + \frac{\partial \Theta_y}{\partial x} \right)^2 \right] + \kappa h G \left[ \left( \frac{\partial w}{\partial x} + \Theta_x \right)^2 + \left( \frac{\partial w}{\partial y} + \Theta_y \right)^2 \right] \right\} dx dy. \quad (3.13b)$$

It is noteworthy that by setting  $\Theta_x = -\frac{\partial w}{\partial x}$ ,  $\Theta_y = -\frac{\partial w}{\partial y}$ , and neglecting the effect of rotary inertia in (3.13a) and (3.13b), the energy definitions (3.5a) and (3.5b) for Kirchhoff plate can be obtained.

### Orthotropic Mindlin plate

Assuming that the orthotropic Mindlin plate material have axes of symmetry along  $x$  and  $y$  directions (analogously like in case of an orthotropic Kirchhoff plate), free vibrations of such plate are governed by the equations:

$$\frac{\rho_p h^3}{12} \frac{\partial^2 \Theta_x}{\partial t^2} - D_x \left( \frac{\partial^2 \Theta_x}{\partial x^2} + \nu_y \frac{\partial^2 \Theta_y}{\partial x \partial y} \right) - D_{xy} \left( \frac{\partial^2 \Theta_x}{\partial y^2} + \frac{\partial^2 \Theta_y}{\partial x \partial y} \right) + \kappa_x h G_{xz} \left( \frac{\partial w}{\partial x} + \Theta_x \right) = 0, \quad (3.14a)$$

$$\frac{\rho_p h^3}{12} \frac{\partial^2 \Theta_y}{\partial t^2} - D_y \left( \frac{\partial^2 \Theta_y}{\partial y^2} + \nu_x \frac{\partial^2 \Theta_x}{\partial x \partial y} \right) - D_{xy} \left( \frac{\partial^2 \Theta_y}{\partial x^2} + \frac{\partial^2 \Theta_x}{\partial x \partial y} \right) + \kappa_y h G_{yz} \left( \frac{\partial w}{\partial y} + \Theta_y \right) = 0, \quad (3.14b)$$

$$\rho_p h \frac{\partial^2 w}{\partial t^2} - \kappa_x h G_{xz} \left( \frac{\partial^2 w}{\partial x^2} + \frac{\partial \Theta_x}{\partial x} \right) - \kappa_y h G_{yz} \left( \frac{\partial^2 w}{\partial y^2} + \frac{\partial \Theta_y}{\partial y} \right) = 0, \quad (3.14c)$$

where

$$D_x = \frac{E_x h^3}{12(1 - \nu_x \nu_y)}, \quad D_y = \frac{E_y h^3}{12(1 - \nu_x \nu_y)}, \quad D_{xy} = \frac{G_{xy} h^3}{12}. \quad (3.15)$$

In Eqs. (3.14a) - (3.15),  $G_{xy}$ ,  $G_{xz}$  and  $G_{yz}$  are the shear moduli in  $X-Y$ ,  $X-Z$  and  $Y-Z$  planes, respectively;  $\kappa_x$  and  $\kappa_y$  are the shear coefficients in the  $x$  and  $y$  directions, respectively. It can be easily shown, similarly as in case of Kirchhoff plate, that if given elastic constants corresponding to different directions become equal, then Eqs. (3.14) simplifies to (3.11).

The kinetic energy is calculated in the same manner as for isotropic Mindlin plate, given in Eq. (3.13a). However, the strain energy  $U_p$  is expressed by:

$$U_p = \frac{1}{2} \iint_S \left\{ D_x \left( \frac{\partial \Theta_x}{\partial x} \right)^2 + D_y \left( \frac{\partial \Theta_y}{\partial y} \right)^2 + (\nu_y D_x + \nu_x D_y) \frac{\partial \Theta_x}{\partial x} \frac{\partial \Theta_y}{\partial y} + D_{xy} \left( \frac{\partial \Theta_x}{\partial y} + \frac{\partial \Theta_y}{\partial x} \right)^2 + \kappa_x h G_{xz} \left( \frac{\partial w}{\partial x} + \Theta_x \right)^2 + \kappa_y h G_{yz} \left( \frac{\partial w}{\partial y} + \Theta_y \right)^2 \right\} dx dy. \quad (3.16)$$

As the most general of the considered models, the orthotropic Mindlin plate model is used in the following considerations and analysis. Therefore, it is helpful to express the kinetic and strain energies of the plate, given in Eqs. (3.13a) and (3.16), in non-dimensional coordinates, which facilitate the solution of the differential system (described in Section 3.6). Introducing non-dimensional coordinates  $\xi = \frac{x}{a}$ ,  $\eta = \frac{y}{b}$ , and a non-dimensional parameter  $\alpha_p = \frac{a}{b}$ , the kinetic and strain energies of the plate can be calculated as:

$$T_p = \frac{\rho_p h a b}{2} \int_0^1 \int_0^1 \left\{ \frac{h^2}{12} \left[ \left( \frac{\partial \Theta_x}{\partial t} \right)^2 + \left( \frac{\partial \Theta_y}{\partial t} \right)^2 \right] + \left( \frac{\partial w}{\partial t} \right)^2 \right\} d\xi d\eta, \quad (3.17a)$$

$$U_p = \frac{1}{2\alpha_p} \int_0^1 \int_0^1 \left\{ D_x \left( \frac{\partial \Theta_x}{\partial \xi} \right)^2 + \alpha_p^2 D_y \left( \frac{\partial \Theta_y}{\partial \eta} \right)^2 + \alpha_p (\nu_y D_x + \nu_x D_y) \frac{\partial \Theta_x}{\partial \xi} \frac{\partial \Theta_y}{\partial \eta} \right. \\ \left. + D_{xy} \left( \alpha_p \frac{\partial \Theta_x}{\partial \eta} + \frac{\partial \Theta_y}{\partial \xi} \right)^2 + \kappa_x h G_{xz} \left( \frac{\partial w}{\partial \xi} + a\Theta_x \right)^2 + \alpha_p^2 \kappa_y h G_{yz} \left( \frac{\partial w}{\partial \eta} + b\Theta_y \right)^2 \right\} d\xi d\eta. \quad (3.17b)$$

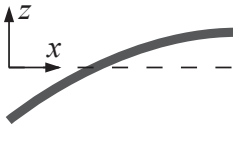
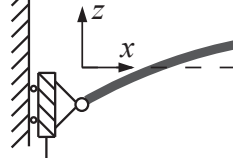
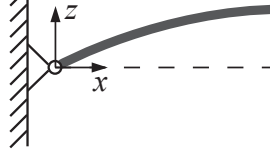
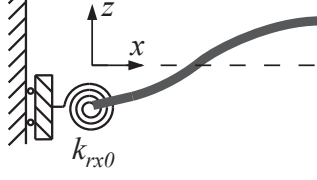
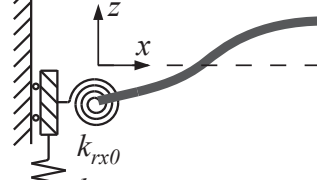
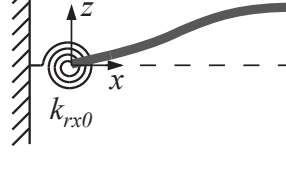
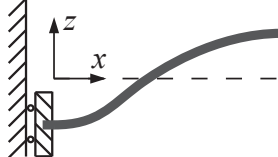
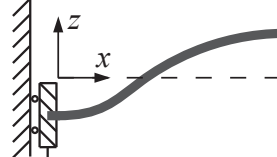
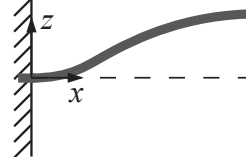
### 3.3 Boundary conditions

Type of mounting of the plate edges affects strongly its behaviour (both natural frequencies and modeshapes). Therefore, the boundary conditions should be always carefully considered and appropriately modelled. In the literature, classical boundary conditions have been thoroughly evaluated—simply-supported, fully-clamped or free edges (e.g. in (Leissa, 1969)). However, the actual boundary conditions of a real system are mostly not classical, but somewhere in between these conditions. In this dissertation, a general formulation of boundary conditions is employed—plate edges are elastically restrained against both translation and rotation. Such mounting is represented by translational and rotational springs distributed linearly along plate edges and defined by spring constants (it corresponds to a majority of practical application of plates, including casing walls). It can be easily showed that the classical boundary conditions of the plate can be obtained as limiting cases when the spring constants approach their natural limits of zero or infinity (it is schematically presented in Tab. 3.1). Detailed considerations and derivation of elastic boundary conditions can be found e.g. in (Rao, 2007).

For the sake of brevity, necessary definitions of the boundary conditions are presented strictly for the purpose of application of the Rayleigh-Ritz method. In this method, appropriate admissible functions, which satisfy the geometric boundary conditions have to be chosen. These functions, in fact, determine, which geometry of the plate is considered, and what boundary conditions are adopted (together with an appropriate energy functional). To obtain the admissible functions, in this dissertation products of characteristic orthogonal polynomials having the properties of Timoshenko beam functions are used (a rectangular plate is considered, hence there are two beams assumed, corresponding to  $x$  and  $y$  directions). Therefore, equations representing the boundary conditions are presented as for the Timoshenko beam, but in fact, an edge of the beam represent homogeneous boundary conditions of a corresponding edge of the plate.

To describe in such manner boundary conditions of four plate edges, eight spring constants needs to be defined, as shown in Fig. 3.1. Translational spring constants in the  $x$  direction at  $x = 0$  and  $x = a$ , and in the  $y$  direction at  $y = 0$  and  $y = b$  are designated as  $k_{tx0}$ ,  $k_{tx1}$ ,  $k_{ty0}$  and  $k_{ty1}$ , respectively. Rotational spring constants for plate edges given in the same manner as above, are noted as  $k_{rx0}$ ,  $k_{rx1}$ ,  $k_{ry0}$  and  $k_{ry1}$ , respectively.

Table 3.1: Summary of different boundary conditions, depending on spring constants, at the exemplary plate edge  $x = 0$ . The dashed line represents the reference state of the plate.

	$k_{tx0} = 0$	$0 < k_{tx0} < \infty$	$k_{tx0} = \infty$
$k_{rx0} = 0$	 free edge $\frac{\partial^2 \Theta_x}{\partial x^2} = 0,$ $\frac{\partial \Theta_x}{\partial x} = 0.$	 $k_{tx0}w = -D_x \frac{\partial^2 \Theta_x}{\partial x^2},$ $\frac{\partial \Theta_x}{\partial x} = 0.$	 simply-supported edge $w = 0,$ $\frac{\partial \Theta_x}{\partial x} = 0.$
$0 < k_{rx0} < \infty$	 $\frac{\partial^2 \Theta_x}{\partial x^2} = 0,$ $k_{rx0}\Theta_x = D_x \frac{\partial \Theta_x}{\partial x}.$	 $k_{tx0}w = -D_x \frac{\partial^2 \Theta_x}{\partial x^2},$ $k_{rx0}\Theta_x = D_x \frac{\partial \Theta_x}{\partial x}.$	 $w = 0,$ $k_{rx0}\Theta_x = D_x \frac{\partial \Theta_x}{\partial x}.$
$k_{rx0} = \infty$	 $\frac{\partial^2 \Theta_x}{\partial x^2} = 0,$ $\Theta_x = 0.$	 $k_{tx0}w = -D_x \frac{\partial^2 \Theta_x}{\partial x^2},$ $\Theta_x = 0.$	 fully clamped edge $w = 0,$ $\Theta_x = 0.$

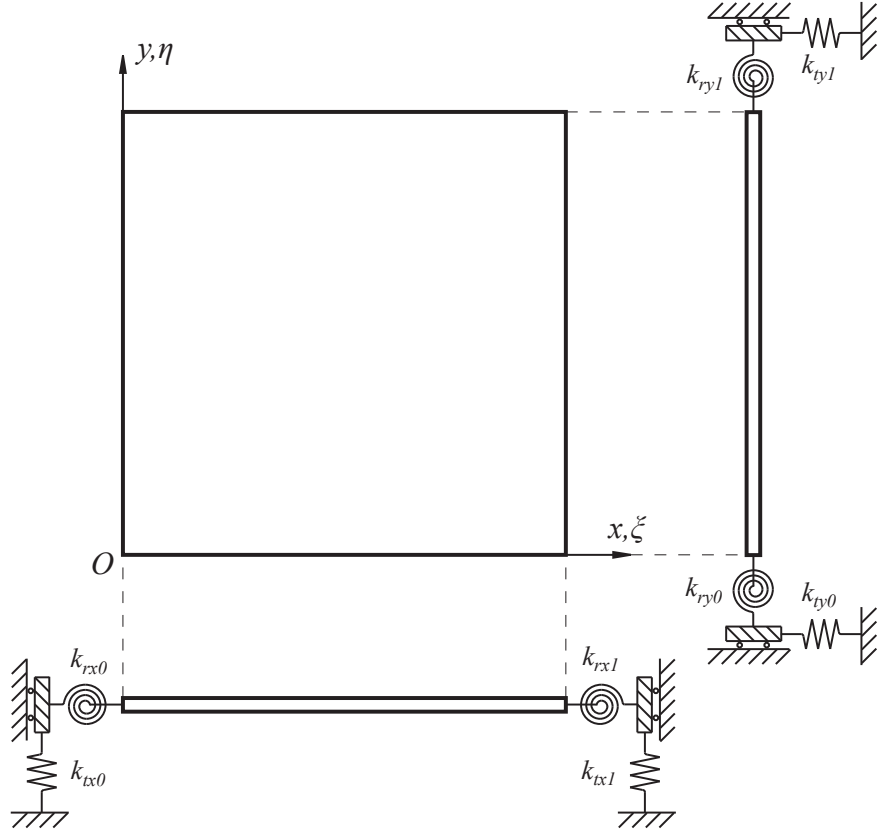


Figure 3.1: A multiview orthographic projection of the rectangular plate with boundary conditions represented as rotational and translational springs.

With such notation, the boundary conditions for elastically restrained edges are:

$$k_{tx0}w = -D_x \frac{\partial^2 \Theta_x}{\partial x^2}, \quad k_{rx0}\Theta_x = D_x \frac{\partial \Theta_x}{\partial x} \quad \text{at } x = 0, \quad (3.18a)$$

$$k_{tx1}w = D_x \frac{\partial^2 \Theta_x}{\partial x^2}, \quad k_{rx1}\Theta_x = -D_x \frac{\partial \Theta_x}{\partial x} \quad \text{at } x = a, \quad (3.18b)$$

$$k_{ty0}w = -D_y \frac{\partial^2 \Theta_y}{\partial y^2}, \quad k_{ry0}\Theta_y = D_y \frac{\partial \Theta_y}{\partial y} \quad \text{at } y = 0, \quad (3.18c)$$

$$k_{ty1}w = D_y \frac{\partial^2 \Theta_y}{\partial y^2}, \quad k_{ry1}\Theta_y = -D_y \frac{\partial \Theta_y}{\partial y} \quad \text{at } y = b. \quad (3.18d)$$

A summary of the equations representing boundary conditions depending on spring constants (at the exemplary plate edge  $x = 0$ ) are given in Tab. 3.1.

As needed in the Rayleigh-Ritz method, the strain energy stored in translational and rotational springs,  $U_b$ , utilizing the non-dimensional coordinates  $(\xi, \eta)$ , is given by:

$$U_b = \frac{1}{2\alpha_p} \left[ \int_0^1 a \left\{ (k_{tx0}w^2 + k_{rx0}\Theta_x^2) \Big|_{\xi=0} + (k_{tx1}w^2 + k_{rx1}\Theta_x^2) \Big|_{\xi=1} \right\} d\eta \right. \\ \left. + \alpha_p^2 \int_0^1 b \left\{ (k_{ty0}w^2 + k_{ry0}\Theta_y^2) \Big|_{\eta=0} + (k_{ty1}w^2 + k_{ry1}\Theta_y^2) \Big|_{\eta=1} \right\} d\xi \right]. \quad (3.19)$$

### 3.4 Additional elements

The casing walls considered in this dissertation are a subject of both passive and active control. For this purpose, different kinds of element are bonded to the walls surface—actuators, sensors, additional masses and ribs (stiffeners). They have strong impact on the plate dynamical behaviour and have to be included in the mathematical modelling, so the model remains valid after the elements are attached to the plate surface.

In this section, mathematical modelling of additional masses and ribs bonded to plate surface is considered. Presence of sensors and actuators is also modelled as additional masses. Modelling of ribs includes the Engesser theory associated with the consideration of torsion (Engesser, 1891). The idea is presented schematically in Fig. 3.2. The symbols are summarized in the List of Symbols and discussed in details in this Section.

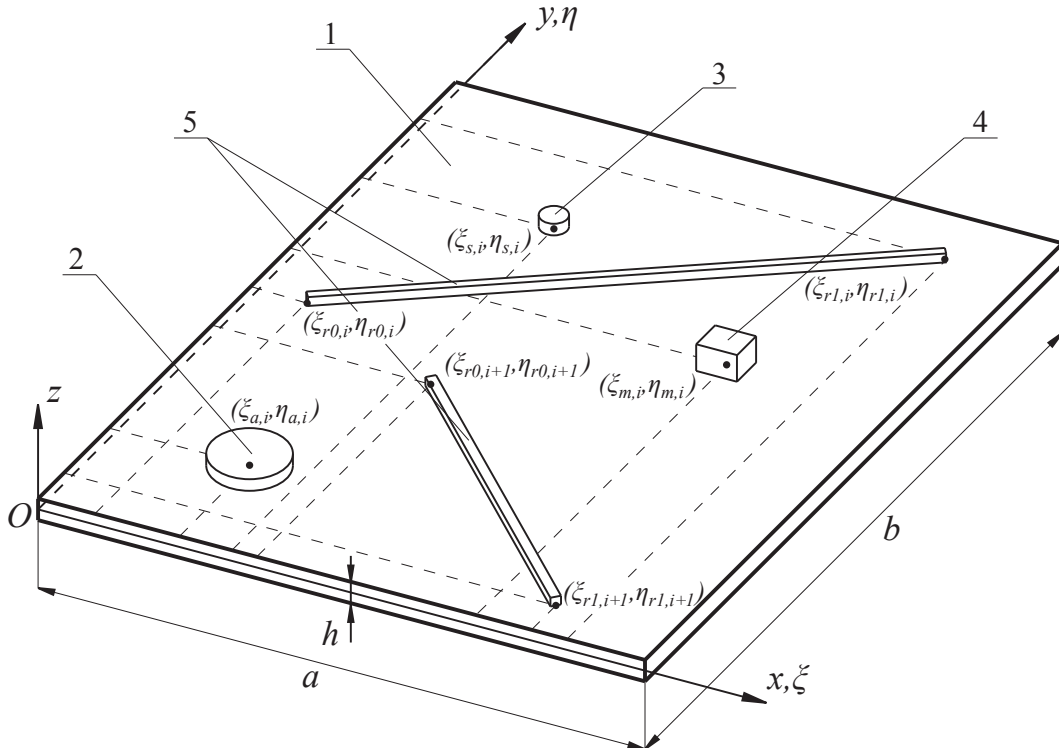


Figure 3.2: Rectangular plate (1) with actuators (2), sensors (3), additional masses (4) and ribs (5) bonded to its surface—a visualization in an isometric projection.

For the sake of brevity, mathematical modelling of additional elements is presented apart from differential system of the vibrating plate, defining only the kinetic and potential energy related to the elements (as they are most important for the Rayleigh-Ritz method used to solve the differential system).

### 3.4.1 Energy related to additional masses

Elements represented by additional masses in this dissertation (actuators, sensors and passive masses), can be for simplification (not limiting the analysis) considered of small size, compared to the dimensions of the plate. Therefore, an influence of strain caused by these elements bonded to the plate surface is neglected. Moreover, assuming perfect bonding, the total energy introduced to the system by the additional masses is considered to be the kinetic energy, expressed in the non-dimensional coordinates  $(\xi, \eta)$  as:

$$\begin{aligned} T_m = & \sum_{i=0}^{N_a} \frac{1}{2} \left\{ m_{a,i} \left( \frac{\partial w}{\partial t} \right)^2 + I_{ax,i} \left( \frac{\partial \Theta_x}{\partial t} \right)^2 + I_{ay,i} \left( \frac{\partial \Theta_y}{\partial t} \right)^2 \right\} \Big|_{\substack{\xi=\xi_{a,i} \\ \eta=\eta_{a,i}}} \\ & + \sum_{i=0}^{N_s} \frac{1}{2} \left\{ m_{s,i} \left( \frac{\partial w}{\partial t} \right)^2 + I_{sx,i} \left( \frac{\partial \Theta_x}{\partial t} \right)^2 + I_{sy,i} \left( \frac{\partial \Theta_y}{\partial t} \right)^2 \right\} \Big|_{\substack{\xi=\xi_{s,i} \\ \eta=\eta_{s,i}}} \\ & + \sum_{i=0}^{N_m} \frac{1}{2} \left\{ m_{m,i} \left( \frac{\partial w}{\partial t} \right)^2 + I_{mx,i} \left( \frac{\partial \Theta_x}{\partial t} \right)^2 + I_{my,i} \left( \frac{\partial \Theta_y}{\partial t} \right)^2 \right\} \Big|_{\substack{\xi=\xi_{m,i} \\ \eta=\eta_{m,i}}}, \end{aligned} \quad (3.20)$$

where  $N_\Gamma$ ,  $m_{\Gamma,i}$ ,  $I_{\Gamma x,i}$ ,  $I_{\Gamma y,i}$ ,  $\xi_{\Gamma,i}$  and  $\eta_{\Gamma,i}$  (depending of the kind of elements -  $\Gamma$  stand for:  $a$  for actuators,  $s$  for sensors and  $m$  for passive masses) are the number of elements bonded to the plate surface, mass of the  $i$ -th element, moments of inertia of the  $i$ -th element with respect to  $x$  and  $y$  directions, and coordinates of the  $i$ -th element, respectively.

### 3.4.2 Energy related to ribs

Assuming  $N_r$  stiffening ribs mounted on the plate surface, the total energy functionals related to the ribs can be expressed as:

$$T_r = \sum_{i=0}^{N_r} T_{r,i}, \quad (3.21a)$$

$$U_r = \sum_{i=0}^{N_r} U_{r,i}, \quad (3.21b)$$

where  $T_{r,i}$  and  $U_{r,i}$  are kinetic and potential energy of the  $i$ -th rib, respectively.

In the present considerations, the ribs can be mounted on the plate surface with any orientation, defined for the  $i$ -th rib by angle  $\alpha_i$ . Therefore, a local coordinates  $(\tilde{x}_{r,i}, \tilde{y}_{r,i})$  system have to be introduced (shown in Fig. 3.3), in which the energy functionals of

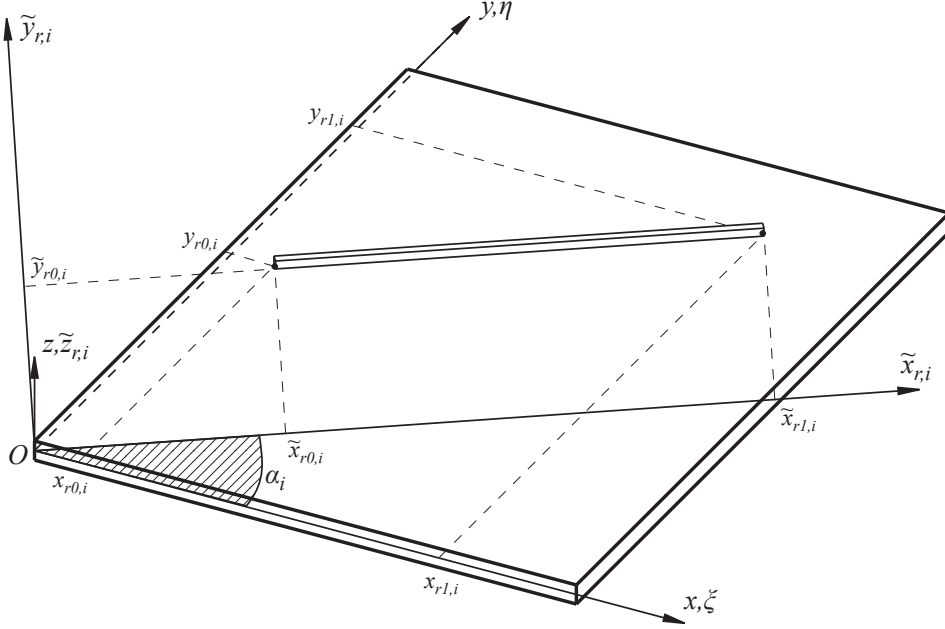


Figure 3.3: Rectangular plate with the  $i$ -th rib bonded to the plate surface, utilizing global and local coordinates systems.

the  $i$ -th rib are expressed as:

$$T_{r,i} = \frac{1}{2} A_{r,i} \rho_{r,i} \int_{\tilde{x}_{r0,i}}^{\tilde{x}_{r1,i}} \left\{ \left( \frac{\partial w}{\partial t} \right)^2 + k_{r,i} \left[ \left( \frac{\partial \Theta_{\tilde{x}_{r,i}}}{\partial t} \right)^2 + \left( \frac{\partial \Theta_{\tilde{y}_{r,i}}}{\partial t} \right)^2 \right] \right\} \Big|_{\tilde{y}_{r,i}=\tilde{y}_{r0,i}} d\tilde{x}_{r,i}, \quad (3.22a)$$

$$U_{r,i} = \frac{1}{2} \int_{\tilde{x}_{r0,i}}^{\tilde{x}_{r1,i}} \left\{ E_{r,i} I_{r,i} \left( \frac{\partial \Theta_{\tilde{x}_{r,i}}}{\partial \tilde{x}_{r,i}} \right)^2 + \frac{G_{r,i} A_{r,i}}{\beta_{r,i}} \left( \Theta_{\tilde{x}_{r,i}} + \frac{\partial w}{\partial \tilde{x}_{r,i}} \right) + G_{r,i} J_{r,i} \left( \frac{\partial \Theta_{\tilde{y}_{r,i}}}{\partial \tilde{x}_{r,i}} \right)^2 \right\} \Big|_{\tilde{y}_{r,i}=\tilde{y}_{r0,i}} d\tilde{x}_{r,i}, \quad (3.22b)$$

where  $\tilde{x}_{r0,i}$  and  $\tilde{x}_{r1,i}$  are the coordinates of the start and end points of the  $i$ -th rib, assuming that the ribs are mounted along the  $\tilde{x}_{r,i}$  direction;  $\tilde{y}_{r0,i}$  is the location of the  $i$ -th rib along the  $\tilde{y}_{r,i}$  direction; the functions  $\Theta_{\tilde{x}_{r,i}}$  and  $\Theta_{\tilde{y}_{r,i}}$  denote the cross-sectional rotations of the plate mid-plane in the  $\tilde{x}_{r,i}$  and  $\tilde{y}_{r,i}$  directions, respectively;  $E_{r,i}$  is a Young modulus;  $I_{r,i}$  is a second moment of inertia about the plate mid-plane;  $G_{r,i}$  is a shear modulus;  $A_{r,i}$  is a cross-sectional area;  $\beta_{r,i}$  is a shape factor;  $J_{r,i}$  is a torsional constant;  $\rho_{r,i}$  is a mass density; and  $k_{r,i}$  is a radius of gyration of the  $i$ -th rib.

The relation between the global  $(x, y)$  and the local  $(\tilde{x}_{r,i}, \tilde{y}_{r,i})$  coordinate systems can be expressed as:

$$x = \tilde{x}_{r,i} \cos \alpha_i - \tilde{y}_{r,i} \sin \alpha_i, \quad (3.23a)$$

$$y = \tilde{x}_{r,i} \sin \alpha_i + \tilde{y}_{r,i} \cos \alpha_i. \quad (3.23b)$$

The partial derivatives are related by:

$$\frac{\partial}{\partial \tilde{x}_{r,i}} = \cos \alpha_i \frac{\partial}{\partial x} + \sin \alpha_i \frac{\partial}{\partial y}. \quad (3.24)$$

The relationship between the rotations of the plate mid-plane in global coordinates and in local coordinates may be derived as:

$$\Theta_{\tilde{x}_{r,i}} = \Theta_x \cos \alpha_i + \Theta_y \sin \alpha_i, \quad (3.25a)$$

$$\Theta_{\tilde{y}_{r,i}} = -\Theta_x \sin \alpha_i + \Theta_y \cos \alpha_i. \quad (3.25b)$$

Considering (3.23)-(3.25), the energy functionals (3.22) for the  $i$ -th rib can be transformed from the local coordinate system into the global coordinate system as below:

$$T_{r,i} = \frac{1}{2 \cos \alpha_i} A_{r,i} \rho_{r,i} \int_{x_{r0,i}}^{x_{r1,i}} \left\{ \left( \frac{\partial w}{\partial t} \right)^2 + k_{r,i} \left[ \left( \frac{\partial \Theta_x}{\partial t} \right)^2 + \left( \frac{\partial \Theta_y}{\partial t} \right)^2 \right] \right\} \Big|_{y=f_{r,i}(x)} dx, \quad (3.26a)$$

$$U_{r,i} = \frac{1}{2 \cos \alpha_i} \int_{x_{r0,i}}^{x_{r1,i}} \left\{ E_{r,i} I_{r,i} \left[ \cos^2 \alpha_i \frac{\partial \Theta_x}{\partial x} + \sin \alpha_i \cos \alpha_i \left( \frac{\partial \Theta_x}{\partial y} + \frac{\partial \Theta_y}{\partial x} \right) + \sin^2 \alpha_i \frac{\partial \Theta_y}{\partial y} \right]^2 \right. \\ \left. + \frac{G_{r,i} A_{r,i}}{\beta_{r,i}} \left[ \cos \alpha_i \left( \Theta_x + \frac{\partial w}{\partial x} \right) + \sin \alpha_i \left( \Theta_y + \frac{\partial w}{\partial y} \right) \right]^2 \right. \\ \left. + G_{r,i} J_{r,i} \left[ \cos^2 \alpha_i \frac{\partial \Theta_y}{\partial x} - \sin \alpha_i \cos \alpha_i \left( \frac{\partial \Theta_x}{\partial x} - \frac{\partial \Theta_y}{\partial y} \right) - \sin^2 \alpha_i \frac{\partial \Theta_x}{\partial y} \right]^2 \right\} \Big|_{y=f_{r,i}(x)} dx. \quad (3.26b)$$

Then, utilizing the non-dimensional coordinates  $(\xi, \eta)$ , (3.26) can be expressed as:

$$T_{r,i} = \frac{a}{2 \cos \alpha_i} A_{r,i} \rho_{r,i} \int_{\xi_{r0,i}}^{\xi_{r1,i}} \left\{ \left( \frac{\partial w}{\partial t} \right)^2 + k_{r,i} \left[ \left( \frac{\partial \Theta_x}{\partial t} \right)^2 + \left( \frac{\partial \Theta_y}{\partial t} \right)^2 \right] \right\} \Big|_{\eta=g_{r,i}(\xi)} d\xi, \quad (3.27a)$$

$$U_{r,i} = \frac{a}{2 \cos \alpha_i} \int_{\xi_{r0,i}}^{\xi_{r1,i}} \left\{ E_{r,i} I_{r,i} \left[ \frac{\cos^2 \alpha_i}{a} \frac{\partial \Theta_x}{\partial \xi} + \sin \alpha_i \cos \alpha_i \left( \frac{1}{b} \frac{\partial \Theta_x}{\partial \eta} + \frac{1}{a} \frac{\partial \Theta_y}{\partial \xi} \right) + \frac{\sin^2 \alpha_i}{b} \frac{\partial \Theta_y}{\partial \eta} \right]^2 \right. \\ \left. + \frac{G_{r,i} A_{r,i}}{\beta_{r,i}} \left[ \cos \alpha_i \left( \Theta_x + \frac{1}{a} \frac{\partial w}{\partial \xi} \right) + \sin \alpha_i \left( \Theta_y + \frac{1}{b} \frac{\partial w}{\partial \eta} \right) \right]^2 \right. \\ \left. + G_{r,i} J_{r,i} \left[ \frac{\cos^2 \alpha_i}{a} \frac{\partial \Theta_y}{\partial \xi} - \sin \alpha_i \cos \alpha_i \left( \frac{1}{a} \frac{\partial \Theta_x}{\partial \xi} - \frac{1}{b} \frac{\partial \Theta_y}{\partial \eta} \right) - \frac{\sin^2 \alpha_i}{b} \frac{\partial \Theta_x}{\partial \eta} \right]^2 \right\} \Big|_{\eta=g_{r,i}(\xi)} d\xi. \quad (3.27b)$$

### 3.5 Total energy functional

In the previous three sections of this Chapter, the mathematical model of the vibrating plate, elastic boundary conditions and additional elements bonded to the plate surface is presented. To employ the Rayleigh-Ritz method, the total energy functional have to be defined. Summarising, the maximum strain energy of the system,  $U$ , can be expressed as:

$$U = U_p + U_b + U_r , \quad (3.28)$$

where  $U_p$ ,  $U_b$  and  $U_r$  are potential energies corresponding to plate strain, boundary restraints, and ribs, respectively.

The maximum kinetic energy of the system,  $T$ , can be defined as:

$$T = T_p + T_m + T_r , \quad (3.29)$$

where  $T_p$ ,  $T_m$  and  $T_r$  are kinetic energies of the plate, additional masses and ribs, respectively.

### 3.6 The Rayleigh-Ritz method

The Rayleigh-Ritz method is used to calculate approximate solution of the presented differential system, obtaining natural frequencies and modeshapes of the system. To utilize this method, the total energy of the system needs to be defined (which is derived in the previous sections) and appropriate admissible functions, which satisfy the geometric boundary conditions have to be chosen. More detailed informations regarding the Rayleigh-Ritz method are provided in (Young, 1950).

For free vibration of the plate, the solution of  $w$ ,  $\Theta_x$  and  $\Theta_y$  can be expressed in a required form using a set of appropriate trial functions:

$$w(\xi, \eta, t) = \sum_{i=1}^N \phi_i(\xi, \eta) q_i(t) = \boldsymbol{\phi}^T \mathbf{q} , \quad (3.30a)$$

$$\Theta_x(\xi, \eta, t) = \sum_{i=1}^N \psi_{x,i}(\xi, \eta) p_{x,i}(t) = \boldsymbol{\psi}_x^T \mathbf{p}_x , \quad (3.30b)$$

$$\Theta_y(\xi, \eta, t) = \sum_{i=1}^N \psi_{y,i}(\xi, \eta) p_{y,i}(t) = \boldsymbol{\psi}_y^T \mathbf{p}_y , \quad (3.30c)$$

where  $\mathbf{q}$ ,  $\mathbf{p}_x$  and  $\mathbf{p}_y$  are a generalized plate displacement vector, generalized plate rotations vectors in the  $x$  and  $y$  directions, respectively;  $\boldsymbol{\phi}$ ,  $\boldsymbol{\psi}_x$  and  $\boldsymbol{\psi}_y$  are vectors, which represent a set of time-invariant trial functions—in this dissertation, characteristic orthogonal polynomials having the property of Timoshenko beam functions are used; the superscript T denotes the transpose. All of mentioned vectors are of dimension ( $N \times 1$ ).

The procedure for forming orthogonal polynomial trial functions for Mindlin plates is described in details in (Kim et al., 2012).

### 3.6.1 Energy definition

Utilizing (3.30), the total potential and kinetic energies defined in (3.28) and (3.29) can also be written as functions of generalized plate displacement and rotations vectors  $\mathbf{q}$ ,  $\mathbf{p}_x$ ,  $\mathbf{p}_y$ , mass matrix  $\mathbf{M}$  of dimension  $(3N \times 3N)$  and stiffness matrix  $\mathbf{K}$  of dimension  $(3N \times 3N)$ :

$$U = \frac{1}{2} \begin{bmatrix} \mathbf{q} \\ \mathbf{p}_x \\ \mathbf{p}_y \end{bmatrix}^T \mathbf{K} \begin{bmatrix} \mathbf{q} \\ \mathbf{p}_x \\ \mathbf{p}_y \end{bmatrix}, \quad (3.31)$$

$$T = \frac{1}{2} \begin{bmatrix} \dot{\mathbf{q}} \\ \dot{\mathbf{p}}_x \\ \dot{\mathbf{p}}_y \end{bmatrix}^T \mathbf{M} \begin{bmatrix} \dot{\mathbf{q}} \\ \dot{\mathbf{p}}_x \\ \dot{\mathbf{p}}_y \end{bmatrix}, \quad (3.32)$$

where matrices  $\mathbf{K}$  and  $\mathbf{M}$  are defined in following Subsections.

### 3.6.2 Stiffness matrix

The overall stiffness matrix  $\mathbf{K}$  is calculated as a sum of stiffness matrices related to different energy components:

$$\mathbf{K} = \mathbf{K}_p + \mathbf{K}_b + \mathbf{K}_r, \quad (3.33)$$

where  $\mathbf{K}_p$ ,  $\mathbf{K}_b$  and  $\mathbf{K}_r$  correspond to strain energy of the plate, potential energy stored in boundary restraints and potential energy related to ribs mounted on the plate surface, respectively.

Stiffness matrices introduced in (3.33) are defined as:

$$\mathbf{K}_p = \begin{bmatrix} \mathbf{K}_{pcc} & \mathbf{K}_{pcd} & \mathbf{K}_{pee} \\ & \mathbf{K}_{pdd} & \mathbf{K}_{pde} \\ & & \mathbf{K}_{pee} \end{bmatrix}_{symm.}, \quad \mathbf{K}_b = \begin{bmatrix} \mathbf{K}_{bcc} & \mathbf{0}_{N,N} & \mathbf{0}_{N,N} \\ & \mathbf{K}_{bdd} & \mathbf{0}_{N,N} \\ & & \mathbf{K}_{bee} \end{bmatrix}_{symm.}, \quad \mathbf{K}_r = \begin{bmatrix} \mathbf{K}_{rcc} & \mathbf{K}_{rcd} & \mathbf{K}_{ree} \\ & \mathbf{K}_{rdd} & \mathbf{K}_{rde} \\ & & \mathbf{K}_{ree} \end{bmatrix}_{symm.}, \quad (3.34)$$

where  $\mathbf{0}_{N,N}$  denotes a zero matrix of dimension  $(N \times N)$ . Detailed definitions of sub-matrices used in (3.34) are given in Appendix A for convenience of the reader. They, in fact, can be obtained for the considered problem based on the literature (Liew et al., 1994), but the derivation is nontrivial and combines more components.

### 3.6.3 Mass matrix

The overall mass matrix  $\mathbf{M}$  is calculated similarly to the stiffness matrix - as a sum of matrices related to different energy components:

$$\mathbf{M} = \mathbf{M}_p + \mathbf{M}_m + \mathbf{M}_r , \quad (3.35)$$

where  $\mathbf{M}_p$ ,  $\mathbf{M}_m$  and  $\mathbf{M}_r$  correspond to kinetic energy of the plate, kinetic energy of additional masses and kinetic energy related to ribs, respectively.

Mass matrices introduced in (3.35) are defined as:

$$\mathbf{M}_p = \begin{bmatrix} \mathbf{M}_{pcc} & \mathbf{0}_{N,N} & \mathbf{0}_{N,N} \\ & \mathbf{M}_{pdd} & \mathbf{0}_{N,N} \\ & & \mathbf{M}_{pee} \end{bmatrix}_{symm.}, \quad \mathbf{M}_m = \begin{bmatrix} \mathbf{M}_{mcc} & \mathbf{0}_{N,N} & \mathbf{0}_{N,N} \\ & \mathbf{M}_{mdm} & \mathbf{0}_{N,N} \\ & & \mathbf{M}_{mee} \end{bmatrix}_{symm.}, \quad \mathbf{M}_r = \begin{bmatrix} \mathbf{M}_{rcr} & \mathbf{0}_{N,N} & \mathbf{0}_{N,N} \\ & \mathbf{M}_{rdd} & \mathbf{0}_{N,N} \\ & & \mathbf{M}_{ree} \end{bmatrix}_{symm.}. \quad (3.36)$$

Detailed definitions of submatrices used in (3.36) are given in Appendix B. Similarly, as in case of Appendix A, they could be obtained using (Nicholson and Bergman, 1985), but presented definitions are given in a convenient form consistent with previous derivations.

### 3.6.4 Equation of the vibrating structure and a harmonic solution

When the stiffness and mass matrices are defined, by using the Lagrange equation of the second kind, the equation of a vibrating structure can be obtained as:

$$\mathbf{M} \begin{bmatrix} \ddot{\mathbf{q}} \\ \ddot{\mathbf{p}}_x \\ \ddot{\mathbf{p}}_y \end{bmatrix} + \mathbf{K} \begin{bmatrix} \mathbf{q} \\ \mathbf{p}_x \\ \mathbf{p}_y \end{bmatrix} = \mathbf{Q} , \quad (3.37)$$

where  $\mathbf{Q}$  is the vector of generalized forces of dimension  $(3N \times 1)$ . In this dissertation, inertial actuators are considered. Hence, for the purpose of positioning, their action can be simplified and taken into account as a force acting on a point. Therefore, the control vector  $\mathbf{u}$  of dimension  $(N_a \times 1)$  can be defined as:

$$\mathbf{u} = [f_1, f_2, \dots, f_{N_a}]^T , \quad (3.38)$$

where  $f_i$  is a force generated by a  $i$ -th actuator. Then, the vector of generalized forces can be expressed as:

$$\mathbf{Q} = \left[ \begin{bmatrix} \phi \Big|_{\substack{\xi=\xi_{a,1} \\ \eta=\eta_{a,1}}, \phi \Big|_{\substack{\xi=\xi_{a,2} \\ \eta=\eta_{a,2}}, \dots, \phi \Big|_{\substack{\xi=\xi_{a,N_a} \\ \eta=\eta_{a,N_a}}} } \mathbf{u} \\ \mathbf{0}_{2N,1} \end{bmatrix} \right] , \quad (3.39)$$

The harmonic solution to (3.37) gives the eigenvector matrix  $\Phi$  of dimension  $(3N \times 3N)$  and  $(3N)$  eigenfrequencies  $\omega_i$ . Replacing  $\begin{bmatrix} \mathbf{q}, \mathbf{p}_x, \mathbf{p}_y \end{bmatrix}^T$  by  $\Phi\mathbf{v}$ , and multiplying (3.37) on the left by  $\Phi^T$ , it gives:

$$\Phi^T \mathbf{M} \Phi \ddot{\mathbf{v}} + \Phi^T \mathbf{K} \Phi \mathbf{v} = \Phi^T \mathbf{Q}, \quad (3.40)$$

where  $\mathbf{v}$  denotes a modal displacement vector of dimension  $(3N \times 1)$ :

$$\mathbf{v} = [v_1, v_2, \dots, v_{(3N)}]^T. \quad (3.41)$$

Taking advantage of the orthonormality of eigenvectors in matrix  $\Phi$ , the modal mass matrix becomes a unit matrix  $\mathbf{I}_{(3N)}$  of dimension  $(3N \times 3N)$  and the corresponding modal stiffness matrix becomes a diagonal matrix  $\Omega$  of  $(3N)$  eigenvalues  $\omega_i^2$  (Craig and Kurdila, 2006):

$$\Phi^T \mathbf{M} \Phi = \mathbf{I}_{(3N)}, \quad (3.42)$$

$$\Phi^T \mathbf{K} \Phi = \Omega = \left[ \text{diag}(\omega_1^2, \omega_2^2, \dots, \omega_{(3N)}^2) \right]. \quad (3.43)$$

Then, by substituting (3.42) and (3.43) to (3.40), it gives:

$$\ddot{\mathbf{v}} + \Omega \mathbf{v} = \Phi^T \mathbf{Q}. \quad (3.44)$$

For a better reference to a real system behaviour this equation is extended to the following one:

$$\ddot{\mathbf{v}} + \Xi \dot{\mathbf{v}} + \Omega \mathbf{v} = \Phi^T \mathbf{Q}, \quad (3.45)$$

where  $\Xi \dot{\mathbf{v}}$  is a term introduced to include the damping in the system, and  $\Xi$  is a diagonal matrix of dimension  $(3N \times 3N)$  defined as:

$$\Xi = \left[ \text{diag}(2\xi_{d,1}\omega_1, 2\xi_{d,2}\omega_2, \dots, 2\xi_{d,(3N)}\omega_{(3N)}) \right]. \quad (3.46)$$

In (3.46) the damping ratios,  $0 < \xi_{d,i} < 1$ , are calculated with use of the thermoelastic damping model for elastic plates described in details in (Norris and Photiadis, 2005). The damping mechanism could be also included at the beginning of the modelling in the form of complex bending rigidities. However, it would substantially complicate the derivation. Introducing it at this point preserves the brevity of derivation and leads to equivalent solution. Such approach was also used in (Leleu et al., 2001).

### 3.7 State space model

Equation (3.45) can be written in the usual state-space form:

$$\dot{\mathbf{x}} = \mathbf{A}\mathbf{x} + \mathbf{B}\mathbf{u} \quad (3.47a)$$

$$\mathbf{y} = \mathbf{C}\mathbf{x} + \mathbf{D}\mathbf{u} \quad (3.47b)$$

with the output vector  $\mathbf{y}$  of dimension  $(N_s \times 1)$ :

$$\mathbf{y} = [y_1, y_2, \dots, y_{N_s}]^T, \quad (3.48)$$

and the state vector  $\mathbf{x}$  of dimension  $(6N \times 1)$ :

$$\mathbf{x} = [\dot{v}_1, \omega_1 v_1, \dot{v}_2, \omega_2 v_2, \dots, \dot{v}_{3N}, \omega_{3N} v_{3N}]^T. \quad (3.49)$$

The state matrix  $\mathbf{A} = [\text{diag}(\mathbf{A}_1, \mathbf{A}_2, \dots, \mathbf{A}_{3N})]$  of dimension  $(6N \times 6N)$ , is defined by:

$$\mathbf{A}_i = \begin{bmatrix} -2\xi_{d,i}\omega_i & -\omega_i \\ \omega_i & 0 \end{bmatrix}, \quad i = 1, 2, \dots, 3N. \quad (3.50)$$

Matrix  $\mathbf{B}$  of dimension  $(6N \times N_a)$  can be expressed as:

$$\mathbf{B} = [\text{diag}(\mathbf{b}_1, \mathbf{b}_2, \dots, \mathbf{b}_{3N})] \Phi^T \begin{bmatrix} \left[ \phi \Big|_{\substack{\xi=\xi_{a,1} \\ \eta=\eta_{a,1}}}, \phi \Big|_{\substack{\xi=\xi_{a,2} \\ \eta=\eta_{a,2}}}, \dots, \phi \Big|_{\substack{\xi=\xi_{a,N_a} \\ \eta=\eta_{a,N_a}}} \right] \\ \mathbf{0}_{2N, N_a} \end{bmatrix}, \quad (3.51)$$

where  $\mathbf{b}_i = [1 \ 0]^T$ .

Considering accelerometers as the sensors, the output matrix  $\mathbf{C}$  of dimension  $(N_s \times 6N)$  is defined by:

$$\mathbf{C} = \begin{bmatrix} \phi^T \Big|_{\substack{\xi=\xi_{s,1} \\ \eta=\eta_{s,1}}} \\ \phi^T \Big|_{\substack{\xi=\xi_{s,2} \\ \eta=\eta_{s,2}}} \\ \vdots \\ \phi^T \Big|_{\substack{\xi=\xi_{s,N_s} \\ \eta=\eta_{s,N_s}}} \end{bmatrix} \Phi [\text{diag}(\mathbf{c}_1, \mathbf{c}_2, \dots, \mathbf{c}_{3N})], \quad (3.52)$$

where  $\mathbf{c}_i = [-2\xi_{d,i}\omega_i, -\omega_i]$ . Matrix  $\mathbf{D}$  of dimension  $(N_s \times N_a)$  can be calculated as:

$$\mathbf{D} = \begin{bmatrix} \phi^T \Big|_{\substack{\xi=\xi_{s,1} \\ \eta=\eta_{s,1}}} \\ \phi^T \Big|_{\substack{\xi=\xi_{s,2} \\ \eta=\eta_{s,2}}} \\ \vdots \\ \phi^T \Big|_{\substack{\xi=\xi_{s,N_s} \\ \eta=\eta_{s,N_s}}} \end{bmatrix} \begin{bmatrix} \phi \Big|_{\substack{\xi=\xi_{a,1} \\ \eta=\eta_{a,1}}}, \phi \Big|_{\substack{\xi=\xi_{a,2} \\ \eta=\eta_{a,2}}}, \dots, \phi \Big|_{\substack{\xi=\xi_{a,N_a} \\ \eta=\eta_{a,N_a}}} \end{bmatrix}. \quad (3.53)$$

### 3.8 Controllability and observability

Taking advantage of the fact that the model is expressed in the state-space form, classical methods can be used to describe the controllability and observability of the system (Klamka, 2013). The method presented in this Section represents the energy-based approach, and it is used later in the optimization process for active control scenarios (see Section 5.4).

The control energy required to reach the desired state  $\mathbf{x}_{T_1}$  at time  $t = T_1$ , assuming the optimal solution, can be expressed as:

$$E_c = \int_0^{T_1} \mathbf{u}^T(t) \mathbf{u}(t) dt = (\mathbf{e}^{\mathbf{A}T_1} \mathbf{x}_0 - \mathbf{x}_{T_1})^T \mathbf{W}^{-1}(T_1) (\mathbf{e}^{\mathbf{A}T_1} \mathbf{x}_0 - \mathbf{x}_{T_1}), \quad (3.54)$$

where  $\mathbf{W}(T_1)$  is the controllability Gramian matrix of dimension  $(6N \times 6N)$ . To minimize control required energy with respect to the actuators locations, a measure of the Gramian matrix should be maximized. It has been shown in the literature that instead of using  $\mathbf{W}(T_1)$ , a steady state controllability Gramian matrix,  $\mathbf{W}_c$ , can be used for stable systems, when time tends to infinity (Anderson and Moore, 2007).

Analogously, the output energy received by the sensors, when the system starts in initial state  $\mathbf{x}_0$  and is not controlled, can be written as:

$$E_o = \int_0^{\infty} \mathbf{y}^T(t) \mathbf{y}(t) dt = \mathbf{x}_0^T \left( \int_0^{\infty} \mathbf{e}^{\mathbf{A}^T t} \mathbf{C}^T \mathbf{C} \mathbf{e}^{\mathbf{A}^T t} dt \right) \mathbf{x}_0 = \mathbf{x}_0^T \mathbf{W}_o \mathbf{x}_0, \quad (3.55)$$

where  $\mathbf{W}_o$  is the observability Gramian matrix of dimension  $(6N \times 6N)$ . To maximize output energy with respect to the sensors locations, again a measure of the Gramian matrix should be maximized.

Both controllability and observability Gramian matrices can be calculated by solving the Lyapunov equations:

$$\mathbf{A}\mathbf{W}_c + \mathbf{W}_c\mathbf{A}^T + \mathbf{B}\mathbf{B}^T = 0. \quad (3.56a)$$

$$\mathbf{A}^T\mathbf{W}_o + \mathbf{W}_o\mathbf{A} + \mathbf{C}^T\mathbf{C} = 0. \quad (3.56b)$$

The controllability and observability Gramian matrices are convenient to use, because if the  $(2i)$ -th value at the diagonal of the matrix, corresponding to the  $i$ -th eigenmode is small, the eigenmode is difficult to control (it can be regulated only if a large control energy is available) or is not observable well, respectively. Such information can be an important criterion in the optimization process of actuators and sensors placement.

Formally, controllability and observability are dichotomous properties, but "controllable" and "observable" does not say how high control effort is needed to reach the final state and how much energy is received by the sensors.

### **3.9 Summary**

The mathematical model of the device casing walls has been developed in this Chapter. The model includes thin and thick plate theory, elastically restrained boundary conditions, structural thermoelastic damping model, and additional elements mounted to the casing surface—masses, ribs, actuators and sensors. These aspects are integrated in a state space model form, which facilitates further analysis and numerical simulation.

The model can be used to predict natural frequencies and modeshapes of a casing walls or other panels. If active control is concerned, it can be used also to calculate measures of controllability and observability of the system.

# **Chapter 4**

# **Validation and analysis of the model**

## **4.1 Background**

Before the mathematical model developed in the previous Chapter can be used for an extensive analysis and optimization of vibrating structures, it have to be carefully validated. For this purpose, results obtained by the model for various cases are compared with results of other numerical methods and laboratory experiments (including results obtained with the Finite Elements Method (FEM) utilizing ANSYS, experiments performed by the author and reports of other authors available in the literature). The model is validated by means of a comparison of natural frequencies, modeshapes and frequency response functions.

In experiments performed by the author, measurements of natural frequencies and modeshapes are made with a laser vibrometer PDV-100 (measuring the normal plate velocity in a large number of points). A loudspeaker placed on the bottom of the casing is used as the noise source exciting the casing walls and making them vibrate. A random wideband signal is used as the excitation. Due to the close distance between the walls and the loudspeaker, not all of the eigenmodes in the considered frequency range are excited equally. Some of the less excited eigenmodes are even difficult to observe, because of vicinity of more excited ones. This is, however, a problem met if a real device is enclosed in the casing, and therefore it should not be artificially mitigated.

This Chapter is structured as follows. Firstly, in Section 4.2 the results obtained with the developed model are compared with results available in the literature for individual plates—including theoretical and experimental results. Both unloaded and loaded plates are considered. Subsequently, in Section 4.3 experiments performed by the author are used to validate the model accuracy for active casing walls.

## **4.2 Comparison with the individual plates**

In this Section, the developed model is evaluated for different individual plates considered in the literature. Many of them constitute benchmarks for evaluation of plate models and they are used broadly in a number of publications. The studied examples are presented starting with simple scenarios. Subsequently, more complex ones are considered.

### 4.2.1 Unloaded plate

In this Subsection, the comparison is made by means of the non-dimensional frequency parameters  $\lambda$ , as they are commonly used in the literature. Different formulations for the  $\lambda$  parameters are used, depending on the considered case (the formulation is always given for each of the tables presenting results). For the sake of brevity, for each case initial six eigenmodes are evaluated. However, they are representative as a similar accuracy is obtained for following ones.

#### Isotropic thin plate with classical boundary conditions

The first example for evaluation of the developed model is an isotropic thin plate with classical boundary conditions. The utilized notation of boundary conditions is similar to the one defined in (Leissa, 1969), where S denotes a simply-supported edge, C stands for a fully-clamped edge and F means a free edge (these classical boundary conditions are limiting cases of elastically restrained boundary conditions, as described in Section 3.3). For a complete plate definition, four symbols have to be used, e.g. SCSF identifies a rectangular plate with edges  $x = 0, y = 0, x = a, y = b$  having simply-supported, fully-clamped, simply-supported, and free boundary conditions, respectively.

The obtained results are compared with values given in following publications:

- (Leissa, 1969), where the classical Kirchhoff-Love thin plate theory has been used;
- (Mindlin et al., 1956), where analytical solutions for the Mindlin-Reissner thick plate theory are given;
- (Dawe and Roufaeil, 1980), where Rayleigh-Ritz method is used with the Mindlin-Reissner plate theory (analytical solutions are available only for selected cases of boundary conditions);
- (Dawe, 1978), where Finite Strip Models are used, also utilizing Mindlin-Reissner plate theory.

The results calculated for a set of four boundary conditions, SSSS, SCSC, CCCC, CCCF, are given in Tabs. 4.1-4.4, respectively. Although there are differences in values calculated with different methods, they are of negligible magnitude and all of evaluated methods provide consistent results.

Table 4.1: Frequency parameters  $\lambda = \omega \sqrt{2(1 + \nu)\rho_p a^2/E}$  for thin square **SSSS** plate:  
 $h/a = \mathbf{0.01}$ ,  $\nu = 0.3$ ,  $\kappa = 0.822$ .

Mode	Present dissertation	(Mindlin et al., 1956)	(Dawe, 1978)	(Leissa, 1969)
	Developed model	Mindlin's	FSM	Classical
1	0.0963	0.0963	0.0963	0.0963
2	0.2407	0.2406	0.2406	0.2408
3	0.2407	0.2406	0.2406	0.2408
4	0.3850	0.3847	0.3847	0.3853
5	0.4808	0.4807	0.4807	0.4816
6	0.4808	0.4807	0.4807	0.4816

Table 4.2: Frequency parameters  $\lambda = \omega \sqrt{2(1 + \nu)\rho_p a^2/E}$  for thin square **SCSC** plate:  
 $h/a = \mathbf{0.01}$ ,  $\nu = 0.3$ ,  $\kappa = 0.822$ .

Mode	Present dissertation	(Dawe and Roufaeil, 1980)	(Dawe, 1978)	(Leissa, 1969)
	Developed model	Mindlin's	FSM	Classical
1	0.1411	0.1411	0.1411	0.1413
2	0.2668	0.2668	0.2668	0.2671
3	0.3373	0.3377	0.3376	0.3383
4	0.4602	0.4608	0.4604	0.4615
5	0.4977	0.4979	0.4977	0.4988
6	0.6270	0.6279	0.6279	0.6299

Table 4.3: Frequency parameters  $\lambda = \omega \sqrt{2(1 + \nu)\rho_p a^2/E}$  for thin square **CCCC** plate:  
 $h/a = \mathbf{0.01}$ ,  $\nu = 0.3$ ,  $\kappa = 0.860$ .

Mode	Present dissertation	(Dawe and Roufaeil, 1980)	(Leissa, 1969)
	Developed model	Mindlin's	Classical
1	0.1754	0.1754	0.1756
2	0.3570	0.3576	0.3581
3	0.3570	0.3576	0.3581
4	0.5259	0.5274	0.5280
5	0.6390	0.6402	0.6421
6	0.6421	0.6432	0.6451

Table 4.4: Frequency parameters  $\lambda = \omega \sqrt{2(1 + \nu)\rho_p a^2/E}$  for thin square **CCCF** plate:  
 $h/a = \mathbf{0.01}$ ,  $\nu = 0.3$ ,  $\kappa = 0.860$ .

Mode	Present dissertation	(Dawe and Roufaeil, 1980)	(Leissa, 1969)
	Developed model	Mindlin's	Classical
1	0.1168	0.1171	0.1171
2	0.1948	0.1951	0.1953
3	0.3081	0.3093	0.3094
4	0.3732	0.3740	0.3744
5	0.3922	0.3931	0.3938
6	0.5671	0.5695	0.5699

### Isotropic thick plate with classical boundary conditions

In subsequent evaluation, a thick plate is considered, where plate thickness to length ratio  $h/a = 0.1$ . The same set of boundary conditions is used as for thin plate. The results are given in Tabs. 4.5-4.8.

The results obtained with the method using Mindlin-Reissner plate theory provided consistent results (including the developed model). However, classical Kirchhoff-Love plate theory is no longer valid for plates of such thickness (the obtained errors may exceed 20%).

Table 4.5: Frequency parameters  $\lambda = \omega \sqrt{2(1 + \nu)\rho_p a^2/E}$  for thick square **SSSS** plate:  
 $h/a = \mathbf{0.1}$ ,  $\nu = 0.3$ ,  $\kappa = 0.822$ .

Mode	Present dissertation		(Mindlin et al., 1956)	(Dawe, 1978)	(Leissa, 1969)
	Developed model	Mindlin's	FSM	Classical	
1	0.930	0.930	0.930	0.963	
2	2.218	2.218	2.218	2.408	
3	2.218	2.218	2.218	2.408	
4	3.403	3.402	3.402	3.853	
5	4.145	4.144	4.144	4.816	
6	4.145	4.144	4.144	4.816	

Table 4.6: Frequency parameters  $\lambda = \omega \sqrt{2(1 + \nu)\rho_p a^2/E}$  for thick square **SCSC** plate:  
 $h/a = \mathbf{0.1}$ ,  $\nu = 0.3$ ,  $\kappa = 0.822$ .

Mode	Present dissertation		(Dawe and Roufaeil, 1980)	(Dawe, 1978)	(Leissa, 1969)
	Developed model	Mindlin's	FSM	Classical	
1	1.296	1.302	1.300	1.413	
2	2.398	2.398	2.394	2.671	
3	2.922	2.888	2.885	3.383	
4	3.878	3.852	3.839	4.615	
5	4.250	4.237	4.232	4.988	
6	4.951	4.939	4.936	6.299	

Table 4.7: Frequency parameters  $\lambda = \omega \sqrt{2(1 + \nu)\rho_p a^2/E}$  for thick square **CCCC** plate:  
 $h/a = \mathbf{0.1}$ ,  $\nu = 0.3$ ,  $\kappa = 0.860$ .

Mode	Present dissertation		(Dawe and Roufaeil, 1980)	(Leissa, 1969)
	Developed model	Mindlin's	Classical	
1	1.588	1.594	1.756	
2	3.073	3.046	3.581	
3	3.073	3.046	3.581	
4	4.314	4.285	5.280	
5	5.024	5.035	6.421	
6	5.071	5.078	6.451	

Table 4.8: Frequency parameters  $\lambda = \omega \sqrt{2(1 + \nu)\rho_p a^2/E}$  for thick square CCCF plate:  
 $h/a = 0.1, \nu = 0.3, \kappa = 0.860$ .

Mode	Present dissertation	(Dawe and Roufaeil, 1980)	(Leissa, 1969)
	Developed model	Mindlin's	Classical
1	1.077	1.089	1.171
2	1.740	1.758	1.953
3	2.694	2.673	3.094
4	3.192	3.216	3.744
5	3.320	3.318	3.938
6	4.578	4.615	5.699

### Isotropic plate with elastically restrained boundary conditions

In this evaluation, elastically restrained against rotation boundary conditions are used (uniform for all edges). Four values of rotational spring are used, starting with a value close to simply-supported edges, and finishing with a value approaching fully-clamped boundary conditions. Calculations are performed for a thick plate. Results obtained by the developed model are compared with results provided in (Chung et al., 1993), where authors used the Rayleigh-Ritz method. Comparisons are presented in Tabs. 4.9-4.12. It follows from the analysis that the developed model is highly consistent with the results reported in (Chung et al., 1993).

Table 4.9: Frequency parameters  $\lambda = \omega \sqrt{2(1 + \nu)\rho_p a^2/E}$  for square plate with edges elastically restrained against rotation:  $k_{rx0} = k_{rx1} = k_{ry0} = k_{ry1} = 10D/a, h/a = 0.1, \nu = 0.3, \kappa = 0.822$ .

Mode	Present dissertation	(Chung et al., 1993)	
	Developed model	Timoshenko beam functions	Polynomials
1	1.305	1.303	1.302
2	2.629	2.616	2.619
3	2.629	2.618	2.620
4	3.803	3.792	3.791
5	4.522	4.517	4.526
6	4.535	4.532	4.539

Table 4.10: Frequency parameters  $\lambda = \omega \sqrt{2(1 + \nu)\rho_p a^2/E}$  for square plate with edges elastically restrained against rotation:  $k_{rx0} = k_{rx1} = k_{ry0} = k_{ry1} = 50D/a, h/a = 0.1, \nu = 0.3, \kappa = 0.822$ .

Mode	Present dissertation	(Chung et al., 1993)	
	Developed model	Timoshenko beam functions	Polynomials
1	1.500	1.499	1.498
2	2.918	2.887	2.889
3	2.918	2.891	2.890
4	4.121	4.092	4.085
5	4.824	4.818	4.826
6	4.859	4.857	4.861

Table 4.11: Frequency parameters  $\lambda = \omega \sqrt{2(1 + \nu)\rho_p a^2/E}$  for square plate with edges elastically restrained against rotation:  $k_{rx0} = k_{rx1} = k_{ry0} = k_{ry1} = 100D/a$ ,  $h/a = 0.1$ ,  $\nu = 0.3$ ,  $\kappa = 0.822$ .

Mode	Present dissertation		(Chung et al., 1993)
	Developed model	Timoshenko beam functions	Polynomials
1	1.540	1.540	1.538
2	2.986	2.949	2.950
3	2.986	2.954	2.952
4	4.200	4.166	4.156
5	4.902	4.893	4.900
6	4.942	4.938	4.941

Table 4.12: Frequency parameters  $\lambda = \omega \sqrt{2(1 + \nu)\rho_p a^2/E}$  for square plate with edges elastically restrained against rotation:  $k_{rx0} = k_{rx1} = k_{ry0} = k_{ry1} = 1000D/a$ ,  $h/a = 0.1$ ,  $\nu = 0.3$ ,  $\kappa = 0.822$ .

Mode	Present dissertation		(Chung et al., 1993)
	Developed model	Timoshenko beam functions	Polynomials
1	1.582	1.582	1.580
2	3.058	3.016	3.016
3	3.058	3.021	3.018
4	4.287	4.246	4.234
5	4.984	4.977	4.982
6	5.031	5.028	5.029

### Orthotropic plate

The following evaluation is made for an orthotropic plate case. For the purpose of comparison, results given in (Dozio, 2011) and (Xing and Liu, 2009) are used, where two different orthotropic plate materials were considered—graphite/epoxy and boron/epoxy. Values of calculated frequency parameters are given in Tabs. 4.13-4.16. A satisfactory consistency have been obtained for all evaluated cases.

Table 4.13: Frequency parameters  $\lambda = a \sqrt[4]{\rho_p h \omega^2 / D_x}$  for **graphite/epoxy SSCC** plate:  $a/b = 0.833$ ,  $E_x = 185$  GPa,  $E_y = 10.5$  GPa,  $G_x = 7.3$  GPa,  $\nu_x = 0.28$ ,  $\kappa = 0.860$ .

Mode	Present dissertation		(Dozio, 2011)	(Xing and Liu, 2009)
	Developed model	Trigonometric Ritz method	Exact solutions	
1	4.016	4.019	4.02	
2	4.384	4.386	4.38	
3	5.092	5.098	5.09	
4	6.042	6.064	6.06	
5	7.101	7.115	7.12	
6	7.124	7.168	7.17	

Table 4.14: Frequency parameters  $\lambda = a \sqrt[4]{\rho_p h \omega^2 / D_x}$  for **graphite/epoxy SCCC plate**:  $a/b = 0.833$ ,  $E_x = 185$  GPa,  $E_y = 10.5$  GPa,  $G_x = 7.3$  GPa,  $\nu_x = 0.28$ ,  $\kappa = 0.860$ .

Mode	Present dissertation		(Dozio, 2011)	(Xing and Liu, 2009)
	Developed model	Trigonometric Ritz method	Exact solutions	
1	4.048	4.051	4.04	
2	4.504	4.500	4.49	
3	5.303	5.293	5.28	
4	6.300	6.310	6.30	
5	7.109	7.123	7.12	
6	7.293	7.307	7.30	

Table 4.15: Frequency parameters  $\lambda = a \sqrt[4]{\rho_p h \omega^2 / D_x}$  for **graphite/epoxy CCCC plate**:  $a/b = 0.833$ ,  $E_x = 185$  GPa,  $E_y = 10.5$  GPa,  $G_x = 7.3$  GPa,  $\nu_x = 0.28$ ,  $\kappa = 0.860$ .

Mode	Present dissertation		(Dozio, 2011)	(Xing and Liu, 2009)
	Developed model	Trigonometric Ritz method	Exact solutions	
1	4.798	4.806	4.80	
2	5.099	5.102	5.08	
3	5.706	5.704	5.68	
4	6.560	6.573	6.56	
5	7.594	7.612	7.60	
6	7.887	7.895	7.89	

Table 4.16: Frequency parameters  $\lambda = a \sqrt[4]{\rho_p h \omega^2 / D_x}$  for **boron/epoxy CCCC plate**:  $a/b = 0.5$ ,  $E_x = 208$  GPa,  $E_y = 18.9$  GPa,  $G_x = 5.7$  GPa,  $\nu_x = 0.23$ ,  $\kappa = 0.860$ .

Mode	Present dissertation		(Dozio, 2011)	(Xing and Liu, 2009)
	Developed model	Trigonometric Ritz method	Exact solutions	
1	4.738	4.749	4.75	
2	4.818	4.827	4.82	
3	5.002	5.008	5.00	
4	5.323	5.329	5.32	
5	5.796	5.796	5.78	
6	6.381	6.384	6.37	

#### 4.2.2 Plate loaded with additional elements

In this Subsection, a plate with ribs and additional masses mounted on its surface is evaluated. There are no exact solutions for the eigenfrequencies and modeshapes of a finite rectangular plate loaded with such additional elements. Therefore, results of numerical simulations and laboratory experiments are reported.

### Isotropic plate stiffened with ribs

Firstly, a case of an isotropic stiffened plate is considered. It is due to the fact that a number of works in the literature refer to (Olson and Hazell, 1977), where authors presented theoretical and experimental study of the vibrations of integrally machined rib-stiffened plates. Certain structural configurations that they introduced became over the years a benchmark for modelling the stiffened shell structures. Two of these configurations are selected to be used in this dissertation (a general schematic of the plate configuration is shown in Fig. 4.1).

The parameters of the fully-clamped plate and the rib are as follows:

$$a = b = 203 \text{ mm}, \quad h = 1.37 \text{ mm}, \quad E = 68.9 \text{ GPa}, \quad \rho_p = 2670 \text{ kg/m}^3, \quad \nu = 0.3,$$

with a rectangular cross-section of the rib, in case 1a:

$$h_r = 8.28 \text{ mm}, \quad e_r = 4.83 \text{ mm},$$

and in case 1b:

$$h_r = 11.33 \text{ mm}, \quad e_r = 6.35 \text{ mm},$$

where  $h_r$  and  $e_r$  are height and width of the rib, respectively. The rib in both cases is placed in the  $y$  direction, at the centre of the plate.

In (Olson and Hazell, 1977) authors utilized Finite Elements (FE) to calculate natural frequencies and modeshapes of the plate. In (Koko and Olson, 1992) authors used Super Finite Elements (SFE), reducing the number of variables in the mathematical

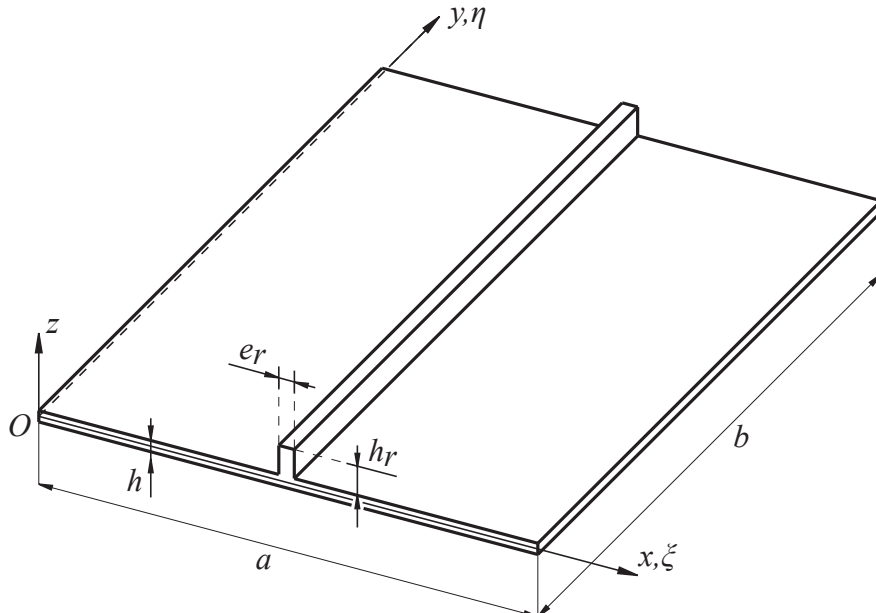


Figure 4.1: Configuration of stiffened plate for comparisons with (Olson and Hazell, 1977), (Koko and Olson, 1992) and (Barrette et al., 2000).

Table 4.17: Natural frequencies for case 1a (Hz).

Mode	Present dissertation			(Barrette et al., 2000)	
	Developed model		ANSYS	HFE	
	Unstiffened	Stiffened	Stiffened	Unstiffened	Stiffened
1	285.2	679.9	679.8	292.8	671.2
2	581.3	714.9	694.8	597.2	744.4
3	581.3	982.6	994.8	597.6	984.6
4	856.8	988.8	1025.4	881.3	1027.2
5	1041.5	1394.6	1459.0	1071.3	1434.4
6	1046.5	1411.1	1441.7	1076.5	1451.9

(Koko and Olson, 1992)					
	SFE	FE (Olson and Hazell, 1977)	Experiment		
Mode	Stiffened				
1	679.1	670.7	627		
2	716.9	724.0	662		
3	990.1	977.2	924		
4	1022.9	1002.1	953		
5	1469.3	1408.7	1370		
6	1442.3	1414.1	1338		

Table 4.18: Natural frequencies for case 1b (Hz).

Mode	Present dissertation			(Barrette et al., 2000)	
	Developed model		ANSYS	HFE	
	Unstiffened	Stiffened	Stiffened	Unstiffened	Stiffened
1	285.2	743.5	746.1	292.8	727.8
2	581.3	752.6	781.4	597.2	783.2
3	581.3	993.8	1035.6	597.6	1015.5
4	856.8	1015.3	1050.6	881.3	1033.8
5	1041.5	1400.7	1466.3	1071.3	1450.0
6	1046.5	1427.4	1470.9	1076.6	1457.9

(Koko and Olson, 1992)					
	SFE	FE (Olson and Hazell, 1977)	Experiment		
Mode	Stiffened				
1	736.8	718.1	689		
2	769.4	751.4	725		
3	1019.6	997.4	961		
4	1032.3	1007.1	986		
5	1483.7	1419.8	1376		
6	1488.3	1424.3	1413		

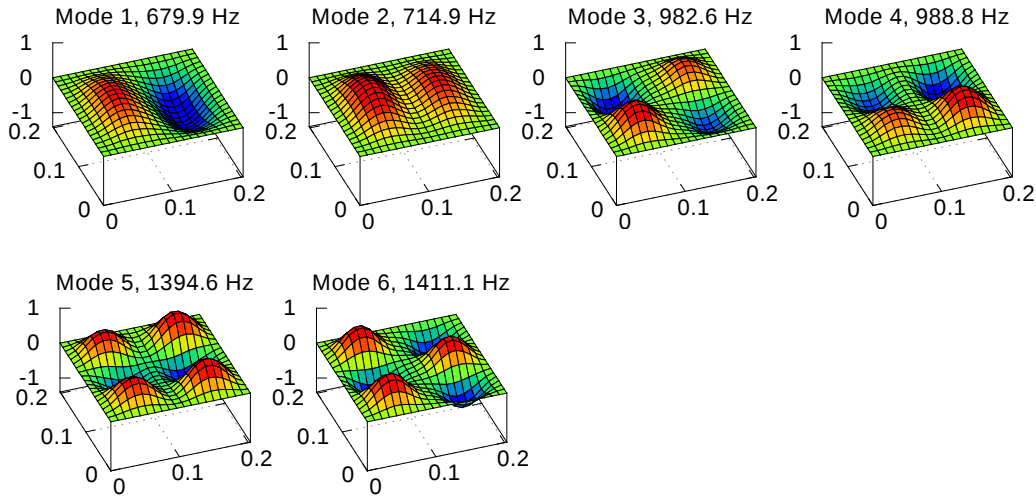


Figure 4.2: The initial 6 eigenmodes shapes and frequencies calculated by the developed model for case 1a (size of the plate is in [m], and the z-axis depicts normalized amplitude).

model, when compared to (Olson and Hazell, 1977). In more recent work (Barrette et al., 2000), authors used the same benchmark and employed Hierarchical Finite Elements (HFE) with a set of local trigonometric interpolation functions. Results obtained by these authors are compared with results calculated according to the model developed in this dissertation. Additionally, calculations performed with ANSYS are also included in the comparison.

Natural frequencies are presented in Tabs. 4.17-4.18 (for a better comparison, an unstiffened plate is also considered). Modeshapes calculated with the developed model are shown in Fig. 4.2.

The coherence of results obtained by the developed mathematical model with the numerical and experimental results reported by references (Koko and Olson, 1992) and (Barrette et al., 2000) is satisfactory, both in terms of eigenfrequencies and modeshapes.

### Isotropic plate loaded with concentrated masses

In this Subsection, the developed model is compared with theoretical and experimental results published in (Stokey and Zorowski, 1959) and (Amabili et al., 2006), where authors studied the effect of concentrated masses with rotary inertia on vibrations of rectangular plates.

In the first comparison, the configuration introduced in (Stokey and Zorowski, 1959) is considered (the case 2a), which was also adopted in (Amabili et al., 2006) for verification. Only the fundamental frequency is evaluated. However, it is done for different types and placement of the additional mass. Parameters of the simply-supported plate used in this comparison are as follows:

$$a = b = 508 \text{ mm}, \quad h = 2.31 \text{ mm}, \quad E = 70.0 \text{ GPa}, \quad \rho_p = 2749 \text{ kg/m}^3, \quad \nu = 0.33.$$

Table 4.19: Fundamental frequencies of the plate with an additional mass, case 2a (Hz).

Mass (kg)	Rotary inertia (kg m <sup>2</sup> )	Position	Present dissertation		
			Developed model		ANSYS
			Unloaded	Loaded	Loaded
0.91	0.0	$\xi_m = 0.50$ $\eta_m = 0.50$	43.4	23.5	23.5
5.40	0.0	$\xi_m = 0.50$ $\eta_m = 0.50$	43.4	10.9	10.9
1.34	0.00237	$\xi_m = 0.25$ $\eta_m = 0.50$	43.4	23.8	23.8
1.34	0.00237	$\xi_m = 0.25$ $\eta_m = 0.25$	43.4	27.6	27.4

Mass (kg)	Rotary inertia (kg m <sup>2</sup> )	Position	(Stokey and Zorowski, 1959)		(Amabili et al., 2006)
			Experiment	Stokey	Amabili
			Loaded	Loaded	Loaded
0.91	0.0	$\xi_m = 0.50$ $\eta_m = 0.50$	23.4	23.5	22.9
5.40	0.0	$\xi_m = 0.50$ $\eta_m = 0.50$	11.0	11.0	10.6
1.34	0.00237	$\xi_m = 0.25$ $\eta_m = 0.50$	26.0	25.1	23.75
1.34	0.00237	$\xi_m = 0.25$ $\eta_m = 0.25$	28.5	28.7	27.3

Parameters of the additional mass and obtained fundamental frequencies for different configurations are given in Tab. 4.19.

In the second comparison (case 2b), the present model is evaluated for the configuration analysed theoretically and experimentally in (Amabili et al., 2006). Similarly to the previous case, only one additional mass is considered, however, initial 7 eigenmodes are analysed. Moreover, plate edges elastically restrained against rotation are adopted with  $k_{rx0} = k_{rx1} = k_{ry0} = k_{ry1} = 4.5 \text{ N/rad}$ . The parameters of the plate used in this comparison are as follows:

$$a = 210.0 \text{ mm}, \quad b = 208.5 \text{ mm}, \quad h = 0.3 \text{ mm}, \quad E = 198 \text{ GPa}, \quad \rho_p = 7850 \text{ kg/m}^3, \quad \nu = 0.3.$$

An additional mass of 0.0112 kg with the moment of inertia  $I_{mx} = I_{my} = 0.205 \cdot 10^{-5} \text{ kg m}^2$  has been placed at  $\xi_m = 0.25$  and  $\eta_m = 0.25$ . Natural frequencies for this configuration are presented in Tab. 4.20, and eigenmodes shapes calculated by the developed model are shown in Fig. 4.3.

The results obtained by the present model are consistent with theoretical and experimental results reported in cited papers, both regarding the natural frequencies and modeshapes.

Table 4.20: Natural frequencies for case 2b (Hz).

Mode	Present dissertation		(Amabili et al., 2006)			
	Developed model		Amabili		Experiment	
	Unloaded	Loaded	Unloaded	Loaded	Unloaded	Loaded
1	38.0	35.7	38	36.0	38.1	36.0
2	84.9	70.4	87.1	70.6	81.1	69.7
3	90.3	87.3	88.0	87.0	91.4	88.4
4	137.0	118.3	137	118	136	114
5	166.3	152.3	169	156	165	148
6	173.4	156.5	171	157	168	154
7	217.6	183.0	218	188	212	173

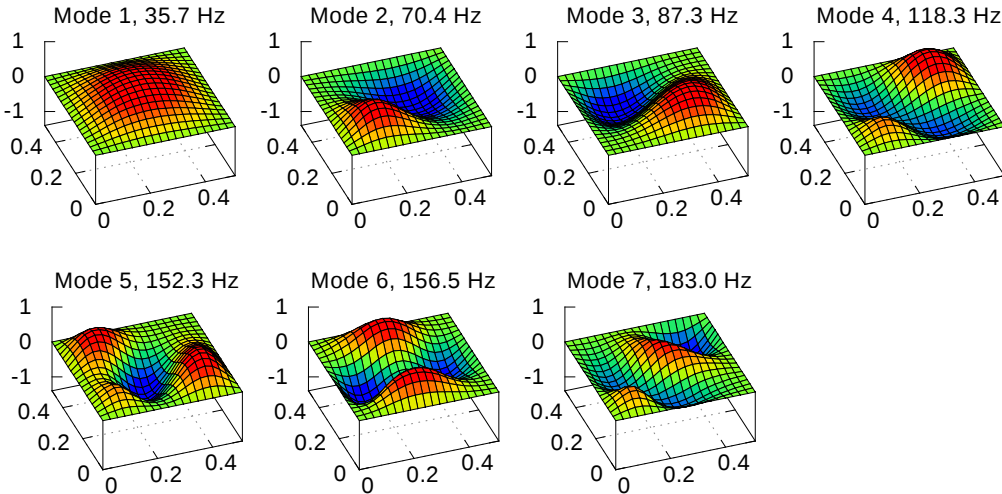


Figure 4.3: The initial 7 eigenmodes shapes and frequencies calculated by developed model for case 2b (size of the plate is in [m], and the z-axis depicts normalized amplitude).

The comparisons presented in this Section confirm the versatility and accuracy of the developed model for modelling of individual plates.

### 4.3 Comparison for active casing walls

In this Section, the developed model is evaluated for active casing walls, which are considered separately, but constitute a part of the three-dimensional structure. The experimental measurements performed by the author are used. Firstly, several configurations utilizing the rigid casing are evaluated. Then, suitability and accuracy of the developed model for light-weight casing walls are investigated.

### 4.3.1 Rigid casing walls

In this Subsection, the measurements and simulation results are presented, obtained for various configurations of rigid casing wall. The experiments were performed utilizing a laboratory setup shown in Fig. 4.4. In all performed experiments, single wall has been acoustically excited with a random wideband signal. The response of the plate has been measured in 400 uniformly distributed points (the distance between adjacent points was equal 20 mm). Remaining walls have been either removed or passively insulated to minimize the interference at this stage of the research.

#### Unloaded casing wall

Firstly, an unloaded casing wall is evaluated. It is a 1 mm thick brushed aluminium plate. Due to the manufacturing process, the plate represents orthotropic properties—it follows from the analysis of initial 11 eigenmodes presented in Fig. 4.5 that despite square shape of the plate, e.g. 2nd and 3rd natural frequencies are not equal. Depending on the application, the wall could be satisfactorily approximated with an isotropic plate model. However, to obtain the highest modelling accuracy, the orthotropic Mindlin plate model is used. The parameters of the plate used for the purpose



Figure 4.4: The laboratory setup with the laser vibrometer and the rigid casing used to measure modeshapes of the casing walls.

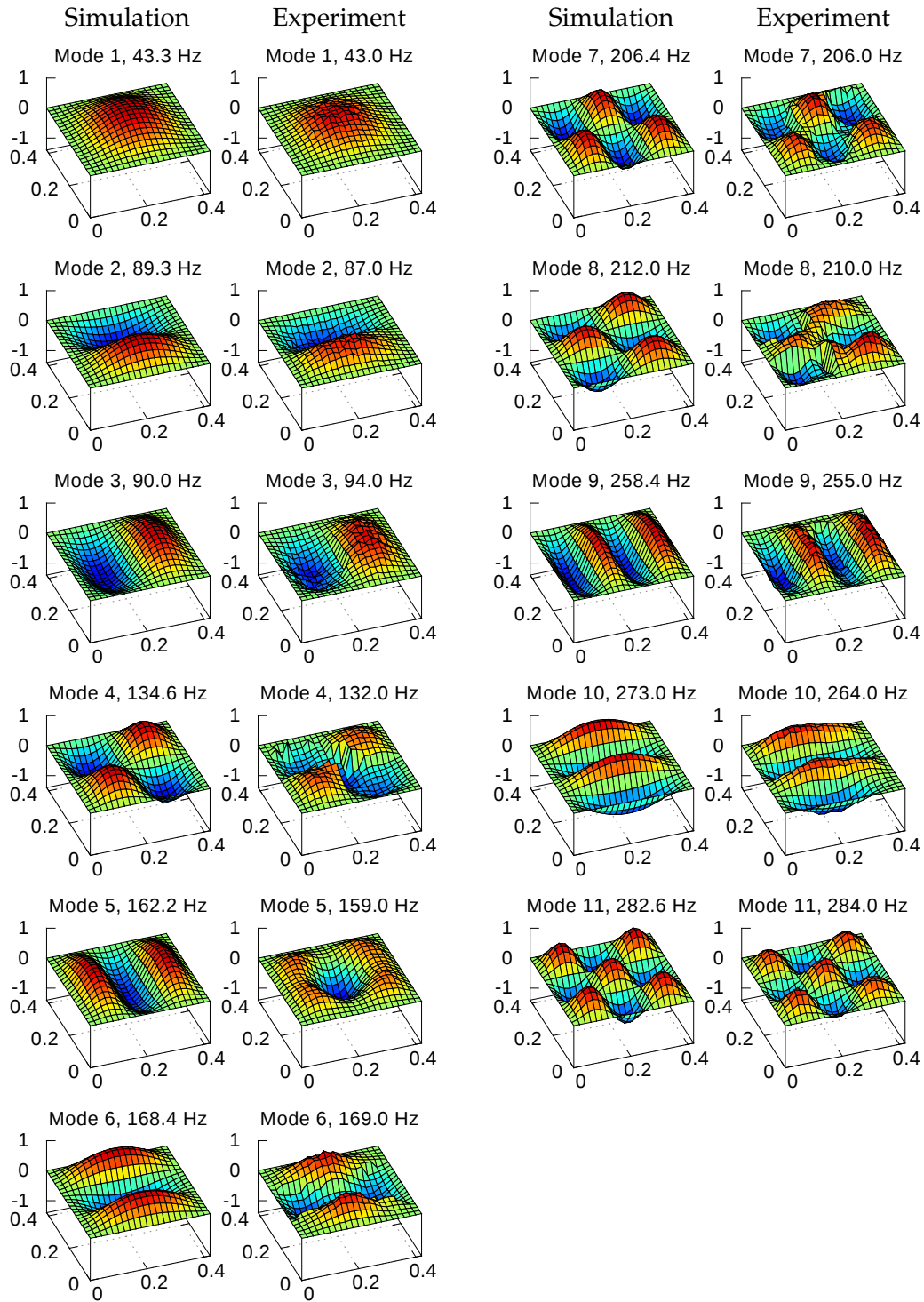


Figure 4.5: A comparison of initial 11 natural frequencies and modeshapes of rigid casing wall, calculated with the mathematical model and experimentally measured—1 mm thick aluminium unloaded plate.

of modelling are as follows:

$$\begin{aligned} a &= 0.420 \text{ m}, & b &= 0.420 \text{ m}, & h &= 0.001 \text{ m}, \\ E_x &= 91.2 \text{ GPa}, & E_y &= 60.8 \text{ GPa}, & G_{xy} &= 29.2 \text{ GPa}, \\ \rho_p &= 2770 \text{ kg/m}^3, & \nu_x &= 0.3, & \kappa_x &= 5/6. \end{aligned}$$

For the rigid casing walls, fully-clamped boundary conditions offer generally satisfactory results. However, in this case, boundary conditions elastically restrained against rotation are used. The stiffness coefficients of rotational springs have been assumed close to completely rigid (as it is for fully-clamped boundary conditions), but a minor softening of the springs offered better fitness to the real measurement data.

Assessing the fitness of theoretically calculated natural frequencies and modeshapes to the real measurements of rigid casing wall (see Fig. 4.5), it can be considered as entirely sufficient. Therefore, a model evaluated in such way for the unloaded plate can now be used to investigate behaviour of the plate when the additional elements are attached to its surface.

### Casing wall with additional mass

The next case is an evaluation of the casing wall with an additional mass attached. In this investigation, a mass of  $m_{m,1} = 0.080 \text{ kg}$  is used. It is rigidly bonded to the plate surface at location  $x_{m,1} = 0.340 \text{ m}$  and  $y_{m,1} = 0.340 \text{ m}$ . Measurements were performed in the same manner as for the unloaded plate. Rotary inertia of the attached mass is taken into account. Theoretically calculated and experimentally measured natural frequencies and modeshapes are compared in Fig. 4.6. A high consistency of both results is obtained.

### Casing wall with inertial actuators

In this investigation, the inertial excitors EX1 are considered. Their weight (0.115 kg) is often comparable with the weight of the wall itself, hence they are significantly affecting its dynamical behaviour when mounted. To correctly determine their efficient locations for the purpose of active control, this effect have to be accordingly taken into account in the mathematical modelling. The correctness of this aspect of the model is now validated. Firstly, a single actuator is mounted to the plate surface at location  $x_{a,1} = 0.340 \text{ m}$  and  $y_{a,1} = 0.340 \text{ m}$  (the same as the previously tested additional mass). Rotary inertia of the inertial exciter is also taken into account. Theoretically calculated and experimentally measured natural frequencies and modeshapes are compared in Fig. 4.7. Similarly as in case of an additional mass, a high accuracy of theoretical predictions is shown.

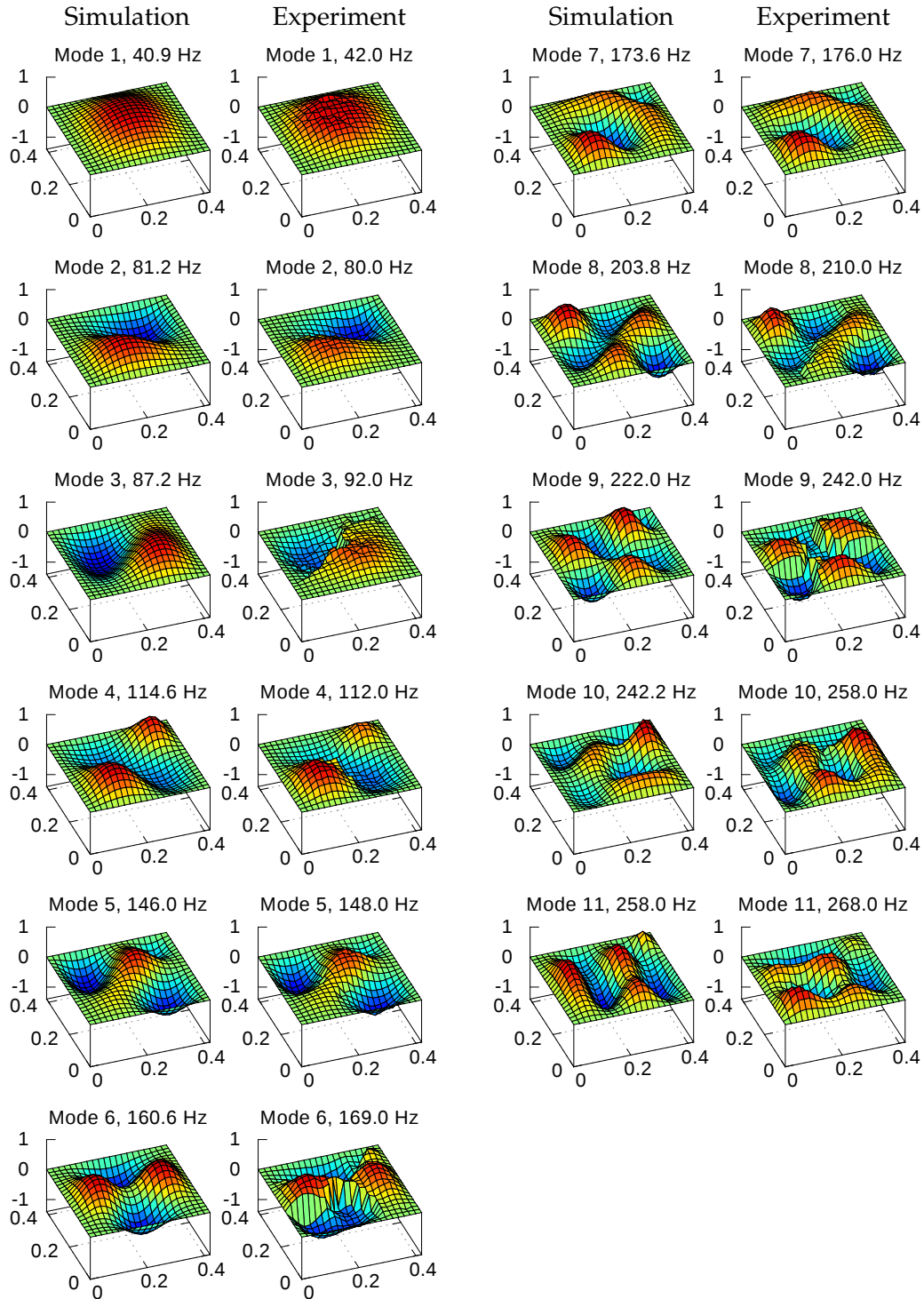


Figure 4.6: A comparison of initial 11 natural frequencies and modeshapes of rigid casing wall, calculated with the mathematical model and experimentally measured—1 mm thick aluminium plate with an additional mass of  $m_{m,1} = 0.080 \text{ kg}$  mounted at  $x_{m,1} = 0.340 \text{ m}$  and  $y_{m,1} = 0.340 \text{ m}$ .

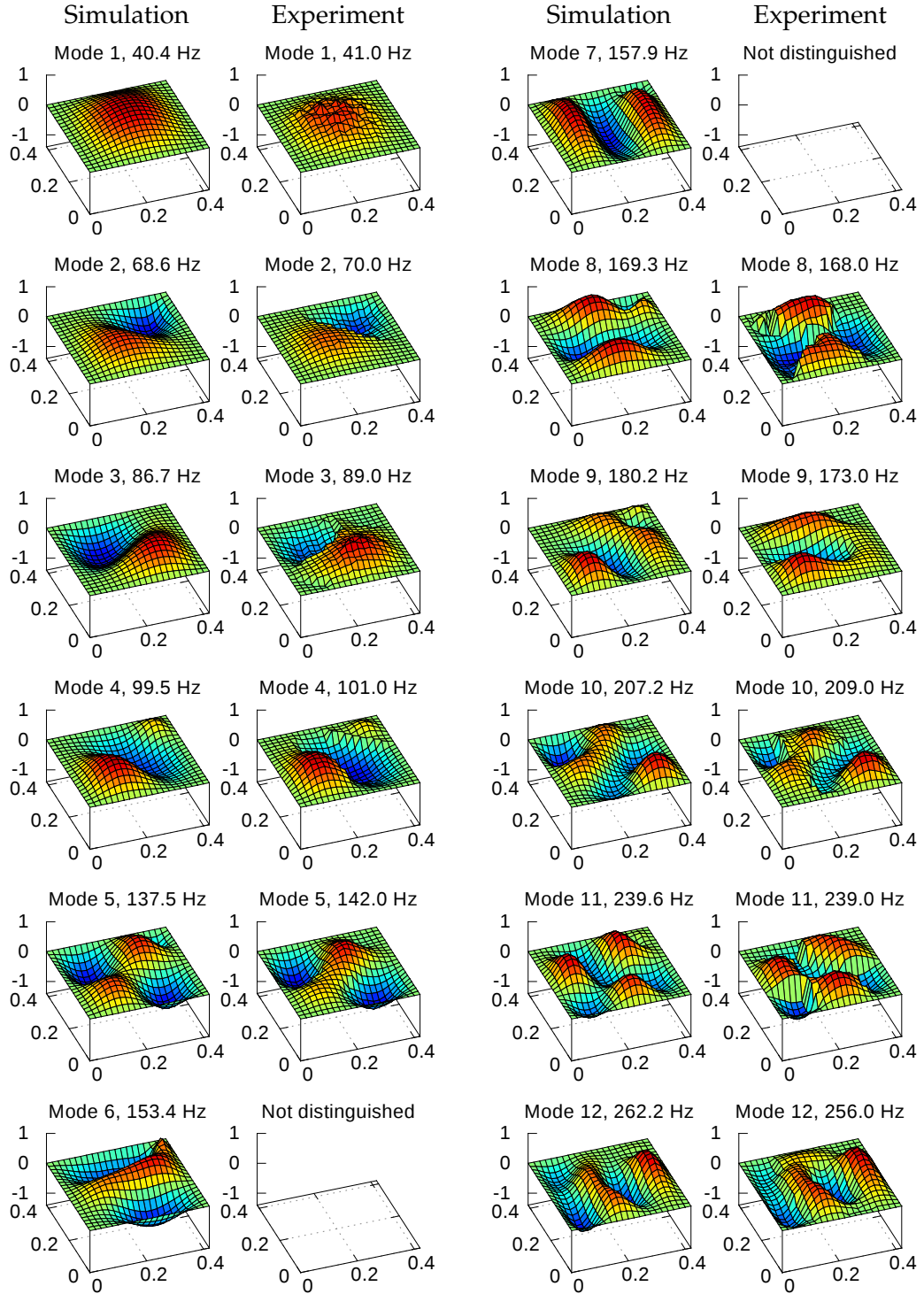


Figure 4.7: A comparison of initial 12 natural frequencies and modeshapes of rigid casing wall, calculated with the mathematical model and experimentally measured—1 mm thick aluminium plate with an inertial actuator EX1 of mass  $m_{a,1} = 0.115$  kg mounted at  $x_{a,1} = 0.340$  m and  $y_{a,1} = 0.340$  m.

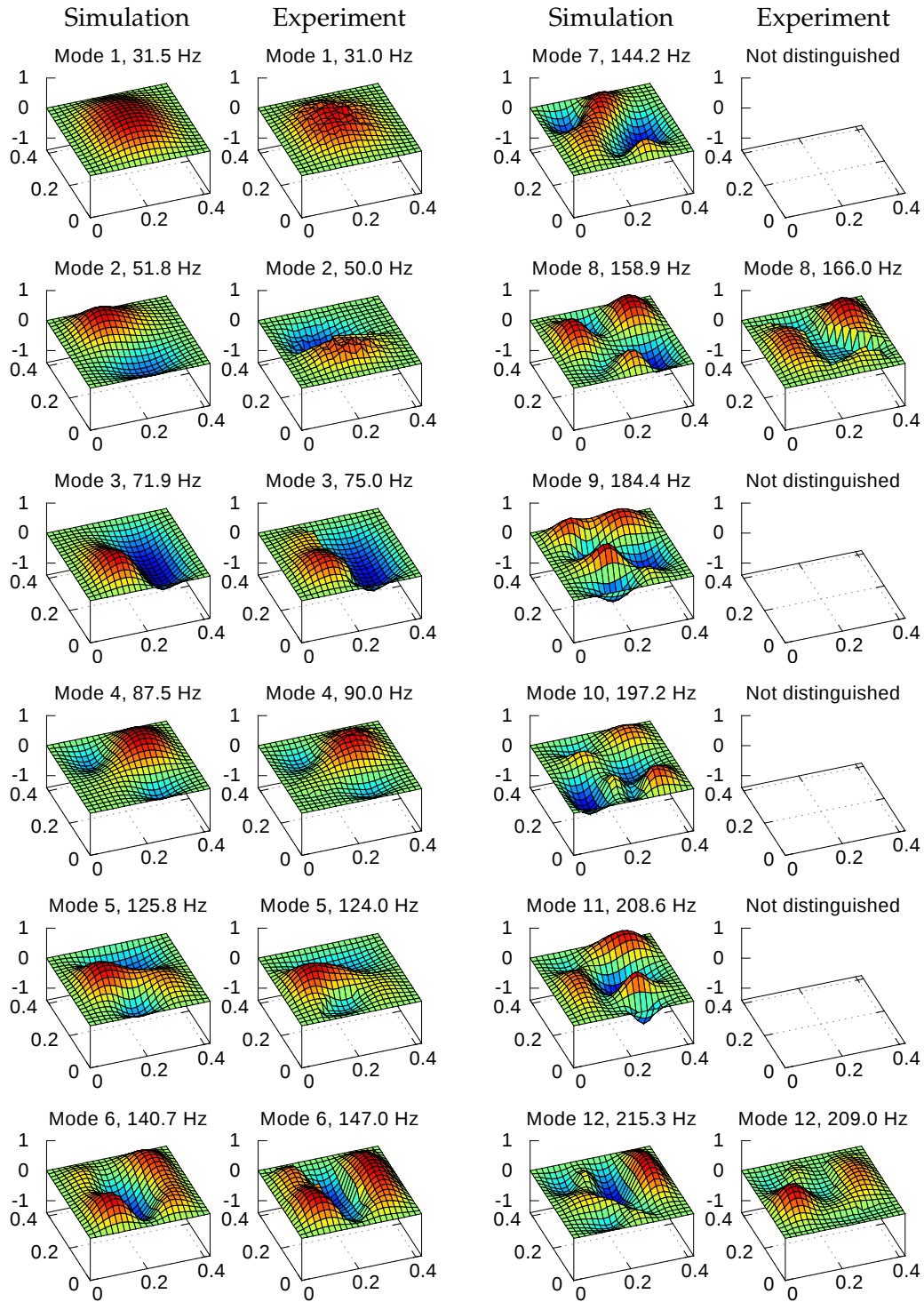


Figure 4.8: A comparison of initial 12 natural frequencies and modeshapes of rigid casing wall, calculated with the mathematical model and experimentally measured—1 mm thick aluminium plate with three inertial actuators EX1 mounted to the surface.

Secondly, three actuators are mounted to the plate surface at locations:

$$\begin{aligned}x_{a,1} &= 0.260 \text{ m}, & y_{a,1} &= 0.072 \text{ m}, \\x_{a,2} &= 0.171 \text{ m}, & y_{a,2} &= 0.110 \text{ m}, \\x_{a,3} &= 0.135 \text{ m}, & y_{a,3} &= 0.312 \text{ m}.\end{aligned}$$

The arrangement is a result of optimization process described in Subsection 5.4.3. Theoretically calculated and experimentally measured natural frequencies and modeshapes of the plate are compared in Fig. 4.8. In the considered case, theoretical and experimental results are also satisfactorily consistent.

### Casing wall with ribs and additional masses

In the last scenario evaluated for the rigid casing, a configuration with ribs and additional masses is studied. The arrangement is obtained by the frequency response shaping method. The considered goal is to move natural frequencies of the plate away from given frequency of 175 Hz, as far as possible, by mounting additional elements in an appropriate arrangement. Details of the optimization procedure itself are given in Subsection 5.4.5. What is studied here, is the natural frequencies and modeshapes of the unloaded plate, their modification after mounting the elements, and the consistency of measurements with theoretical calculations.

Firstly, the unloaded 1 mm thick steel plate is evaluated. Similarly as in case of aluminium plate, the steel plate represents some orthotropic properties. However, in this case an isotropic plate model is used to approximate the casing wall. The parameters of the plate used for the purpose of modelling are as follows:

$$\begin{aligned}a &= 0.420 \text{ m}, & b &= 0.420 \text{ m}, & h &= 0.001 \text{ m}, \\E &= 200 \text{ GPa}, & G &= 76.9 \text{ GPa}, \\&\rho_p = 7850 \text{ kg/m}^3, & \nu &= 0.3, & \kappa &= 5/6.\end{aligned}$$

Boundary conditions are assumed to be fully-clamped.

Assessing the accuracy of theoretically calculated natural frequencies and modeshapes in comparison to the real measurements of steel casing wall (see Fig. 4.9), it can be considered as satisfying. Therefore, the next step is to evaluate the plate with the additional elements attached to its surface. A comparison of theoretically calculated and experimentally measured natural frequencies and modeshapes are given in Fig. 4.10. The laboratory setup prepared for this purpose is shown in Fig. 4.11. The mass and the first rib are bonded to the outer surface of the plate, whereas the second rib is bonded for technological simplicity to the inner side. In a professionally assembled casing, all these elements could obviously be bonded to the same side. Similarly as for the unloaded case, a high consistency of the results is observed.

In addition, experimentally measured frequency responses of the unloaded and loaded plate are given in Fig. 4.12. It is obtained by averaging frequency responses in

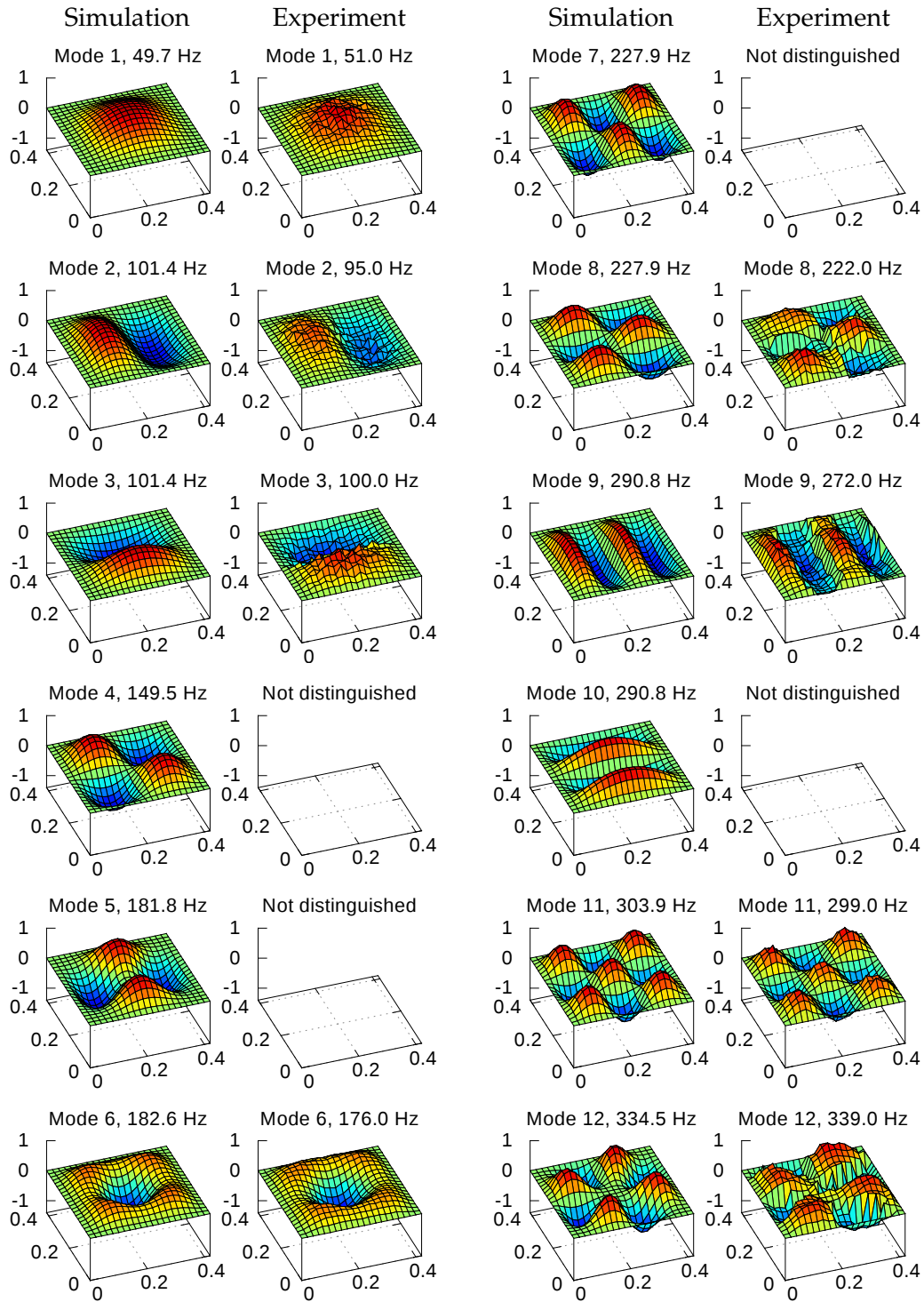


Figure 4.9: A comparison of initial 12 natural frequencies and modeshapes of rigid casing wall, calculated with the mathematical model and experimentally measured—1 mm thick steel unloaded plate.

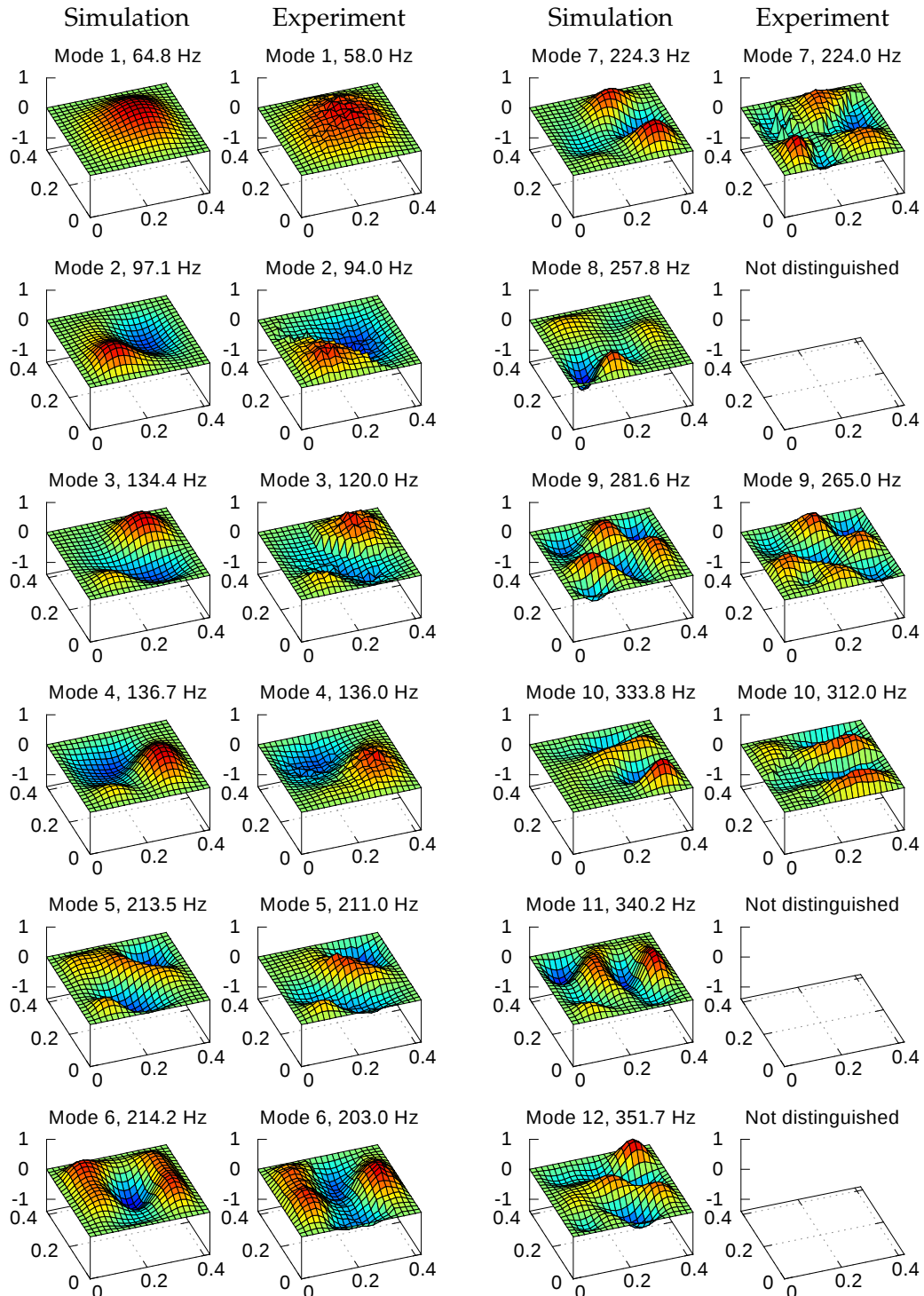


Figure 4.10: A comparison of initial 12 natural frequencies and modeshapes of rigid casing wall, calculated with the mathematical model and experimentally measured—1 mm thick steel plate with ribs and additional masses mounted to the surface.

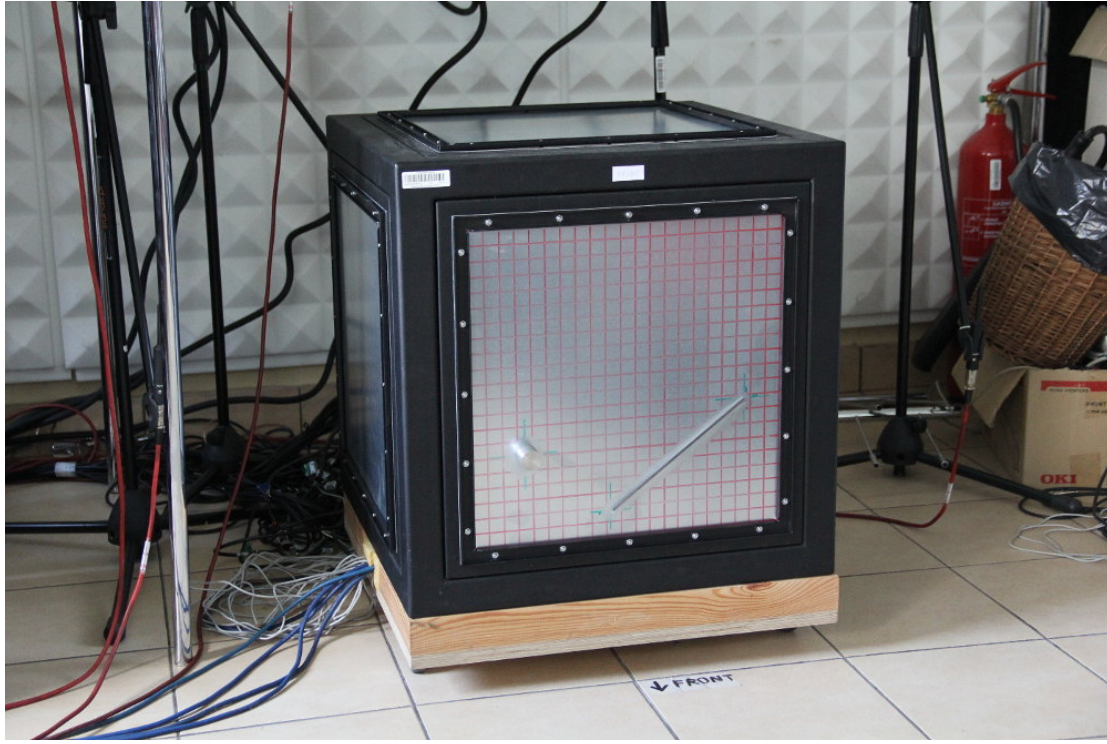


Figure 4.11: The laboratory setup with the rigid casing to measure natural frequencies and modeshapes of the casing walls with ribs and additional mass mounted to the plate surface.

all measurement points distributed uniformly over the plate surface. It follows from the analysis of the response that the given goal is satisfactorily achieved. The valley created in the proximity of frequency of 175 Hz is slightly moved to lower frequencies than in the theoretical calculations. However, still a significant margin to the nearest eigenmode of 203 Hz has been preserved, resulting in a good enhancement of noise and vibration isolation around the assumed frequency. Minor differences between measurements and calculations can be explained by imperfect bonding of the additional elements to the plate surface with a market available glue. Obviously, the precision of

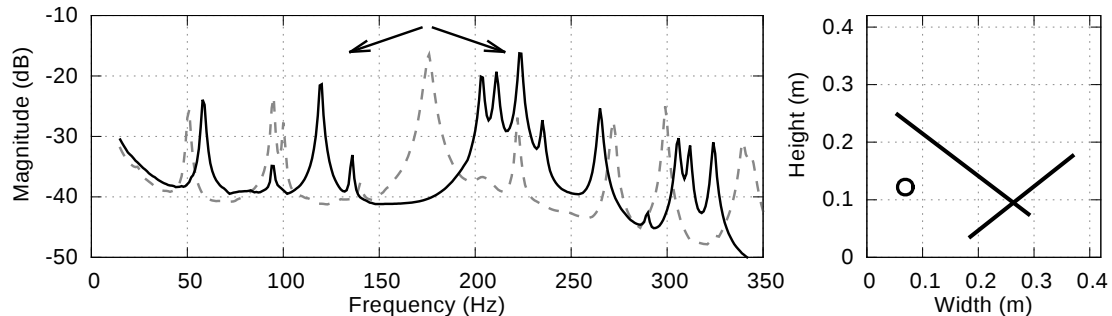


Figure 4.12: Experimentally measured frequency response of the plate (solid line—loaded plate; dashed line—unloaded plate) and visualization of additional elements mounted on the plate (circle—a mass; lines—ribs).

material parameters needed for modelling had also an impact. However, this experiment validates the suitability of the employed frequency response shaping method, described in Subsection 5.4.5.

### 4.3.2 Light-weight casing walls

In this subsection, the light-weight casing is under consideration. A variant of dimensions 500 mm × 630 mm × 800 mm with 1.5 mm of plate thickness is used. The casing with accompanying laboratory setup is shown in Fig. 4.13. During the measurements of the natural frequencies and modeshapes, the whole casing was excited together with a random signal by a loudspeaker placed inside. The response of the casing was measured in uniformly distributed points with the distance between the adjacent points equal 20 mm (as in the case of the rigid casing walls). Such dense grid resulted in many measurement points: 1280 points for the top wall, 1000 points for the front wall and 800 points for the left wall. Hence, a high accuracy of the measured modeshapes is obtained. They can be presented for the whole casing together, as in an example for frequency of 155 Hz given in Fig. 4.14. However, as it was discussed in previous Chapters, the light-weight casing constitutes a three-dimensional structure with strong



Figure 4.13: The laboratory setup with the laser vibrometer and the light-weight casing to measure modeshapes of the structure.

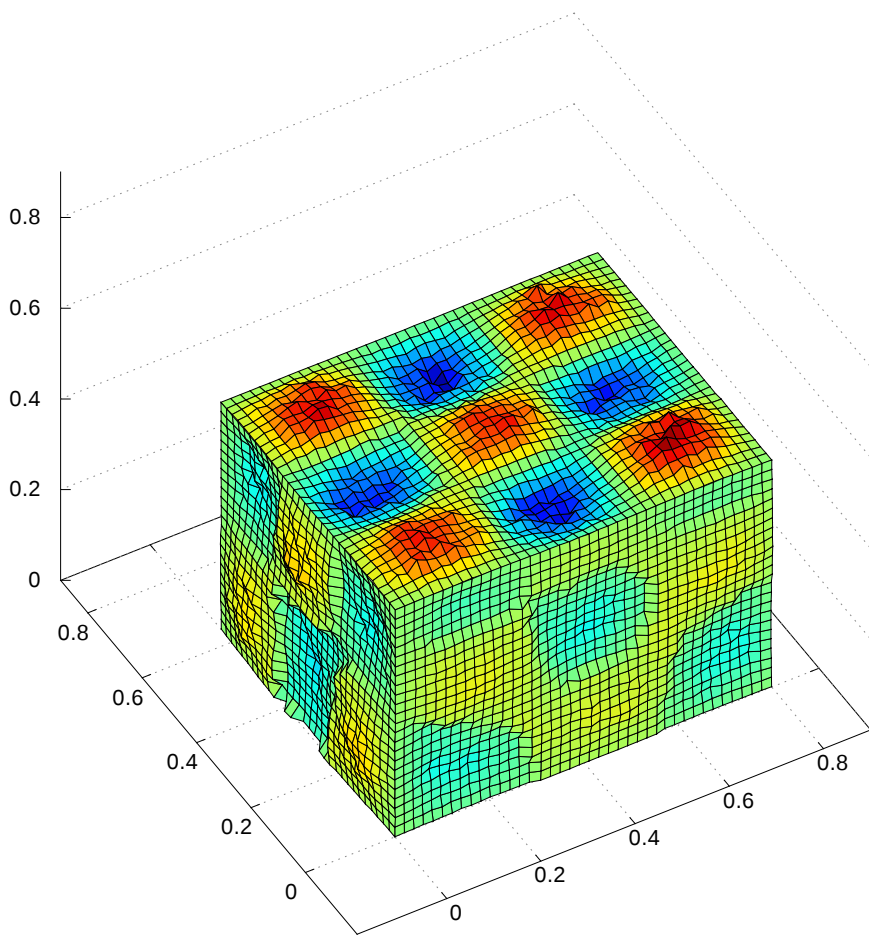


Figure 4.14: Three-dimensional visualization of experimentally measured modeshape of the whole light-weight casing, for an exemplary frequency of 155 Hz. All dimensions are given in [m].

couplings, but due to its specific dynamical behaviour, it can be studied with each of its walls separately. Therefore, due to methodology of the modelling, theoretical calculations and measurements are further compared for each wall separately (right and back walls are omitted as they are symmetrical to the left and front walls, respectively).

The mathematical modelling of the loading of the casing walls with additional elements is validated in previous Subsections. Therefore, to justify the application of the developed model for the light-weight casing, only results for the unloaded casing are presented.

### Unloaded casing walls

Mathematical model parameters used here can be divided into two groups. First group includes dimensions and material properties of the plates that are known, and in this research they are represented by following values:

$$\begin{aligned} h &= 0.0015 \text{ m}, \\ E &= 200 \text{ GPa}, \quad G = 76.9 \text{ GPa}, \\ \rho_p &= 7850 \text{ kg/m}^3, \quad \nu = 0.3, \quad \kappa = 5/6. \end{aligned}$$

All of these values are common for all walls of the casing. The width and height of each plate (denoted by  $a$  and  $b$ , respectively) are defined by corresponding dimensions of the casing given earlier in the Subsection.

The second group consists of parameters, which cannot be measured or calculated directly. Therefore, for the purpose of fitting the model to the behaviour of real whole vibrating structure, an optimization algorithm is used to identify them. In this research, such parameters are spring constants describing boundary conditions of each wall. Plate edges are assumed to be elastically restrained against both rotation and translation, hence there are four rotational spring constants  $k_{rx0}$ ,  $k_{rx1}$ ,  $k_{ry0}$ ,  $k_{ry1}$ , and four translational spring constants  $k_{tx0}$ ,  $k_{tx1}$ ,  $k_{ty0}$ ,  $k_{ty1}$ , defined as in Section 3.3, to be identified for each casing wall (as the two pairs of walls are symmetrical—left and right, front and back—the same configuration is calculated for a given pair). The obtained results and process of identification procedure is described in more details in Section 5.3 and in (Wrona and Pawelczyk, 2016c). What is important, four natural frequencies and modeshapes of each wall were selected in the optimization process for the model to fit to (in following figures they are marked with a red arrow).

A comparison of initial 12 eigenmodes (simulated for optimal set of spring constants and measured experimentally) of the top, front and left wall are given in Figs. 4.15–4.17, respectively. It was expected that frequencies of eigenmodes selected for the optimization would be consistent (they are marked with a red arrow). However, remaining eigenmodes that were observed, but were not used in the identification process, are also consistent with the model, confirming the correctness of the proposed procedure of identification.

Summarizing the results obtained and presented in Figs. 4.15–4.17, the coherence of the developed model and real behaviour of the light-weight casing walls is confirmed.

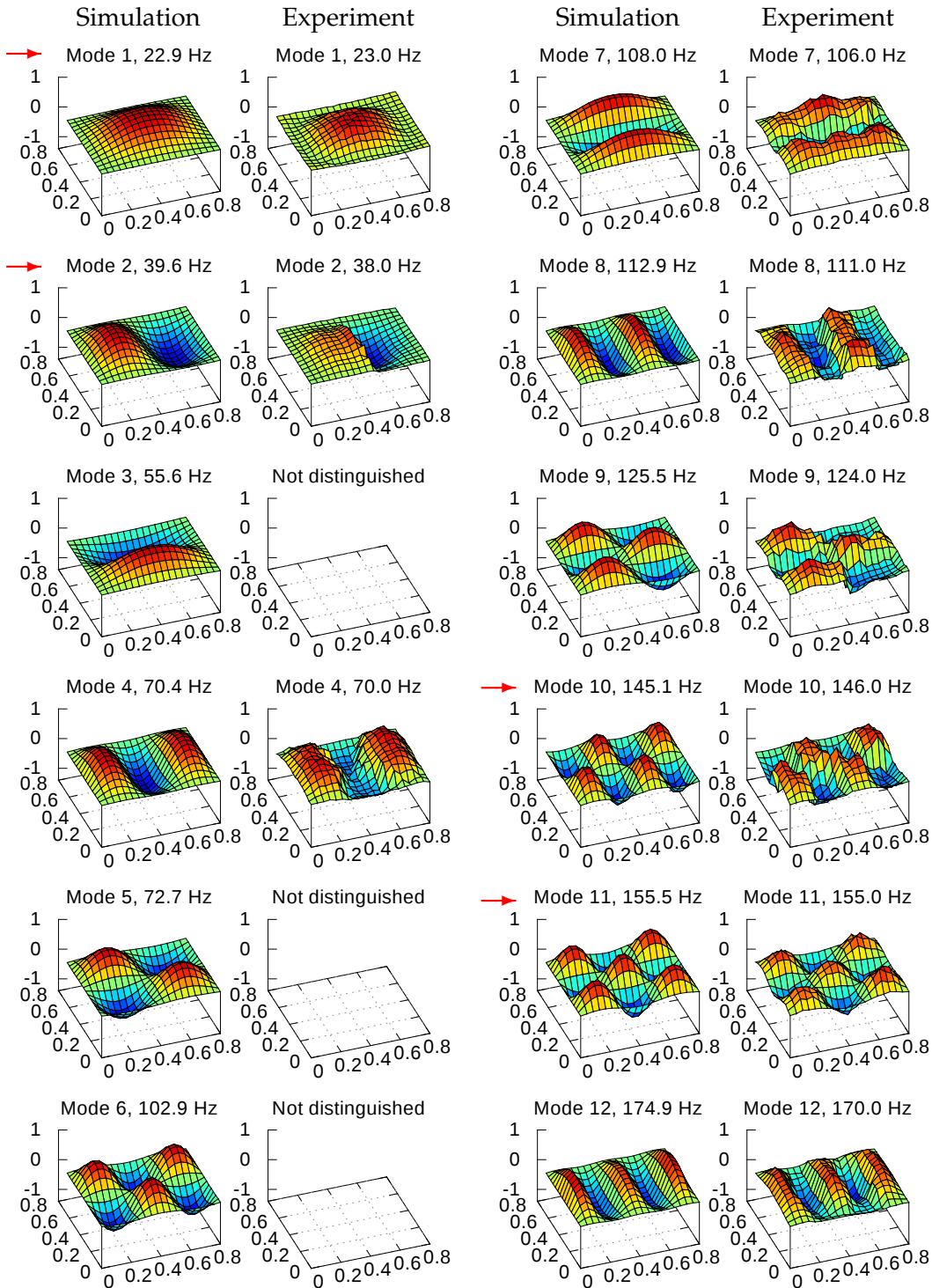


Figure 4.15: A comparison of initial 12 natural frequencies and modeshapes of the top wall of the light-weight casing, calculated with the mathematical model and experimentally measured. The red arrow marks well recognized modes selected for model fitting.

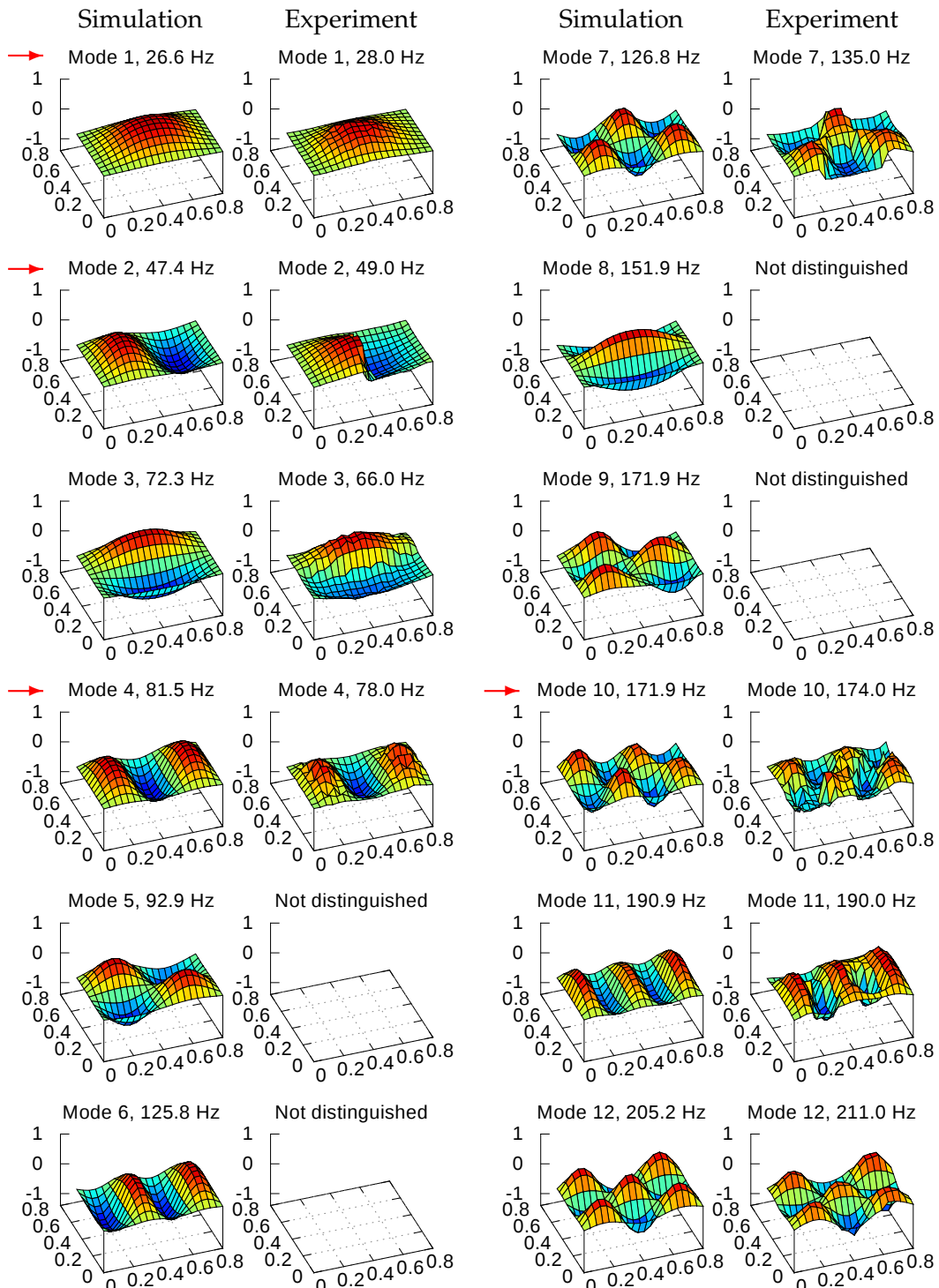


Figure 4.16: A comparison of initial 12 natural frequencies and modeshapes of the front wall of the light-weight casing, calculated with the mathematical model and experimentally measured. The red arrow marks well recognized modes selected for model fitting.

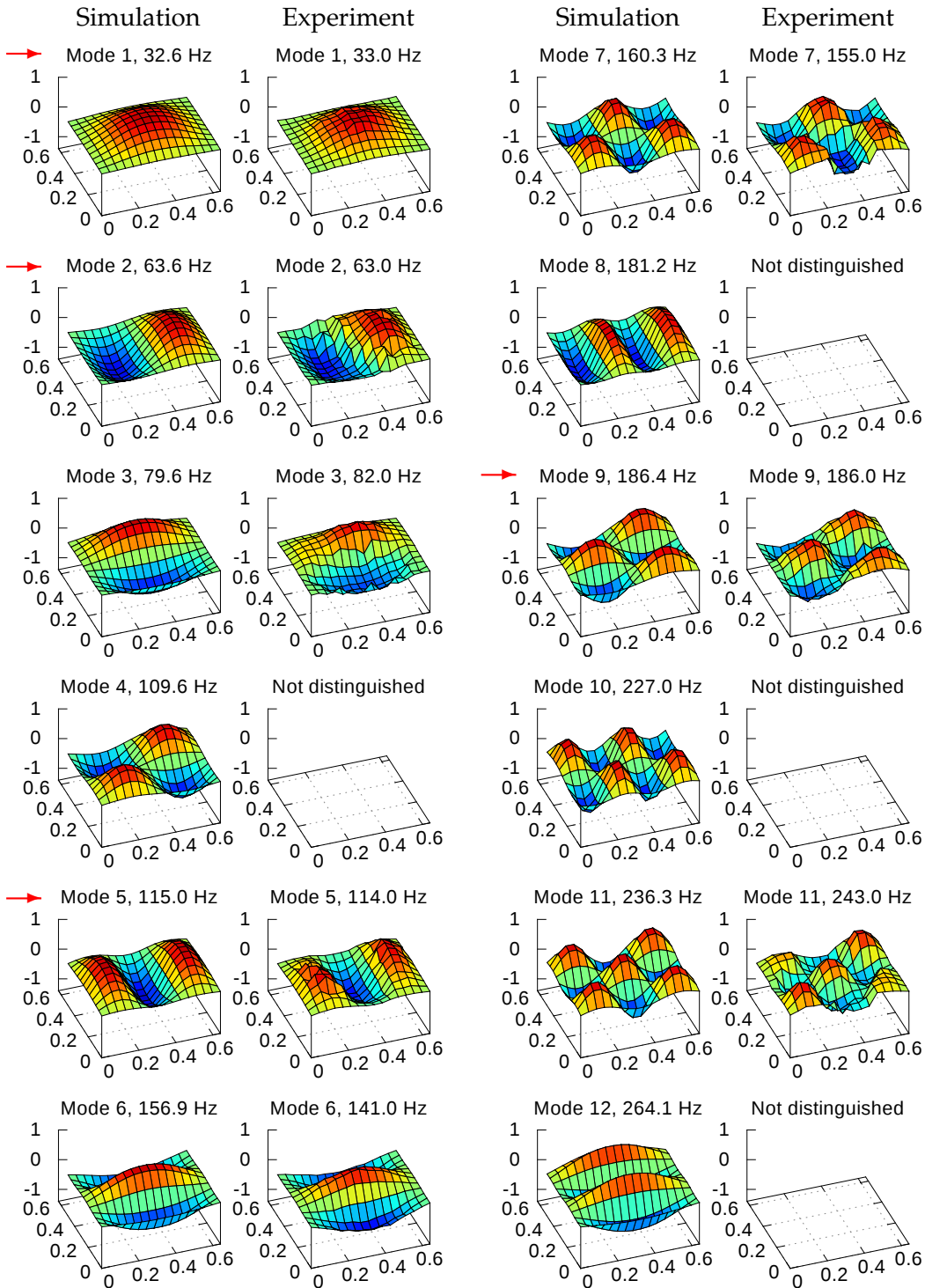


Figure 4.17: A comparison of initial 12 natural frequencies and modeshapes of the left wall of the light-weight casing, calculated with the mathematical model and experimentally measured. The red arrow marks well recognized modes selected for model fitting.

## 4.4 Summary

In this Chapter, the developed model of a casing wall has been validated by means of a comparison with the benchmarks known from literature and laboratory experiments performed by the author. The comparison includes natural frequencies, modeshapes and frequency response functions. Among multiple results of simulation and experiments, the laboratory measurement procedure has been also described.

The model provides satisfactory results for all considered examples. For some applications, even simple isotropic plate model with classical boundary conditions provided results consistent with a real plant. However, to obtain highest modelling accuracy for real structures, often orthotropic plate model with elastically restrained boundary conditions should be used.

It is also noteworthy that the model accurately predicts the impact on frequency responses of additional elements mounted to the plate surface (for both additional masses and ribs). Hence, it can be considered as validated and it can be now employed for the optimization procedures described in the following Chapter.



# Chapter 5

## Optimization process

### 5.1 Background

The response of a physical object excited to vibrations is determined by its mechanical structure. Even slight modifications of the structure may strongly affect its frequency characteristics. On the other hand, the performance of an active noise/vibration control system is highly dependant on both the plant structure itself and an arrangement of actuators and sensors applied to it. Therefore, the active control of an object like the considered device casing should be preceded by thorough investigation of its mechanical structure. Firstly, it is to maximize the susceptibility of the plant to the active control by plausible modifications (e.g. by mounting some additional passive elements on the casing walls to appropriately shape the frequency response). Secondly, it is to efficiently apply actuators and sensors, so the maximum advantage could be taken of them (e.g. by maximizing measures of controllability and observability of the obtained system).

Sometimes an intuition, expert knowledge, or simply trial and error method can be used to improve the properties of a vibrating structure and/or its active control system. But it is rather limited for simplest cases. Any more complicated scenario generally would require more sophisticated method to obtain expected results. One of the approaches is to apply an optimization algorithm. To employ it, firstly, a form of theoretical model of the investigated structure have to be constructed and validated. Then, the objectives and constraints need to be defined in an appropriate form. Finally, an optimization algorithm is chosen and launched utilizing the aforementioned elements. The quality of obtained results depends both on the accuracy of modelling and the effectiveness of employed optimization algorithm.

In the following considerations, the mathematical model of a casing wall is used (developed and validated in previous Chapters). Different scenarios are evaluated and various objectives are considered, including both passive and active applications. The memetic algorithm is used to optimize the given structure according to defined cost functions. It is generally assumed in all evaluated cases that a particular structure is already available and it can be modified by adding some elements to the system, rather than to be modified at a level of a redesign (although, presented approach could be also applied for such considerations). Moreover, any actions undertaken should not

interfere with the device regular operations (should not affect noticeably any device parameters, including heat transfer, dimensions or total mass).

In the beginning of this Chapter, a memetic algorithm is introduced and described in Section 5.2. In Section 5.3, the optimization algorithm is used to identify the model boundary conditions for the light-weight casing walls. Then, in Section 5.4, the memetic algorithm is employed for structure optimization. Initially, an optimization of actuators and sensors arrangement for the rigid casing is considered. Subsequently, the same problem for the light-weight casing is investigated. Afterwards the frequency response shaping method is presented, which is suitable both for passive and active control applications.

## 5.2 Memetic algorithm

The search spaces followed from the problems discussed in this Chapter are very complicated. An efficient algorithm should be chosen to find a solution satisfying defined demands. Evolutionary Algorithms (EA) have proven to be a versatile and effective technique for solving nonlinear optimization problems with multiple optima (Goldberg et al., 1989). However, they usually require evaluation of numerous solutions resulting in high computational cost. To mitigate this drawback, a Memetic Algorithm (MA) can be utilised, which is a hybrid form of population-based approach coupled with separate individual learning. The MA combines advantages of a global search, like for EA, and local refinement procedures, which enhance converge to the local optima (Neri et al., 2012). Because of complementary properties, they are particularly useful in solving complex multi-parameter optimization problems, such as placement of additional elements on a vibrating plate (Wrona and Pawelczyk, 2013b,a).

The memetic algorithm flowchart is presented in Fig. 5.1. It starts with a randomly generated population. The fitness function is evaluated for each individual in the population. A part of the existing population is selected for further reproduction dependent on the fitness value (individuals fitting better are more likely to be chosen). Children solutions are generated by applying a crossover operator for two or more parents. To maintain genetic diversity, the mutation operator is used dependent on a predefined

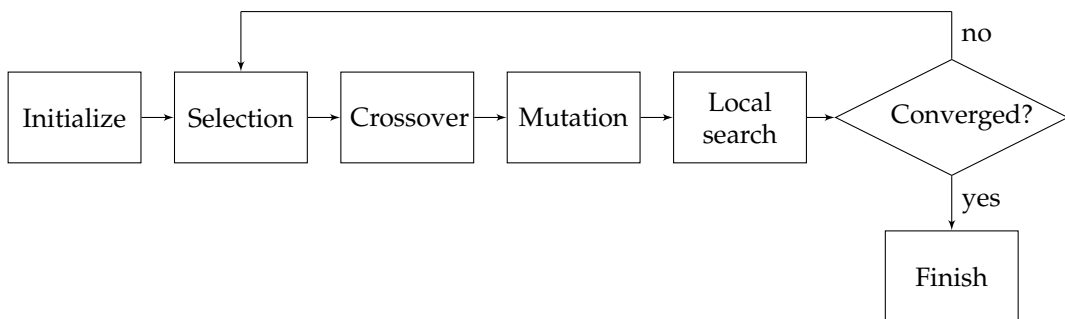


Figure 5.1: A memetic algorithm flowchart.

probability. Then, a local search operator is employed to improve individual fitness. To maintain a balance between the degree of evolution (exploration) and individual improvement (exploitation), only a portion of the population individuals undergo the learning. Afterwards, a selection is performed, and the process is repeated until a certain termination criterion is met.

The size of the population is kept the same in each iteration step. Best individuals are kept unchanged in the next generation (elitist selection). The "Hill climbing" technique (Neri et al., 2012), is chosen as the individual learning strategy. The termination criterion is satisfied if no improvement is found in a number of following iterations, or if the maximum number of iterations is reached.

### 5.2.1 Comparison of evolutionary and memetic algorithms

In this Subsection, to justify the employment of the MA, performance test of evolutionary and memetic algorithms in application to the problem of actuators placement is presented. The rigid casing is taken as an example for the purpose of the comparison (details of the problem specific parameters are described in the Subsection 5.4.3). Due to built-in local search procedures, the MA involves more operations than EA in each generation. An extend of the additional computational load depends on adopted parameters and chosen procedures. For the study to be adequate, both algorithms should possess the same computational budget. Therefore, during the test, population in EA consisted of 90 individuals, while MA population had only 20 individuals. Such arrangement resulted in similar average computation time. Maximum number of generations was set to 30.

Both algorithms were started with randomly generated initial population, which affects strongly convergence rate. To obtain statistical measures of their performance, each algorithm was run 100 times. Each particular run is presented in gray in Fig. 5.2, for distribution of possible results to be visible. The average result is shown as the bold black line.

It follows from the analysis of characteristic values (see Tab. 5.1) that both algorithms are capable of reaching similar level of best value of the fitness function. However, EA best solution is worse than MA average solution. This indicates that both of them could be used successfully in solving the optimization problem, but MA provides better solution. To ensure that obtained solution is near the global optimum, consistency of MA might also be considered as an advantage over EA. Less runs would be necessary in the case of MA, what indicates a better computational efficiency. Additionally, if more complicated structures and with more actuators are considered, benefits of using the MA algorithm are even more significant (Garg, 2009).

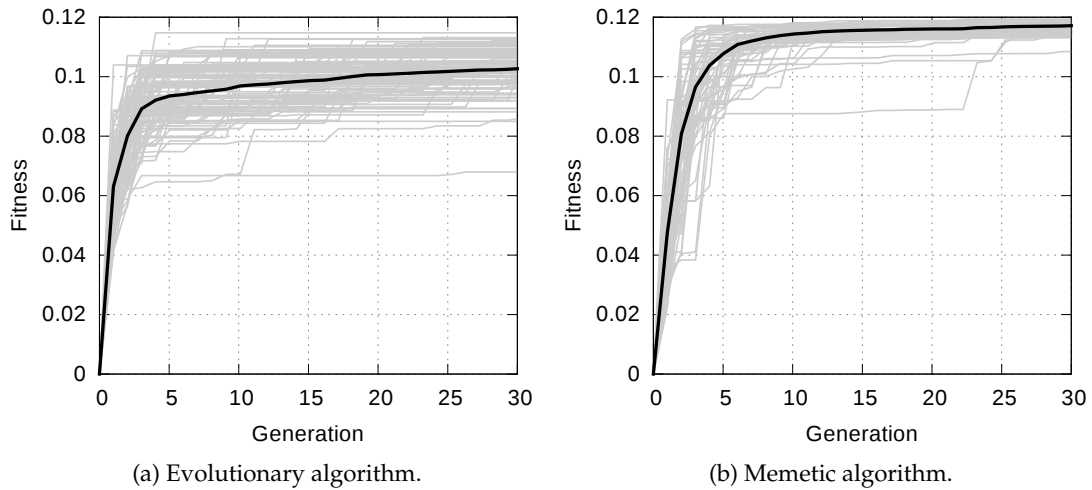


Figure 5.2: Multiple runs of optimization algorithms.

Table 5.1: Comparison of characteristic values.

Properties	Evolutionary algorithm	Memetic algorithm
Runs	100	100
Generations	30	30
Population size	90	20
Best final fitness	0.114	0.119
Average final fitness	0.102	0.116
Worst final fitness	0.068	0.108

### 5.3 Identification of model boundary conditions

In this Section, the optimization algorithm is used to identify the model parameters, to better fit it to the real plant. It is a step that often is inevitable, and should precede the application of the model, e.g. to objectives presented in the following Section.

#### 5.3.1 Formulation of the optimization problem

The goal of the optimization here is to find eight spring constants (considered as optimization variables) describing elastically restrained boundary conditions in the mathematical model of the light-weight casing walls. They are optimized in the sense of fitting the theoretically calculated natural frequencies and modeshapes to their corresponding values of real casing obtained by experimental measurements.

Although only the spring constant are considered here, the same approach can be used to identify other model parameters, depending on the application. What complicates the process, is that the mathematical model is recalculated each time, when different set of parameters is evaluated (even the trial functions, as the boundary conditions changes).

### 5.3.2 Cost function

The cost function is expressing the discrepancy between theoretically predicted natural frequencies and those obtained by experiments. In this considerations, it is formulated as follows:

$$J = \sum_i \left( \frac{\omega_{e,i} - \omega_{s,i}}{\omega_{e,i}} \right)^2, \quad (5.1)$$

where  $\omega_{e,i}$  and  $\omega_{s,i}$  are the  $i$ -th corresponding natural frequencies, measured experimentally and simulated with the model, respectively. The sum is over the set of selected resonances, which are not necessarily consecutive. Generally speaking, the cost function (5.1) expresses an error of modelling—difference between the experiment and the model. It is noteworthy that corresponding natural frequencies  $\omega_{e,i}$  and  $\omega_{s,i}$  are not associated according to the order in frequency domain, but according to the distinguished modeshape (identified by the number of the nodal lines reduced by one, parallel to  $y$  and  $x$  directions, respectively). Hence, for the example of the top wall—the 1st, 2nd, 10th and 11th resonances are identified by their modeshapes  $(1, 1)$ ,  $(2, 1)$ ,  $(4, 2)$  and  $(3, 3)$ , and their natural frequencies 23 Hz, 38 Hz, 146 Hz and 155 Hz, respectively.

### 5.3.3 Preparation of experimental data

As it was pointed out in the previous Chapters, not all of the eigenmodes in the considered frequency range were excited equally. Some of the less excited eigenmodes were even difficult to observe, because of vicinity of more excited ones. Hence, for each casing wall, four of well observed eigenmodes are selected for the identification process. For the top wall (used as an example here), 1st, 2nd, 10th and 11th eigenmodes are chosen for the purpose of identification. Remaining eigenmodes are used only for evaluation of the model accuracy.

### 5.3.4 Results

A memetic algorithm is used to find the optimal values of model parameters. As a result, following spring constants were obtained for the top wall:

$$\begin{aligned} k_{rx0} &= 27.0, & k_{rx1} &= 27.0, & k_{ry0} &= 61.8, & k_{ry1} &= 61.8, \\ k_{tx0} &= 1.1, & k_{tx1} &= 1.1, & k_{ty0} &= 8.7, & k_{ty1} &= 8.7, \end{aligned} \quad (5.2)$$

for the front wall:

$$\begin{aligned} k_{rx0} &= 53.6, & k_{rx1} &= 53.6, & k_{ry0} &= 1.5, & k_{ry1} &= 50.7, \\ k_{tx0} &= 24.7, & k_{tx1} &= 24.7, & k_{ty0} &= 26.9, & k_{ty1} &= 28.3, \end{aligned} \quad (5.3)$$

and for the left wall:

$$\begin{aligned} k_{rx0} &= 63.2, & k_{rx1} &= 63.2, & k_{ry0} &= 19.0, & k_{ry1} &= 23.1, \\ k_{tx0} &= 1.2, & k_{tx1} &= 1.2, & k_{ty0} &= 24.8, & k_{ty1} &= 22.2. \end{aligned} \quad (5.4)$$

Due to a symmetry of the casing structure, identity of opposite symmetrical boundary conditions parameters were assumed. Value of the optimization index (5.1) obtained for the exemplary top wall is:

$$J_{opt} = 0.001678. \quad (5.5)$$

A comparison of initial 12 eigenmodes (simulated for optimal set of spring constants and measured experimentally) of the top, front and left wall are given in previous Chapter, in Figs. 4.15-4.17, respectively. It was expected that frequencies of eigenmodes selected for the cost function would be consistent. However, remaining eigenmodes that were observed, but were not used in the identification process, are also consistent with the model, confirming the correctness of the proposed procedure.

## 5.4 Optimization of a vibrating structure

In this Section, the introduced memetic algorithm is used to optimize the vibrating structure itself (and/or its active control system) by an appropriate placing of additional elements on its surface.

### 5.4.1 Formulation of the optimization problem

Shape and placement of additional elements bonded to a vibrating structure surface are considered as a set of optimization variables. They are optimized in the sense of minimizing an arbitrarily chosen cost function. The cost function corresponds to desired frequency response of the plate and/or controllability/observability measures of an active system, depending on the given application. Four kinds of elements are considered:

- Additional masses

They are passive elements. A significant amount of different items can be utilized in this role, including custom-made elements. Hence the shape, weight and placement are considered as optimization variables.

- Ribs

They are passive elements. It is assumed for practical reasons that one of their dimensions is much greater than the others, and that their cross-sections are constant along this direction. Therefore, the length, cross-section, location and orientation are considered as optimization variables.

- Actuators

For the purpose of this research, electrodynamic shakers are adopted as actuators, although other kinds can also be considered and appropriately introduced in the model, e.g. PZT films, PZT stacks or MFC (Leniowska and Mazan, 2015). The actuators are used to generate sound by the vibrating panel or for active control

purposes. Their shape is often imposed by a manufacturer, and therefore only the placement becomes an optimization variable.

- Sensors

Accelerometers are used in this research to monitor vibration or provide signals for a control algorithm. Other sensors can also be considered and appropriately introduced in the model, e.g. strain gauges, MFC elements or PVDF films. Due to the same reason as in case of actuators, only the placement is considered as an optimisation variable.

Furthermore, the variables specified above, are subjects to various restraints - the number, weight and dimensions of the elements are limited due to plate shape and other constraints dependent on the application.

A property of the optimization algorithm is that if one or more of the elements do not allow obtaining a better fitness, these elements are either placed at the plate border where they do not affect the plate in practice, or their parameters like weight or length are reduced to negligible values. Hence, the number of optimized elements often acts in fact like an upper bound.

#### 5.4.2 Cost function

The cost functions used in the present considerations should reflect discrepancy between the desired and actual frequency responses of the plate. Various approaches can be utilized to define the cost function. They can be defined on the basis of natural frequencies,  $\omega_i$ , and magnitudes of the response, where  $i$  stands for the eigenmode number. On the other hand, overall transmission in a whole bandwidth can also be specified to be either amplified or attenuated, depending whether the role of the plate is to act as a structural noise source or a noise barrier, respectively.

If an active structural control application is considered, measures of controllability and observability of the system expressed in the form of diagonal elements of the controllability and observability Gramian matrices,  $\lambda_{c,i}$  and  $\lambda_{o,i}$ , respectively, can also be introduced in the cost function, as it was done in the previous work of the author (Wrona and Pawelczyk, 2013b,a). Therefore, in the general form the cost function can be presented as:

$$J = f(\omega_i, \lambda_{c,i}, \lambda_{o,i}, \Theta) , \quad (5.6)$$

where  $\Theta$  is a vector representing parameters of the elements to be mounted to the plate, including their shapes and locations. More detailed forms of particular cost functions are presented in the following Subsection, where results for different scenarios are shown and discussed.

In the present analysis, the numbers of subsequent elements mounted to the plate, for simplification, are not a subject of optimization. They are chosen at the beginning as initialization parameters, in a similar manner as the structure of a model for the system

identification process. If the result obtained for certain numbers of elements is not satisfactory, the numbers should be increased (similarly as the orders of a model would be increased). However, simpler configurations are usually more desired. Therefore, if the goal is reached, the possibility of reduction should be explored - sometimes a satisfactory result can be obtained for lower numbers of elements (like the lower order of a model). It means that the chosen final number of elements should be a trade-off between the quality of obtained result and the complexity of the solution. Therefore, it can be defined in a similar way as the Akaike Information Criterion (AIC) for system identification.

In the exemplary cases reported in the following Subsection, the choice of numbers of elements is made according to the guidelines described above. However, for the sake of brevity, this process is not discussed for particular cases.

### 5.4.3 Actuators and sensors arrangement for the rigid casing

The developed model and the memetic algorithm are used in this Subsection to optimize locations of three inertial actuators mounted to the rigid casing wall. The objective is to ensure controllability of initial six eigenmodes, by maximizing following criterion:

$$J = \min_i \lambda_{c,i} , \quad i \in \{1, 2, \dots, 6\} , \quad (5.7)$$

where  $\lambda_{c,i}$  is the  $i$ -th diagonal element of the controllability Gramian matrix, corresponding to the  $i$ -th eigenmode (Wrona and Pawelczyk, 2013b). Such optimization index expresses a measure of controllability of the least controllable mode. The optimization is performed in a continuous spatial domain for admissible actuators placement. What complicates the process, is that the mathematical model is recalculated each time, when different arrangement of actuators is evaluated (as the actuators' mass is taken into account in the plate model). Actuators locations found are shown in Fig. 5.3a. Obtained diagonal elements of the controllability Gramian corresponding to eigenmodes are presented in Fig. 5.3b.

After the optimization process, the actuators have been mounted on the casing wall in the obtained arrangement and experimentally evaluated. Each of the actuators have been individually excited with a random signal. Frequency responses of the panel due to excitation by individual actuators were measured at a number of points, uniformly distributed over the plate surface. The distance between the measurement points (determining the number of them) has been adopted to be considerably smaller than the distance between the nodes and antinodes of the plate eigenmodes in the frequency range considered. Results averaged over all of the measurement points are presented in Fig. 5.4.

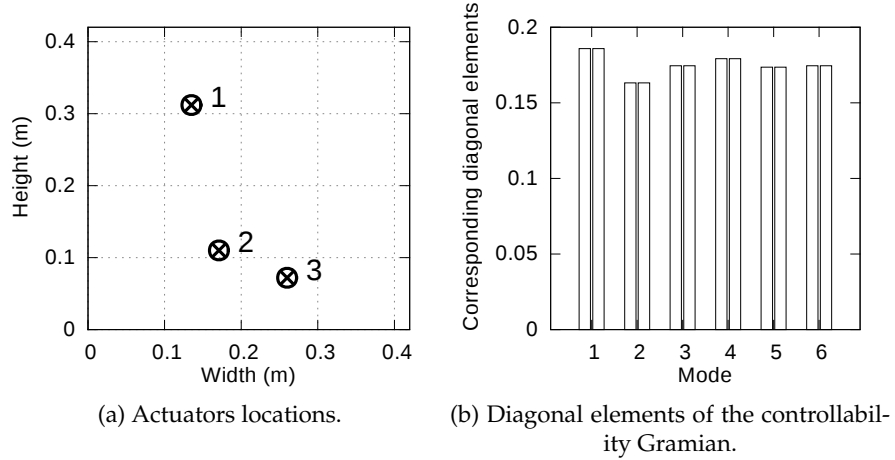


Figure 5.3: Results of the optimization.

The given eigenmode is considered practically controllable (with acceptable control effort) if the corresponding peak is distinguishable in the frequency response graph. It follows from analysis of Fig. 5.4 that individual actuators complement each other. Every actuator excites the first mode, but e.g. the forth mode is well excited only by the actuator no. 1. Hence, each desired eigenmode is controllable with an acceptable margin, what experimentally confirms suitability of the proposed method.

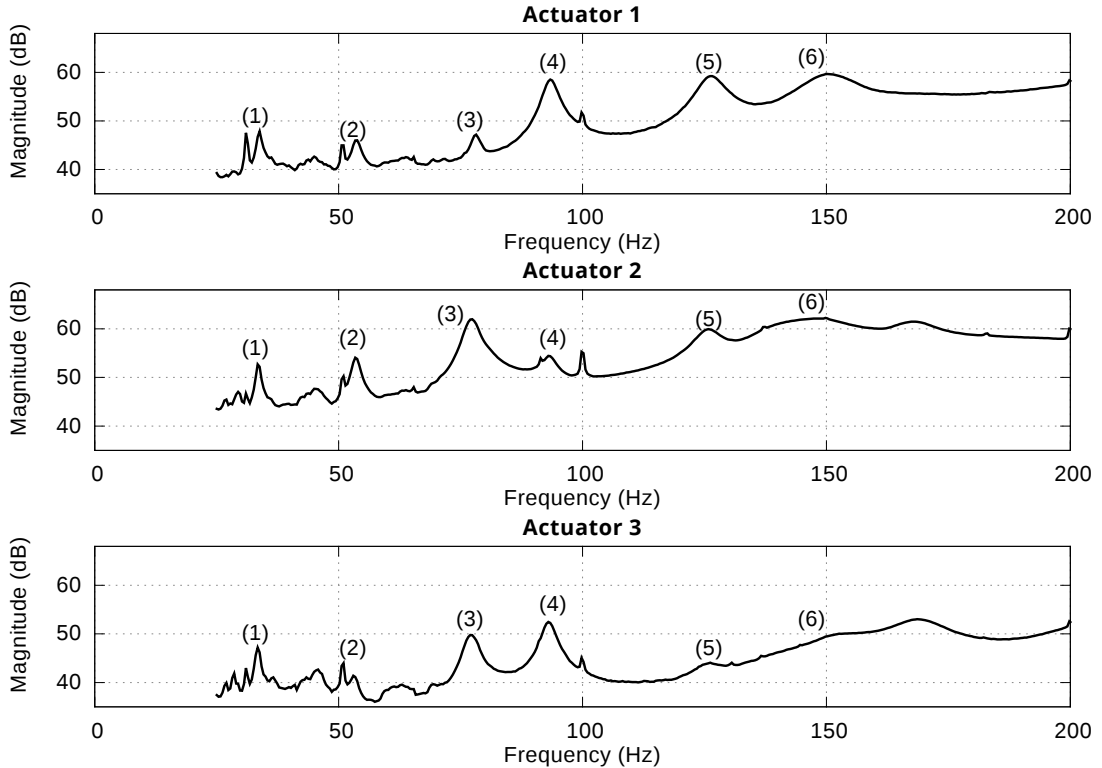


Figure 5.4: Magnitudes of surface-averaged frequency responses of the plate due to excitation by individual actuators (the numbers in parentheses depict eigenfrequencies).

#### 5.4.4 Actuators and sensors arrangement for the light-weight casing

As the mathematical model has been validated for the light-weight casing walls, it is now employed for the process of optimization of arrangement of actuators. Each wall is evaluated in this process separately, therefore it is performed in the same manner as in previous Subsection or in (Wrona and Pawelczyk, 2013b), where the individual casing wall is considered.

The optimization itself is performed with a memetic algorithm. The optimization variables are the coordinates of actuators on the plate surface. The optimization index  $J$  is a measure of controllability of the least controllable mode:

$$J = \min_i \lambda_{c,i} , \quad i \in \{1, 2, \dots, N_{mod}\} , \quad (5.8)$$

where  $\lambda_{c,i}$  is the  $i$ -th diagonal element of the controllability Gramian matrix, corresponding to the  $i$ -th eigenmode (Wrona and Pawelczyk, 2016e).

The goal is to maximize the controllability of eigenmodes in the frequency range up to 300 Hz. Hence, depending on the number of eigenmodes included in the given

Wall	Act.	$x_{a,i}$ (m)	$y_{a,i}$ (m)
Top	1	0.100	0.066
	2	0.322	0.445
	3	0.389	0.564
	4	0.610	0.091
	5	0.695	0.247
Left	1	0.077	0.455
	2	0.424	0.152
	3	0.542	0.222
	4	0.565	0.304
Front	1	0.134	0.065
	2	0.307	0.164
	3	0.674	0.445
	4	0.735	0.263

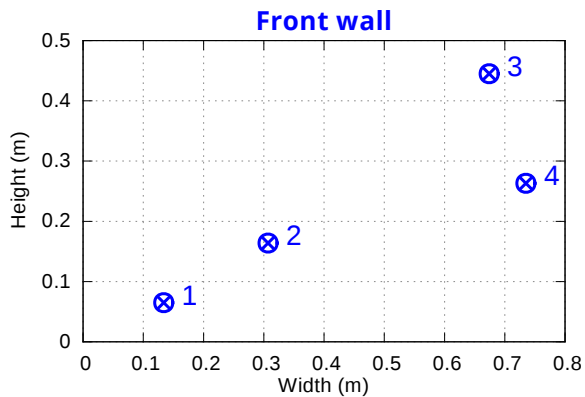
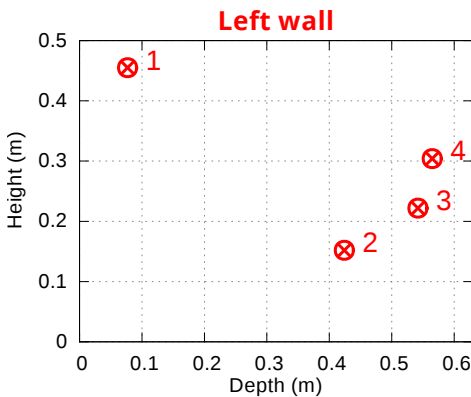
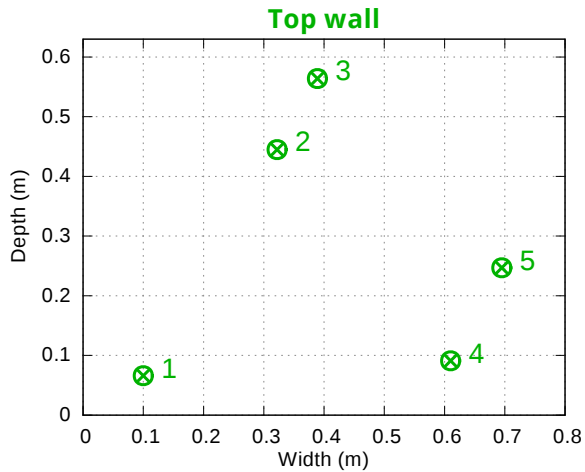


Figure 5.5: Arrangement of actuators on the light-weight casing walls. Two pairs of walls are symmetrical (left and right, front and back), hence only one of each pair is presented.

frequency range, different number of eigenmodes was considered for each wall of the casing:  $N_{mod} = 25$  for top wall,  $N_{mod} = 21$  for front and back wall,  $N_{mod} = 17$  for left and right wall. Five actuators locations have been optimized for the top wall and four actuators locations for remaining walls.

As the two pairs of walls are symmetrical (left and right, front and back), the same configuration have been calculated for a given pair. The obtained arrangement of actuators is presented in Fig. 5.5.

#### 5.4.5 Frequency response shaping method

Vibrating plates can be used as structural sound sources, highly resistant to unfavourable environmental conditions. On the other hand, they can be used as noise barriers, which limit the acoustic energy transmission/emission (Rdzanek, 2014; Rdzanek and Witkowski, 2014; Leniowska and Rdzanek, 2014; Batko et al., 2015). In the latter case their vibration can be appropriately controlled with the aid of actuators to enhance their noise isolation (Pawelczyk, 2013). However, they exhibit complex frequency response, which can make it difficult to achieve satisfactory performance. Therefore, for both kinds of applications, it would be great to have an ability to shape the frequency response as desired. By locating resonance modes at excited frequencies the sound power radiated could be significantly increased (Mazur, 2013; Zawieska et al., 2007; Zawieska and Rdzanek, 2007). In case of noise barriers, by relevant shaping of the frequency response a higher passive attenuation could be obtained or active control ability could be improved. Frequency response shaping can also enhance efficiency of energy harvesting from vibrating structures (Kowal et al., 2008).

General rules are known—additional masses lower the natural frequencies of the plate, whereas ribs elevate them. This can be easily observed in simulations with softwares for modal analysis. However, besides the previous publications of the author (Wrona and Pawelczyk, 2016e,f), presence of additional masses and ribs has not been analysed and used together, especially for shaping the frequency response according to precisely defined demands.

It is proposed to simultaneously optimise arrangement of additional masses and ribs in order to reach precisely defined desired properties of the plate. The limits are related mainly to the maximum dimensions and mass of the created structure. Moreover, this approach can be employed for active structural control applications to reduce vibration and/or noise as well. In such case, actuator and sensors bonded to the plate are modelled as additional masses of imposed shapes and weights. However, they are distinguished from the passive masses in notation, because locations of these elements determine the controllability and observability of the system. In this research, accelerometers and inertial actuators are considered, as examples of sensors and actuators. However, this general idea can easily be applied for other kinds of sensors and actuators. Such sophisticated optimisation, and shaping properties of the structure according to demands of various character followed from defined cost functions and

constraints, would not be possible with available softwares for modal analysis. Hence, both the memetic algorithm and mathematical model of the plate are implemented in authors' original software, utilizing C language and GPU support.

In this Subsection, exemplary optimization scenarios, and corresponding different cost functions are presented and discussed. Beginning with simple intuitive cases to evaluate correctness of obtained configuration, and then more complex cases are considered to demonstrate full potential of the method.

Plate parameters for all cases considered in this Subsection are as follows:

$$\begin{aligned} a &= 0.420 \text{ m}, & b &= 0.420 \text{ m}, & h &= 0.001 \text{ m}, \\ E &= 200 \text{ GPa}, & G &= 76.9 \text{ GPa}, \\ \rho_p &= 7850 \text{ kg/m}^3, & \nu &= 0.3, & \kappa &= 5/6. \end{aligned}$$

Plate edges are assumed to be fully-clamped. This is due to the fact that such boundary conditions correctly represent structures often encountered in practice. Moreover, they are commonly used in many different plate models, which would facilitate a comparison with the reported results. However, the model derived in this dissertation can be used for any boundary conditions (Pawelczyk and Wrona, 2016).

The frequency bandwidth is considered up to 350 Hz, and initial 12 eigenmodes of the plate are compared for each case. For unloaded plate, natural frequencies are given in Tab. 5.2. The frequency response of such plate is given in Fig. 5.6.

For each optimization, the population consist of 50 individuals. Maximum number of generations is set to 10. Probability of crossover, mutation and individual learning is 0.2, 0.3 and 0.1, respectively.

Weights of additional masses are limited to maximum value of 0.2 kg. The concentrated masses are assumed to be placed directly at the place surface, therefore moments of inertia are defined by:

$$I_{mx,i} = I_{my,i} = m_{m,i} \left( \frac{h}{2} \right)^2, \quad (5.9)$$

where  $m_{m,i}$  is the weight of the  $i$ -th additional mass. The ribs are assumed to have a constant cross-section of square shape, defined by dimensions:

$$e_{r,i} = h_{r,i} = 0.004 \text{ m}, \quad (5.10)$$

where  $e_{r,i}$  is the width and  $h_{r,i}$  is the height of the  $i$ -th rib. Such cross-section implies that geometric properties of the ribs are given by:

$$\begin{aligned} A_{r,i} &= e_{r,i} h_{r,i}, & I_{r,i} &= \frac{1}{12} e_{r,i} h_{r,i}^3 + e_{r,i} h_{r,i} \left( \frac{h + h_{r,i}}{2} \right)^2, \\ J_{r,i} &= \frac{1}{12} e_{r,i} h_{r,i}^3 + \frac{1}{12} h_{r,i} e_{r,i}^3, & k_{r,i} &= \frac{1}{12} h_{r,i}^2, \end{aligned} \quad (5.11)$$

Table 5.2: Natural frequencies of unloaded plate.

Mode	1	2	3	4	5	6	7	8	9	10	11	12
$\omega_i$ (Hz)	49.7	101.4	101.4	149.5	181.8	182.6	227.9	227.9	290.8	290.8	303.9	334.5

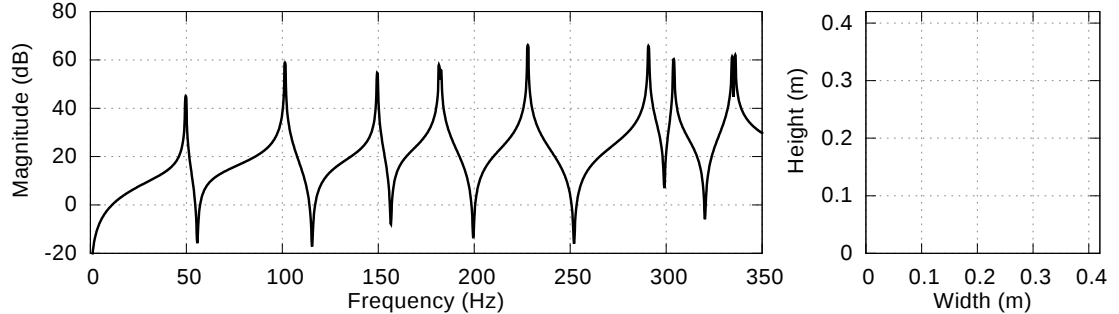


Figure 5.6: The frequency response of unloaded plate and visualization of additional elements mounted on the plate (there are no elements for the unloaded plate).

where  $A_{r,i}$  is the cross-sectional area;  $I_{r,i}$  is the second moment of inertia about the plate mid-plane;  $J_{r,i}$  is the torsional constant;  $k_{r,i}$  is the radius of gyration of the  $i$ -th rib. The material of the ribs is considered to be the same as of the plate.

### Minimization of the fundamental frequency

As an intuitive example, minimization of the fundamental frequency is considered firstly. Such goal implies the following cost function:

$$J = \omega_1 . \quad (5.12)$$

Only passive elements are considered in this case. The number of additional masses and ribs is set here to  $N_m = 1$  and  $N_r = 1$ , respectively. Results of the optimization are given in Tab. 5.3 and Fig. 5.7, where circles and lines represent placements of additional masses and ribs, respectively.

It follows from the optimisation that to minimize the fundamental frequency, the maximum possible amount of additional mass should be mounted on the plate surface, considering the modeshape, at its centre. The algorithm reached such solution, with

Table 5.3: Results of optimization of cost function (5.12) for  $N_m = N_r = 1$ . Natural frequencies of the plate and placement of additional elements.

Mode	1	2	3	4	5	6	7	8	9	10	11	12
$\omega_i$ (Hz)	35.4	94.4	94.4	132.8	149.4	181.7	195.8	195.8	243.9	243.9	270.0	334.4
Masses	$x_{m,i}$ (m)	$y_{m,i}$ (m)	$m_{m,i}$ (kg)		Ribs	$x_{r0,i}$ (m)	$y_{r0,i}$ (m)	$x_{r1,i}$ (m)	$y_{r1,i}$ (m)			
1	0.210	0.212	0.200		1	0.238	0.235	0.240	0.235			

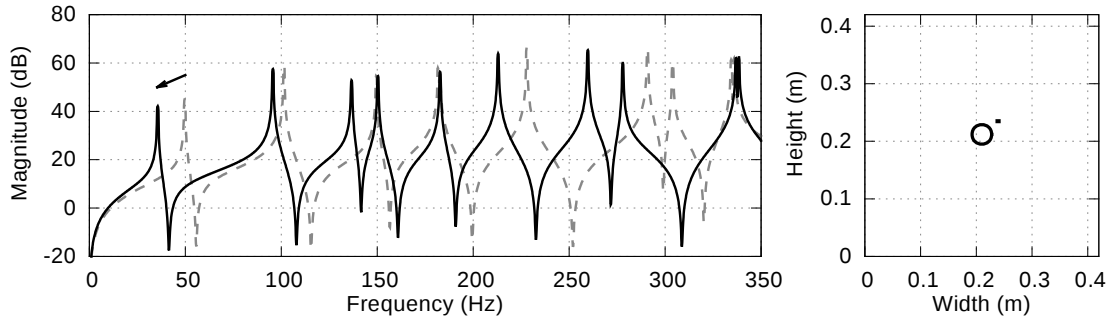


Figure 5.7: Results of optimization of cost function (5.12) for  $N_m = N_r = 1$ . The frequency response of the plate (solid line - plate with elements; dashed line - unloaded plate) and visualization of additional elements mounted on the plate (circles - additional masses; lines - ribs).

cost function value  $J_{opt} = 35.4$ . This value was limited by assumed in a constraint that the largest allowed mass of the additional element is 0.2 kg. Moreover, a typical behaviour of the algorithm can be observed in this example. The optimisation process resulted in a plate rib of negligible length, what means that its employment here is not justified.

For the same cost function, the optimization was performed again, but for doubled number of elements, setting  $N_m = 2$  and  $N_r = 2$ . Results of the optimization are given in Tab. 5.4 and Fig. 5.8.

Table 5.4: Results of optimization of cost function (5.12) for  $N_m = N_r = 2$ . Natural frequencies of the plate and placement of additional elements.

Mode	1	2	3	4	5	6	7	8	9	10	11	12					
$\omega_i$ (Hz)	28.7	86.8	86.8	123.0	149.4	165.4	165.5	181.7	238.5	238.5	265.5	333.6					
Masses	$x_{m,i}$ (m)	$y_{m,i}$ (m)	$m_{m,i}$ (kg)										Ribs	$x_{r0,i}$ (m)	$y_{r0,i}$ (m)	$x_{r1,i}$ (m)	$y_{r1,i}$ (m)
1	0.210	0.212	0.200										1	0.367	0.392	0.371	0.392
2	0.211	0.211	0.200										2	0.415	0.000	0.420	0.000

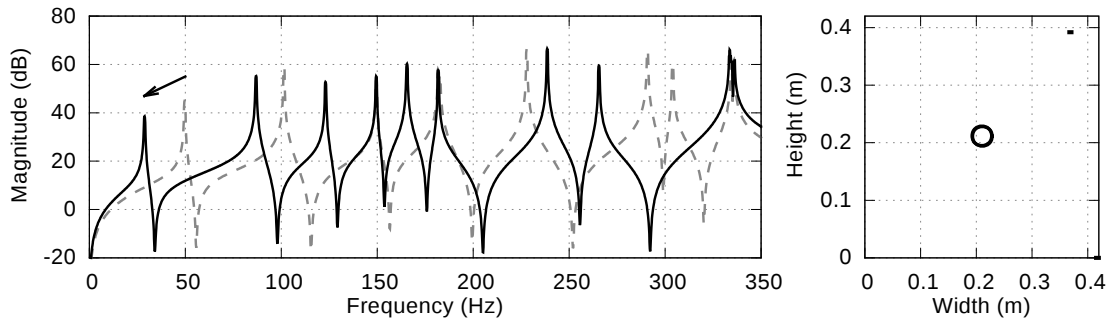


Figure 5.8: Results of optimization of cost function (5.12) for  $N_m = N_r = 2$ . The frequency response of the plate (solid line - plate with elements; dashed line - unloaded plate) and visualization of additional elements mounted on the plate (circles - additional masses; lines - ribs).

As it could be predicted, even more mass is concentrated at the plate center, achieving  $J_{opt} = 28.7$ . Moreover, the ribs are thrown to the plate corners. It is also worth noting that despite increasing number of dimensions of the search space, the algorithm easily reaches a proper solution. The solutions obtained in this subsection are in accordance with intuition and with results known from the literature.

### Maximization of the fundamental frequency

Considering the opposite goal to that from the previous case, maximization of the fundamental frequency is of concern now. It implies the following cost function:

$$J = -\omega_1 . \quad (5.13)$$

Again, only passive elements are considered. The number of additional masses and ribs is set to  $N_m = 1$  and  $N_r = 1$ , respectively. Results of the optimization are given in Tab. 5.5 and Fig. 5.9. The value of the cost function is  $J_{opt} = -88.4$ . It follows from the optimisation that the rib has been placed in the most efficient position, i.e. to split the plate into two. Moreover, the additional mass was placed at the plates edge, indicating that its presence is not justified. The solution is again in accordance with intuition and with results known from the literature.

Table 5.5: Results of optimization of cost function (5.13) for  $N_m = N_r = 1$ . Natural frequencies of the plate and placement of additional elements.

Mode	1	2	3	4	5	6	7	8	9	10	11	12
$\omega_i$ (Hz)	88.4	106.5	160.0	164.0	191.8	239.9	243.7	296.7	311.5	346.7	348.7	353.6
Masses	$x_{m,i}$ (m)	$y_{m,i}$ (m)	$m_{m,i}$ (kg)		Ribs	$x_{r0,i}$ (m)	$y_{r0,i}$ (m)	$x_{r1,i}$ (m)	$y_{r1,i}$ (m)			
1	0.420	0.024	0.027		1	0.210	0.000	0.210	0.420			

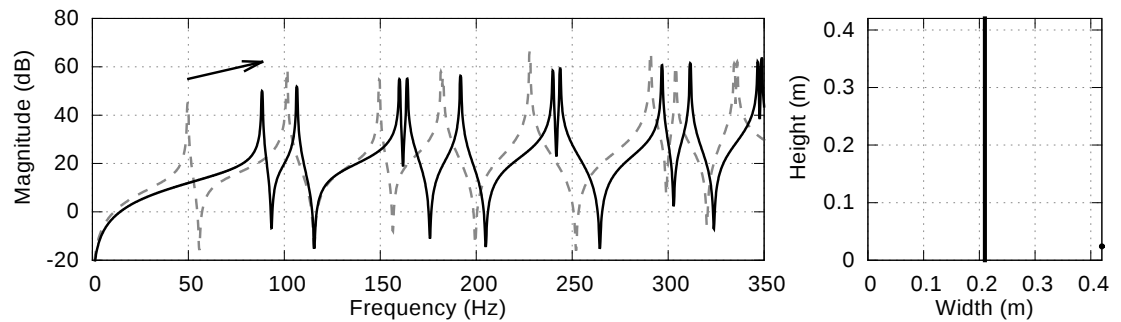


Figure 5.9: Results of optimization of cost function (5.13) for  $N_m = N_r = 1$ . The frequency response of the plate (solid line - plate with elements; dashed line - unloaded plate) and visualization of additional elements mounted on the plate (circles - additional masses; lines - ribs).

### Setting natural frequencies at desired values

In cases presented above, the optimal arrangements of masses and ribs could be predicted without the optimization process. However, it was conducted to evaluate the performance of the algorithm before considering more complex scenarios, where intuitive answers are no longer available.

Here, it is assumed that exact values of desired natural frequencies are arbitrary chosen. The aim of the optimization is to find arrangement of the additional elements mounted on the plate for it to respond accordingly. To represent such goal the cost function, two approaches can be distinguished. Distances with respect to the nearest natural frequencies, or with respect to particular ones, e.g. determined by the number of the mode are minimised. Selection of the approach depends on the given application, whether the goal is to place any of the modes at desired position or to shape the frequency characteristic precisely as desired.

In the given example, the second scenario is adopted as a more general. The exemplary requirement is to place the initial four natural frequencies at desired values  $\omega_{sp,1} = 75 \text{ Hz}$ ,  $\omega_{sp,2} = 125 \text{ Hz}$ ,  $\omega_{sp,3} = 175 \text{ Hz}$  and  $\omega_{sp,4} = 225 \text{ Hz}$ . Then, the cost function

Table 5.6: Results of optimization of cost function (5.14) for  $N_m = N_r = 3$ . Natural frequencies of the plate and placement of additional elements.

Mode	1	2	3	4	5	6	7	8	9	10	11	12
$\omega_i$ (Hz)	75.2	125.6	174.5	224.9	233.4	257.7	329.1	334.2	364.4	371.5	383.8	429.6
Masses	$x_{m,i}$ (m)	$y_{m,i}$ (m)	$m_{m,i}$ (kg)	Ribs	$x_{r0,i}$ (m)	$y_{r0,i}$ (m)	$x_{r1,i}$ (m)	$y_{r1,i}$ (m)				
1	0.003	0.031	0.161	1	0.165	0.017	0.314	0.339				
2	0.002	0.031	0.200	2	0.121	0.046	0.154	0.384				
3	0.003	0.032	0.200	3	0.142	0.023	0.399	0.262				

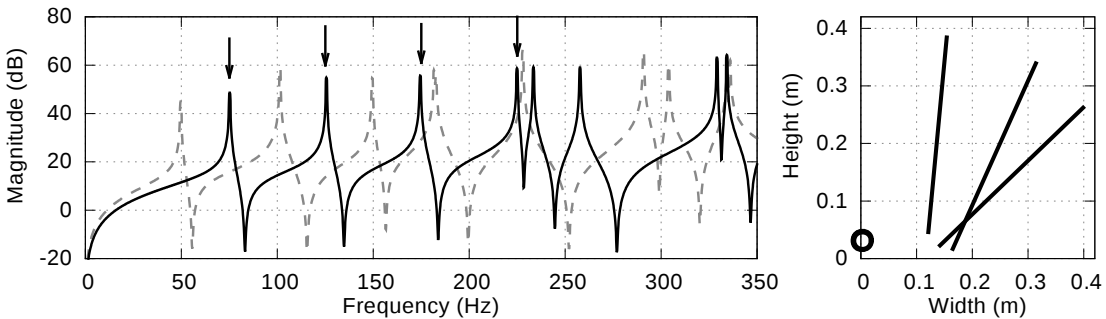


Figure 5.10: Results of optimization of cost function (5.14) for  $N_m = N_r = 3$ . The frequency response of the plate (solid line - plate with elements; dashed line - unloaded plate) and visualization of additional elements mounted on the plate (circles - additional masses; lines - ribs).

reflecting that is expressed as:

$$J = \sum_{i=1}^4 |\omega_i - \omega_{sp,i}| . \quad (5.14)$$

Only passive elements are considered. The number of additional masses and ribs was set to  $N_m = 3$  and  $N_r = 3$ , respectively. Results of the optimization are given in Tab. 5.6 and Fig. 5.10. The value of the cost function that was obtained is  $J_{opt} = 1.4$ .

It has been proven that the given values of desired natural frequencies have been achieved with a high accuracy. Moreover, it follows from the analysis of the obtained solution that the additional masses can be excluded from the final application, and the 3 ribs only allow to reach the goal defined by (5.14). It is an understandable behaviour, because each of the natural frequencies has been moved to higher values than in case of the unloaded plate.

### Setting natural frequencies away from the given value

In this example, the opposite scenario to that from the previous Subsection is considered. The goal is to keep natural frequencies as far as possible from the given frequency. For instance, it corresponds to a practical application, where the frequency of the disturbance is known and the aim is to avoid the excitement of natural frequencies of the plate, thereby increasing its passive isolation. Assuming that such frequency is  $\omega_d = 175$  Hz and the mode closest to this given frequency  $\omega_d$  is the  $i$ -th mode, the cost function is expressed as:

$$J = -|\omega_i - \omega_d| , \quad i \in \{1, 2, \dots, N\} . \quad (5.15)$$

The number of additional masses and ribs is assumed as  $N_m = 2$  and  $N_r = 2$ , respectively. Results of the optimization are given in Tab. 5.7 and Fig. 5.11. The value of the cost function obtained is  $J_{opt} = -38.3$ . It means that the disturbance frequency  $\omega_d$  can fluctuate in the range of 15% around its nominal value, without the risk of approaching the natural frequencies. Moreover, if the safety margin should be even higher, the number of optimized elements should be increased.

Table 5.7: Results of optimization of cost function (5.15) for  $N_m = N_r = 2$ . Natural frequencies of the plate and placement of additional elements.

Mode	1	2	3	4	5	6	7	8	9	10	11	12
$\omega_i$ (Hz)	64.8	97.0	134.3	136.7	213.4	214.2	224.3	257.8	281.5	333.8	340.1	351.7
<hr/>												
Masses	$x_{m,i}$ (m)	$y_{m,i}$ (m)	$m_{m,i}$ (kg)	Ribs	$x_{r0,i}$ (m)	$y_{r0,i}$ (m)	$x_{r1,i}$ (m)	$y_{r1,i}$ (m)				
1	0.000	0.113	0.200	1	0.186	0.036	0.369	0.176				
2	0.069	0.122	0.159	2	0.055	0.248	0.290	0.075				

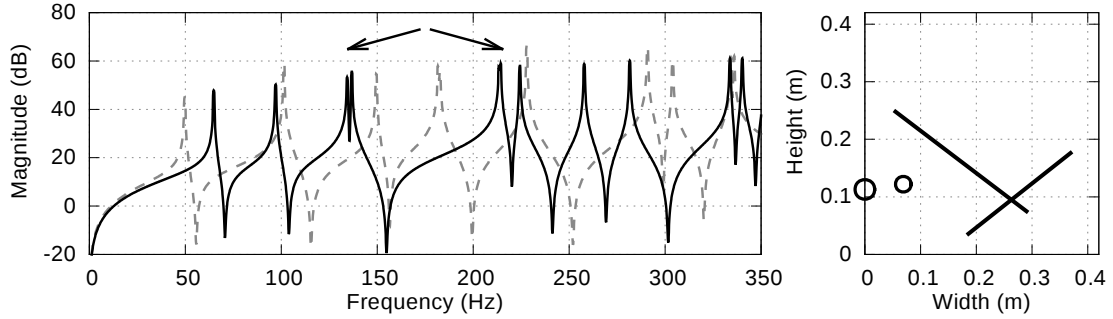


Figure 5.11: Results of optimization of cost function (5.15) for  $N_m = N_r = 2$ . The frequency response of the plate (solid line - plate with elements; dashed line - unloaded plate) and visualization of additional elements mounted on the plate (circles - additional masses; lines - ribs).

It is noteworthy that this exemplary scenario was used in an experiment validating the suitability of the employed frequency response shaping method. It is described in the previous Chapter, in Subsection 4.3.1.

### Simultaneous optimization of arrangement of actuators, sensors, and passive elements

In this subsection, an active control scenario is considered. Among the additional masses and ribs, actuators and sensors need to be arranged. Hence, the cost function should express not only the frequency response of the plate, but also controllability and observability measures, as a function of actuators and sensors placement, as discussed Section 3.8. Therefore, the optimization process becomes a multi-objective problem, because control related goals are not necessarily in line with requirements imposed on the frequency response of the plate. On the other hand, the active elements have non-zero masses and they influence frequency response of the plate.

Masses of actuators and sensors are assumed as (corresponding to electrodynamic actuators and accelerometers, respectively):

$$m_{a,i} = 0.115 \text{ kg}, \quad m_{s,i} = 0.010 \text{ kg},$$

where  $m_{a,i}$  and  $m_{s,i}$  are masses of the actuators and sensors, respectively. Moments of inertia are calculated according to Eq. (5.9).

In the considered case, the goal is to keep one of the natural frequencies as close as possible to the given value  $\omega_{sp} = 200 \text{ Hz}$ . Moreover, it is required that this mode should be controllable and observable well. It corresponds to a situation, where an efficient structural sound source of particular frequency is tried to be achieved. Assuming that the mode closest to this given frequency  $\omega_{sp}$  is the  $i$ -th mode, the cost function is

Table 5.8: Results of optimization of cost function (5.16) for  $N_m = N_r = 2$  and  $N_a = N_s = 1$ . Natural frequencies of the plate and placement of additional elements.

Mode	1	2	3	4	5	6	7	8	9	10	11	12
$\omega_i$ (Hz)	65.2	105.2	138.4	184.5	200.9	221.0	248.6	276.5	312.0	328.3	343.1	377.0
Masses	$x_{m,i}$ (m)	$y_{m,i}$ (m)	$m_{m,i}$ (kg)		Ribs	$x_{r0,i}$ (m)	$y_{r0,i}$ (m)	$x_{r1,i}$ (m)	$y_{r1,i}$ (m)			
1	0.003	0.227	0.000		1	0.013	0.286	0.410	0.284			
2	0.245	0.410	0.147		2	0.243	0.022	0.363	0.200			
Actuators	$x_{a,i}$ (m)	$y_{a,i}$ (m)	$m_{a,i}$ (kg)		Sensors	$x_{s,i}$ (m)	$y_{s,i}$ (m)	$m_{s,i}$ (kg)				
1	0.117	0.294	0.115		1	0.286	0.333	0.010				

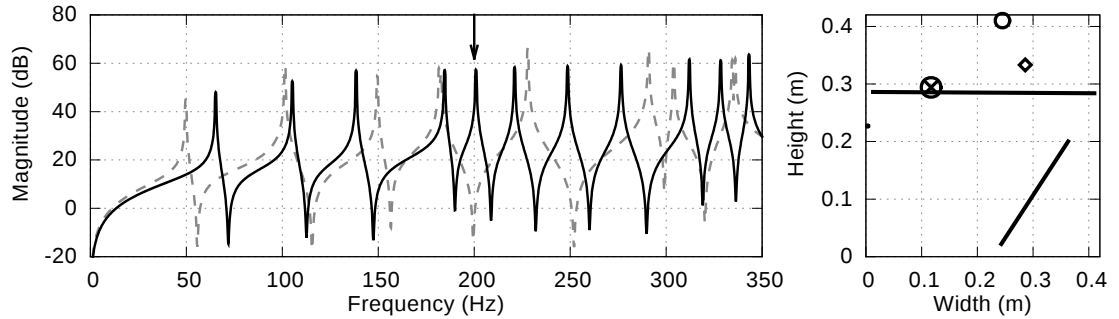


Figure 5.12: Results of optimization of cost function (5.16) for  $N_m = N_r = 2$  and  $N_a = N_s = 1$ . The frequency response of the plate (solid line - plate with elements; dashed line - unloaded plate) and visualization of additional elements mounted on the plate (circles - additional masses; lines - ribs; circles with "X" inside - actuators; diamonds - sensors).

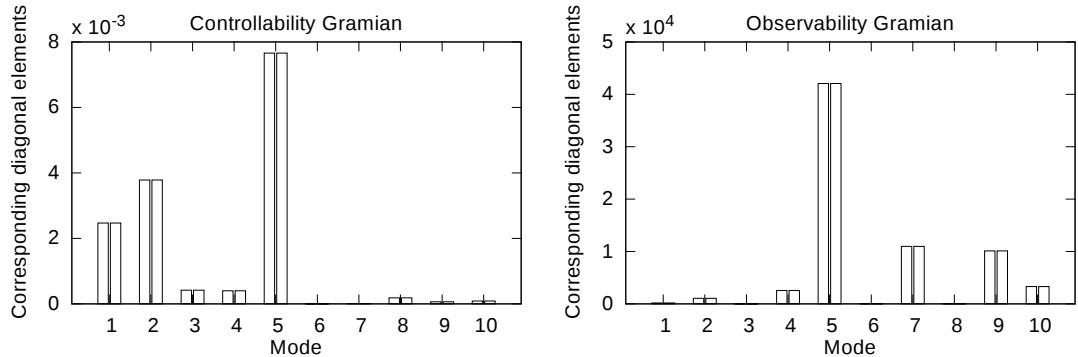


Figure 5.13: Results of optimization of cost function (5.16) for  $N_m = N_r = 2$  and  $N_a = N_s = 1$ . Values of the diagonal elements of the controllability and observability Gramian matrices.

expressed as:

$$J = -\max \left\{ \left( 1 - d_f \frac{|\omega_i - \omega_{sp}|}{\omega_{sp}} \right), 0 \right\} \cdot \lambda_{c,i} \cdot \lambda_{o,i}, \quad i \in \{1, 2, \dots, N\}, \quad (5.16)$$

where  $d_f = 10$  is a parameter defining desired proximity of the  $i$ -th mode to the given frequency  $\omega_{sp}$ . The number of additional masses, ribs, actuators and sensors was set

Table 5.9: Results of optimization of cost function (5.17) for  $N_m = 2$  and  $N_r = N_a = N_s = 3$ . Natural frequencies of the plate and placement of additional elements.

Mode	1	2	3	4	5	6	7	8	9	10	11	12
$\omega_i$ (Hz)	66.9	101.3	125.9	148.4	197.5	200.4	202.1	253.6	282.4	288.6	309.7	320.7
Masses	$x_{m,i}$ (m)	$y_{m,i}$ (m)	$m_{m,i}$ (kg)	Ribs	$x_{r0,i}$ (m)	$y_{r0,i}$ (m)	$x_{r1,i}$ (m)	$y_{r1,i}$ (m)				
1	0.042	0.157	0.014	1	0.272	0.296	0.372	0.241				
2	0.239	0.100	0.065	2	0.417	0.181	0.024	0.065				
				3	0.348	0.280	0.104	0.152				
Actuators	$x_{a,i}$ (m)	$y_{a,i}$ (m)	$m_{a,i}$ (kg)	Sensors	$x_{s,i}$ (m)	$y_{s,i}$ (m)	$m_{s,i}$ (kg)					
1	0.035	0.197	0.115	1	0.270	0.339	0.010					
2	0.049	0.309	0.115	2	0.300	0.338	0.010					
3	0.132	0.051	0.115	3	0.188	0.316	0.010					

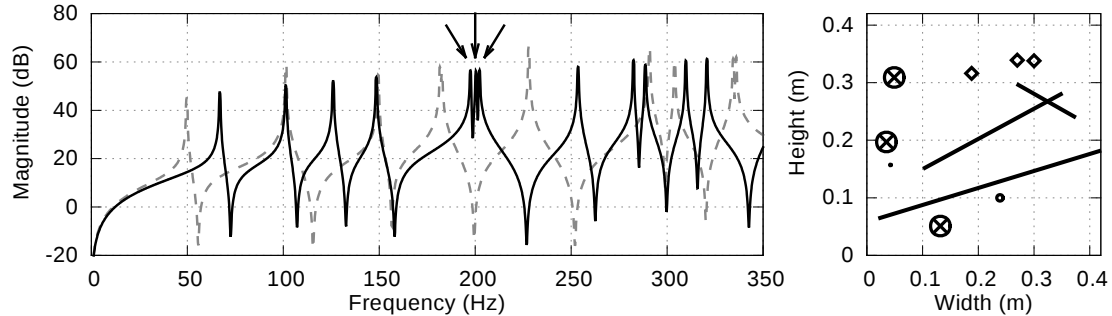


Figure 5.14: Results of optimization of cost function (5.17) for  $N_m = 2$  and  $N_r = N_a = N_s = 3$ . The frequency response of the plate (solid line - plate with elements; dashed line - unloaded plate) and visualization of additional elements mounted on the plate (circles - additional masses; lines - ribs; circles with "X" inside - actuators; diamonds - sensors).

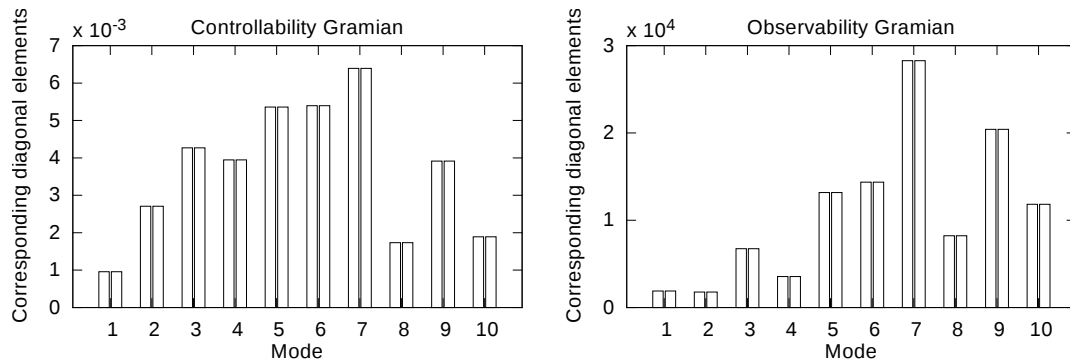


Figure 5.15: Results of optimization of cost function (5.17) for  $N_m = 2$  and  $N_r = N_a = N_s = 3$ . Values of the diagonal elements of the controllability and observability Gramian matrices.

to  $N_m = 2$ ,  $N_r = 2$ ,  $N_a = 1$  and  $N_s = 1$ , respectively. Results of the optimization are given in Tab. 5.8 and Figs. 5.12-5.13, where circles with an "X" inside and diamonds represent actuators and sensors, respectively.

Such a multi-objective optimization problem can also be defined in many ways.

However, the way presented in (5.16) leads to a solution which clearly meets the requirements for the frequency response, and provides controllability and observability for the particular mode at a high level (when compared with other modes).

In the second case considered in this Subsection, a slight modification is made to the cost function. Now not only one mode is desired near the frequency  $\omega_{sp}$ , but as many modes as possible to maximize the effect. Therefore, a sum is introduced. Moreover, to focus more on the frequency response of the plate, the values describing controllability and observability are raised to the powers of 0.5 and 0.25, respectively, leading to the cost function given as:

$$J = - \sum_{i=0}^{3N} \left[ \max \left\{ \left( 1 - d_f \frac{|\omega_i - \omega_{sp}|}{\omega_{sp}} \right), 0 \right\} \cdot (\lambda_{c,i})^{0.5} \cdot (\lambda_{o,i})^{0.25} \right]. \quad (5.17)$$

The number of additional masses, ribs, actuators and sensors was set to  $N_m = 2$ ,  $N_r = 3$ ,  $N_a = 3$  and  $N_s = 3$ , respectively. Results of the optimization are given in Tab. 5.9 and Figs. 5.14-5.15.

The value of the cost function that was obtained is  $J_{opt} = -3.1$ . The goal regarding the frequency response of the plate has been achieved with high precision. Moreover, for the modes in the proximity of the given frequency  $\omega_{sp}$ , both controllability and observability have been assured, guaranteeing usefulness of these modes for active control purposes.

## 5.5 Summary

In this Chapter, the developed model has been widely used for a series of optimization problems. The memetic algorithm has been employed as an effective optimization algorithm for problems with complex search spaces and multiple optima.

Firstly, a method of identification of model boundary conditions has been proposed and practically evaluated. It is successfully used to identify boundary conditions of the light-weight casing walls.

Afterwards, the structure optimization has been concerned. The efficient locations for actuators and sensors have been found, basing on controllability and observability measures. It is a crucial step in preparation of the active control system (if omitted, the overall performance may be significantly affected with lacks of controllability and observability).

Finally, a frequency response shaping method of casing walls has been proposed. It is validated for a set of passive and active control scenarios, including both simulation and a laboratory experiment. It represents a high practical potential, as it can be used for passive control to improve the dynamical properties of the casing walls. On the other hand, the method can be used to maximize the susceptibility of the plant to the active control.



# Chapter 6

## Active control

### 6.1 Background

After proper evaluation of the vibrating structures, when actuators and sensors (and masses and ribs, if needed) arrangement is accordingly optimized, the active control is undertaken. The general objective is common for all performed experiments—to reduce noise emission of the device, achieving global reduction instead local zones of quiet. However, to reach this goal, different signals and different strategies are utilized and compared.

In all control experiments, the adaptive feedforward control algorithm is used. It is based on Leaky Normalised Filtered-x Least Mean Square (LNFxLMS) method, employed to update control filter parameters. The adaptivity is introduced to respond to possible nonstationarity of the disturbance and changes of the plant, e.g. due to temperature variation (Mazur and Pawelczyk, 2011). Among the chosen control strategies, two general approaches can be distinguished. First approach is an independent control system for each casing wall (Wrona and Pawelczyk, 2014b, 2016b). Second approach is an integrated system for the whole casing, employing the Switched-error modification (Mazur and Pawelczyk, 2015). It is used to obtain a trade-off between inclusion of cross couplings of the plant and computational complexity. A drawback of this approach is a prolonged convergence time, however, it is a matter of a increase from several seconds (in case of an independent control) to tens of seconds in case of an integrated control system. It is still in accordance with practical implementation constrain (the system could be working for many hours, hence tens of seconds for initial convergence are acceptable). The control algorithm is further described in the Section 6.2.

The first structure considered is the rigid casing. Taking advantage of vibrational and acoustical isolation between walls, each casing wall is controlled independently (utilizing the first control approach). Outer microphones, cavity microphones or accelerometers are used as error sensors, depending on the particular configuration. Also, both single- and double-panel structures are considered, creating in total five configurations to examine (employment of cavity microphones for single-panel casing is not possible). Results are presented and discussed in Section 6.3.

Afterwards, the light-weight casing is under consideration. Due to the strong vibrational and acoustical couplings, both control approaches are evaluated (independent

and integrated). Only outer microphones are used as error sensors (cavity microphones are not possible and accelerometers performed similarly as for the rigid casing, therefore their results are omitted). Obtained results are presented, compared and discussed in Section 6.4.

## 6.2 Adaptive feedforward control system

A multi-channel feedforward control system is presented in this Section, which is used in laboratory experiments described in the following Sections. It is noteworthy that sometimes a useful reference signal (used in a feedforward system) is impossible to acquire due to, e.g. device structure preventing to place a sensor at appropriate location. In such a case, alternatively to feedforward control, a feedback control strategy in the Internal Model Control (IMC) architecture can be employed (Wrona and Pawelczyk, 2015; Mazur and Pawelczyk, 2016a). It generally provides equivalent results as a feed-forward system if the primary noise is a deterministic signal (e.g. tonal or multi-tonal signals, which are very common). However, for the sake of brevity, only feedforward control system is considered in this dissertation, as a more general approach.

The presented control system is an adaptive control strategy, based on the Leaky Normalised Filtered-x Least Mean Square algorithm used to update control filter parameters. The adaptivity is introduced to respond to possible nonstationarity of the disturbance and changes of the plant, e.g. due to temperature variation (Mazur and Pawelczyk, 2011). The stability and convergence of LMS algorithm have been studied, e.g. in (Bismor, 2015).

The control algorithm is schematically presented in Fig. 6.1. Symbol  $X$  is the reference path,  $\mathbf{W}$  is the adaptive control filters vector (of dimension  $(I \times 1)$ , where  $I$  is the number of actuators),  $\mathbf{P}$  is the primary paths vector (of dimension  $(J \times 1)$ , where  $J$  is the number of error sensors), defined between the reference and error sensors. Figure  $\mathbf{S}$  stands for the secondary paths matrix of dimension  $(J \times I)$  defined between the inputs of the actuators and outputs of the error sensors. These paths include electronics necessary for signal conditioning and data conversion. The symbol  $\hat{\mathbf{S}}$  stands for the secondary path model.

In turn,  $x(n)$  is the scalar reference signal,  $\mathbf{r}(n)$  is the filtered-reference signals matrix of dimension  $(J \times I)$ ,  $\mathbf{u}(n)$  is the control signals vector of dimension  $(I \times 1)$ . Further, signals  $\mathbf{d}(n)$  and  $\mathbf{e}(n)$  are the primary disturbances vector and the error signals vector, respectively, both of dimension  $(J \times 1)$ , at positions of the error sensors where noise reduction is desired. In the control system for each rigid casing wall, number of actuators  $I = 3$ . If a light-weight casing wall is considered,  $I = 4$  or  $I = 5$  depending on particular wall. On the other hand, depending if microphones or accelerometers are used, the number of error sensors is  $J = 1$  or  $J = I$ , respectively. Actuators and sensors are more specifically described in the Subsection 2.2.1. Depending if the microphones

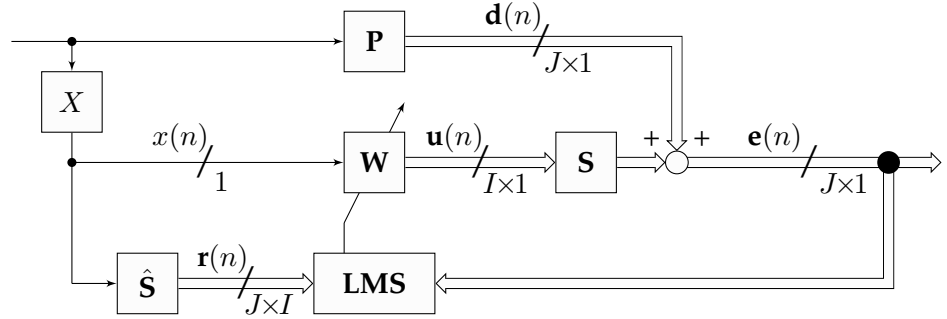


Figure 6.1: Multi-channel feedforward control system with the FxLMS algorithm.

or accelerometers are used as error sensors, the control algorithms are referred to as ASAC algorithm or AVC algorithm, respectively.

The  $i$ -th control signal at the  $(n + 1)$ -st sample,  $u_i(n + 1)$ , is obtained as follows:

$$u_i(n + 1) = \mathbf{w}_i(n)^T \mathbf{x}_u(n) , \quad (6.1)$$

where  $\mathbf{x}_u(n) = [x(n), x(n - 1), \dots, x(n - (N - 1))]^T$  is the vector of regressors of the reference signal and  $\mathbf{w}_i(n) = [w_{i,0}(n), w_{i,1}(n), \dots, w_{i,N-1}(n)]^T$  is the vector of coefficients of the  $i$ -th adaptive Finite Impulse Response (FIR) control filter at sample  $n$ , and  $N$  is the filter order. These coefficients are updated for each of the error signals  $e_j(n)$  according to the formula:

$$\mathbf{w}_i(n + 1) = \alpha \mathbf{w}_i(n) - \mu(n) \mathbf{r}_{ij}(n) e_j(n) , \quad (6.2)$$

where  $\mathbf{r}_{ij}(n) = [r_{ij}(n), r_{ij}(n - 1), \dots, r_{ij}(n - (N - 1))]^T$  is a vector of regressors of the  $ij$ -th filtered-reference signal,  $\mu(n)$  is a step-size, and  $0 \ll \alpha < 1$  is the leakage coefficient. The filtered-reference signal is calculated as:

$$r_{ij} = \hat{\mathbf{s}}_{ij}(n)^T \mathbf{x}_r(n) , \quad (6.3)$$

where  $\hat{\mathbf{s}}_{ij}(n) = [\hat{s}_{ij,0}(n), \hat{s}_{ij,1}(n), \dots, \hat{s}_{ij,M-1}(n)]^T$  is the vector of coefficients of the  $M$ -th order FIR model of the  $ij$ -th secondary path and  $\mathbf{x}_r(n) = [x(n), x(n - 1), \dots, x(n - (M - 1))]^T$  is a vector of regressors of the reference signal. For multichannel versions it is justified to consider reduction of the computational burden, as discussed in (Pawelczyk, 2002) and (Bismor et al., 2016). Under some circumstances, partial update algorithm can even increase the convergence rate (Bismor, 2014; Kurczyk and Pawelczyk, 2015).

### 6.2.1 Switched-error modification

For the light-weight casing, as shown in Subsection 2.3.3, the vibrational and acoustic cross couplings are of significant magnitude. To respond to this feature, a switched-error modification of the presented control algorithm is introduced (Mazur and Pawelczyk, 2015). The modification consist in adaptation of all control filters (corresponding to all casing walls) according to only one error signal, and cyclically changing the sensor which provides the signal. Such algorithm results in similar computation complexity as the separated control algorithm for each casing wall, but it is less vulnerable to cross couplings of the structure. However, as expected, the cost of it is the convergence speed. It is due to the fact that at once, control filters are adapting to only one of the error signals. It is approximately 10 times slower, but is still a matter of only tens of seconds to converge, which is in accordance to predefined practical requirements. The modified control algorithms is referred to as ASAC-SE (Switched-Error) algorithm. Further details are provided in (Mazur and Pawelczyk, 2015).

## 6.3 Active control of the rigid casing

In this Section, the rigid casing is evaluated by means of active control experiments. All walls of the casing, except the basis, are controlled to reduce the emission of noise generated by a primary disturbance source enclosed in the casing. Due to the vibrational and acoustical separation (see Subsection 2.2.2), each wall of the casing is controlled separately.

### 6.3.1 Experiments description

The primary noise signal is generated as a tonal signal of frequency incremented by 1 Hz in the range from 20 to 500 Hz. To achieve the goal of noise reduction, instantaneous square values of error signals are minimized by feedforward adaptive control systems, controlling together fifteen inertial actuators (three per wall). Depending on the particular configuration, the error signals are obtained by the outer microphones, the cavity microphones or by accelerometers (their arrangement is discussed in Subsection 2.2.1). The control performance is evaluated as noise reduction level observed by the room microphones. Performance of both single- and double-panel structure are evaluated and compared in this Section.

For each frequency of the primary disturbance, a 15 seconds experiment was performed. In its initial 4 seconds the active control was off, and variance of the signal acquired by different sensors was estimated as the reference point. Then, the active control was turned on. When the adaptive control algorithm converged, final 4 seconds of the experiment was used to estimate the variance of the signal acquired by corresponding sensors.

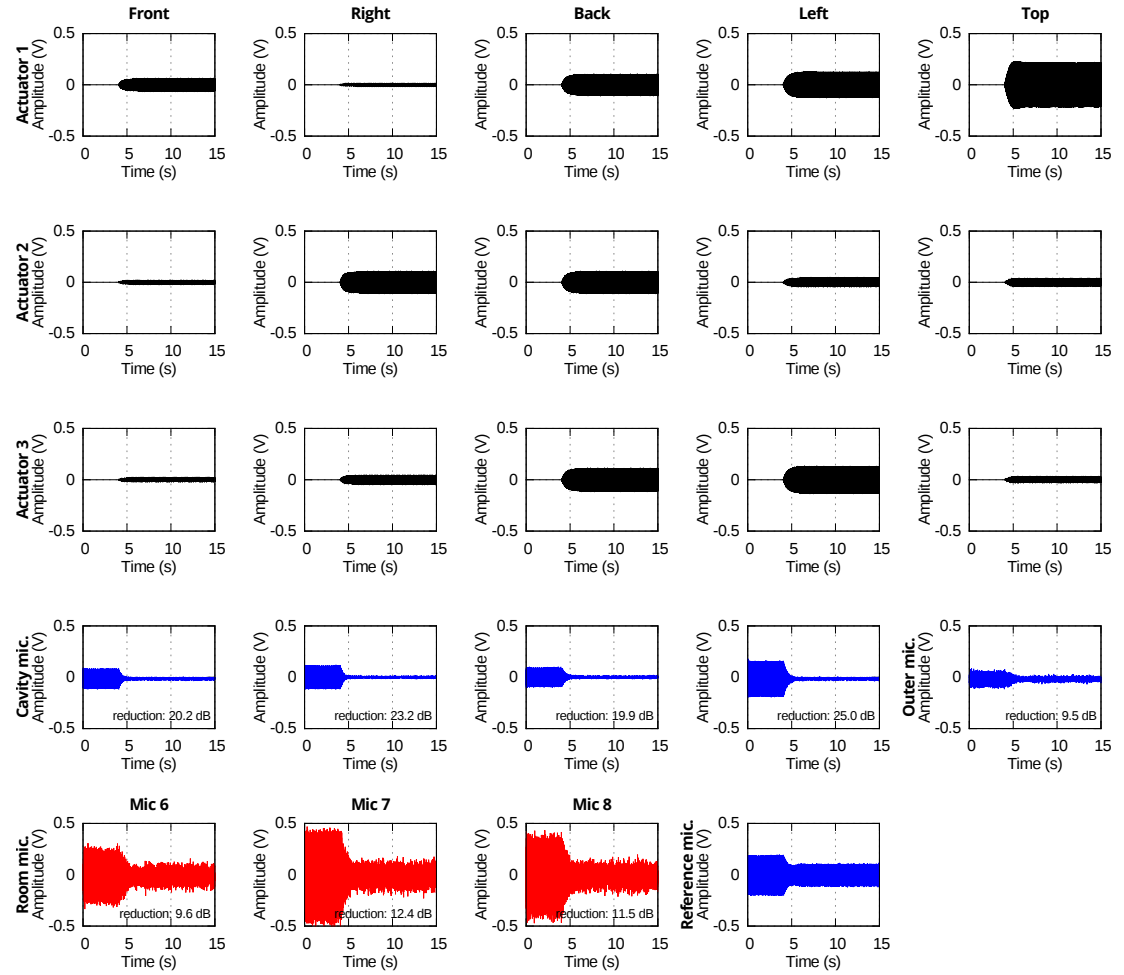


Figure 6.2: Time plots for the experiment performed for primary disturbance of 96 Hz and double-panel casing with ASAC algorithm. Microphones placed in cavities of the side walls and the outer top microphone were used as error sensors.

### 6.3.2 Experiments results and discussion

Results of an exemplary experiment for the frequency of the primary disturbance equal 96 Hz are shown in the time domain in Fig. 6.2. Initial three rows present control signals, where the convergence rate can be observed. In the fourth row, signals measured by microphones used in this experiment as error sensors are presented. In the fifth row of the figure, signals measured by three room microphones are given. The reference microphone measurement is also shown for completeness.

In Figs. 6.3-6.7, frequency characteristics of experiments for single- or double-panel structure with different error sensors configurations are presented. In the last rows of these figures, the mean reduction obtained at the room microphones is shown. It is considered as the main point for evaluation of active control performance. Remaining plots present variances in dB scale of signals acquired by error sensors and individual room microphones, without (blue) and with (green) control. Additionally, bellow each

individual frequency characteristic, a reduction characteristic is also presented, calculated as a difference between noise level without and with control (reduction is marked with red colour).

Finally, a comparison of mean reduction levels obtained for the single-panel casing with different error sensors configurations is presented in Fig. 6.8. In Fig. 6.9, corresponding reduction levels for double-panel structure are presented.

The employment of outer microphones to obtain error signals offered better performance for single-panel structure than in case of double panels. This is the result

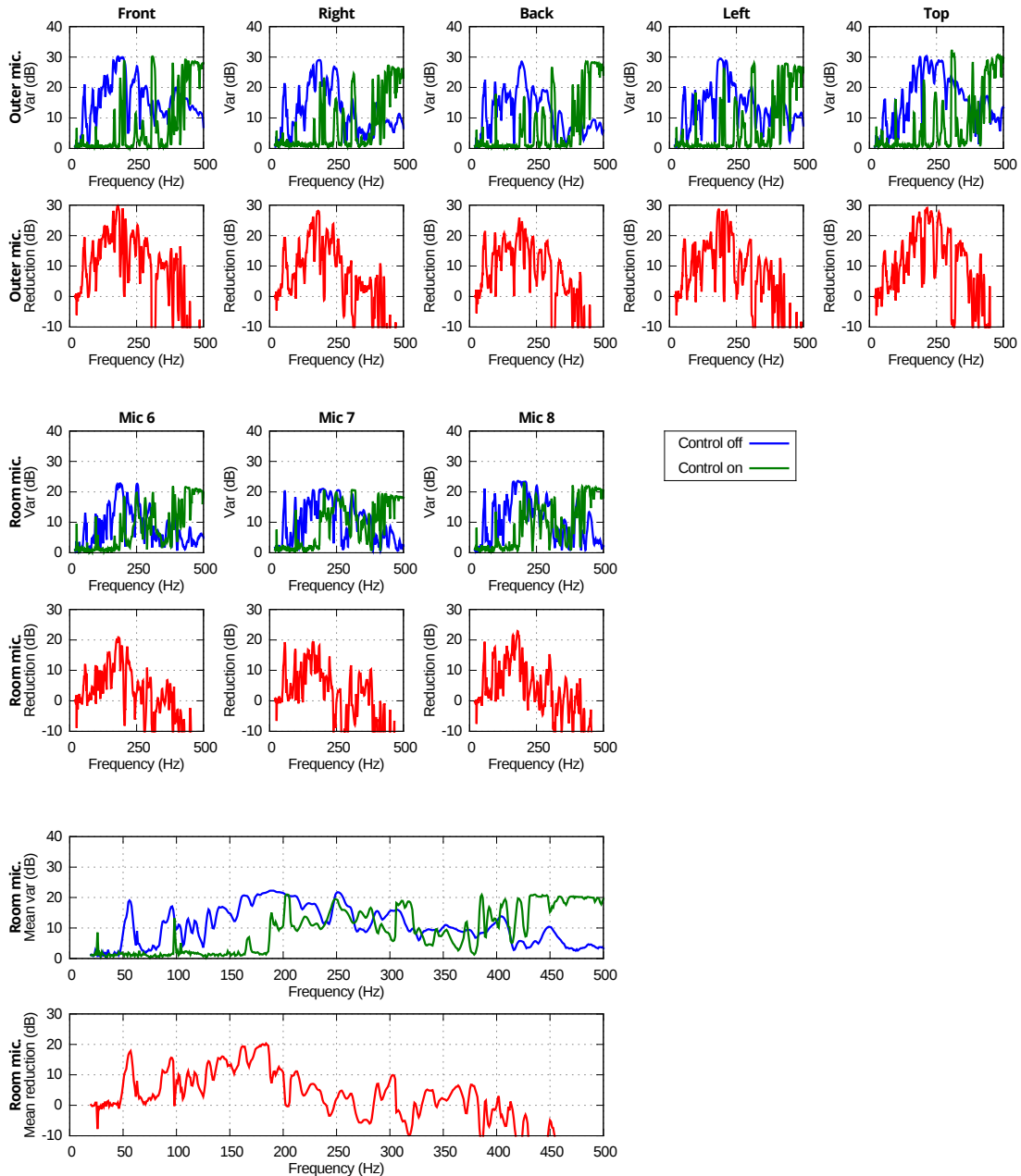


Figure 6.3: Frequency characteristics for the experiment performed for single-panel casing with ASAC algorithm. The outer microphones were used as error sensors.

of actuators mounting on the incident panels. Nevertheless, the double-panel structure introduced higher passive attenuation than single panels, therefore the noise was

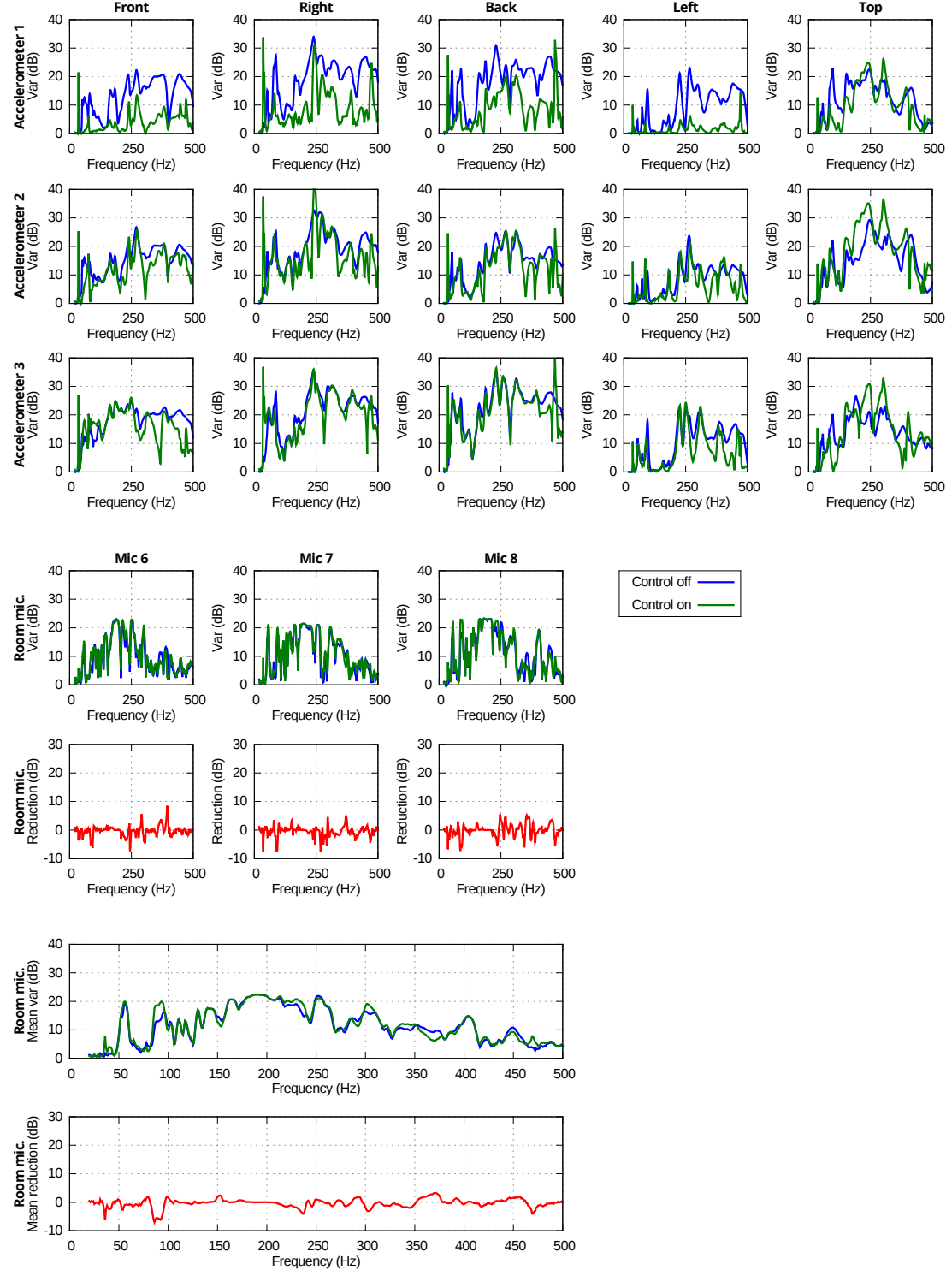


Figure 6.4: Frequency characteristics for the experiment performed for single-panel casing with AVC algorithm. Accelerometers were used as error sensors.

reduced similarly or more, in total. Moreover, the strategy of independent control system for each wall performed well for low frequencies up to 250 Hz, where an impact of vibrations of one wall due to actuators mounted on another wall is significantly weaker, than the impact of actuators mounted directly on the wall. However, above this frequency the cross paths between different walls become significant (see Subsection 2.2.2). Thus, the independent control provides weaker performance than for lower frequencies (even the entire system may become unstable due to the cross couplings).

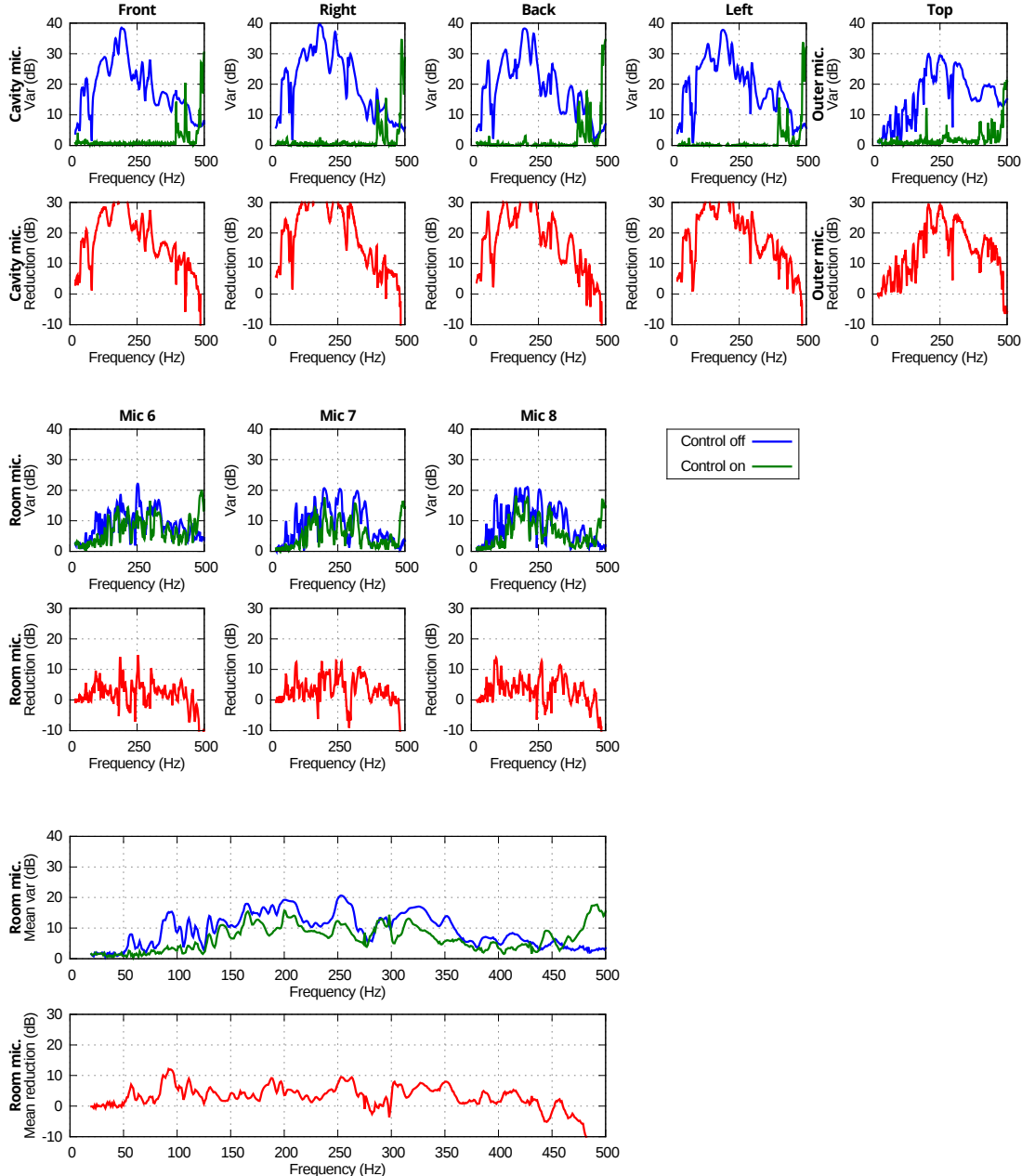


Figure 6.5: Frequency characteristics for the experiment performed for double-panel casing with ASAC algorithm. Microphones placed in cavities of the side walls and the outer top microphone were used as error sensors.

This issue can be mitigated by using more sophisticated strategies, e.g. the switched-error FxLMS algorithm, what is considered in the following Section for the light-weight casing. However, it is noteworthy that generally these strategies require more computational power.

For double-panel casing, the configuration employing cavity microphones as error sensors performed better, than with outer microphones. The control performance was more stable and convergence problems or noise enhancement never occurred until the frequency of 400 Hz (analogous independent control strategy was employed).

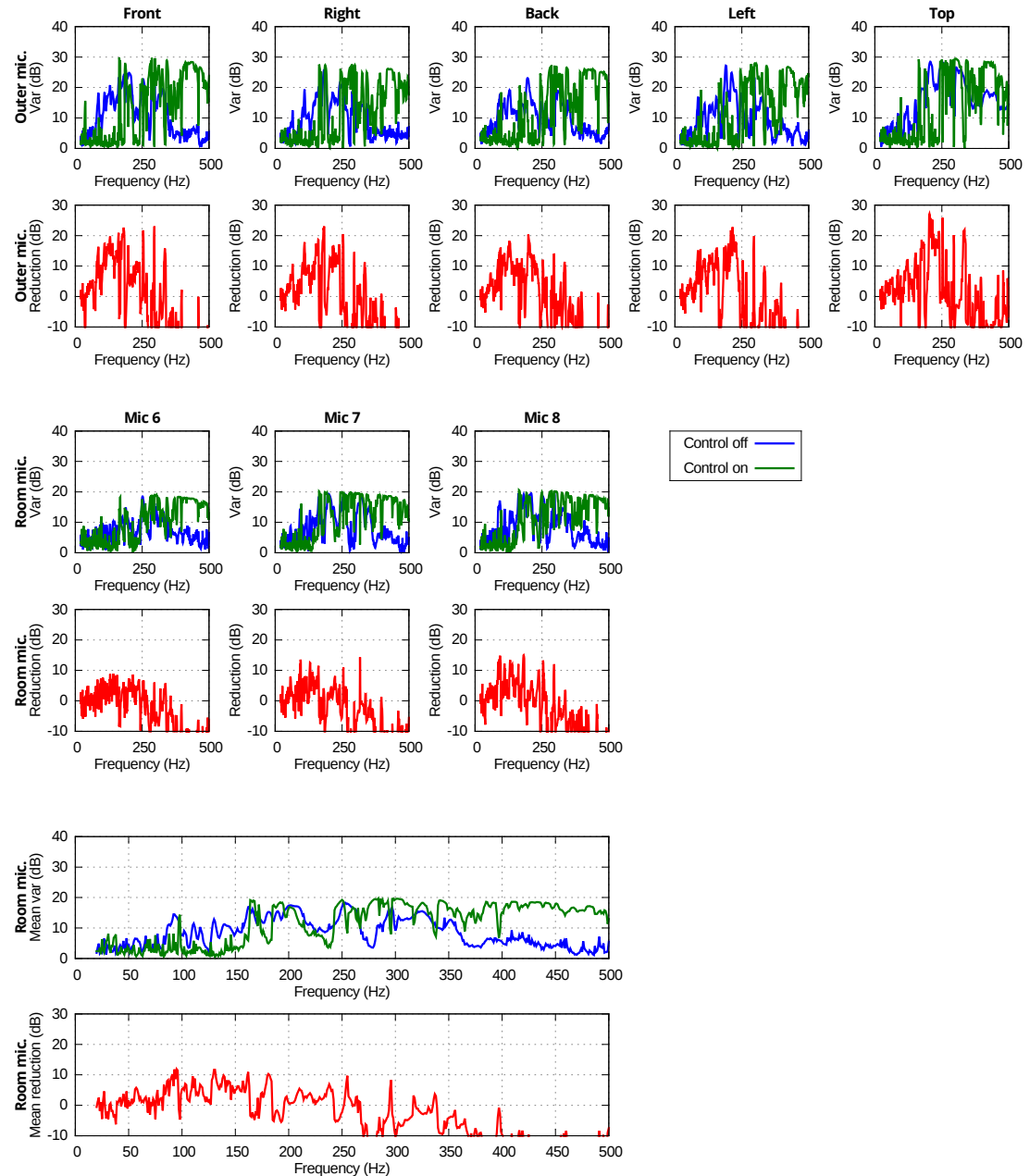


Figure 6.6: Frequency characteristics for the experiment performed for double-panel casing with ASAC algorithm. The outer microphones were used as error sensors.

Moreover, such configuration is more feasible for practical implementation. Usually, users cannot agree to keep error microphones around the casing. Additionally, cavity microphones can operate with lesser gain, than outer microphones. Hence, they are

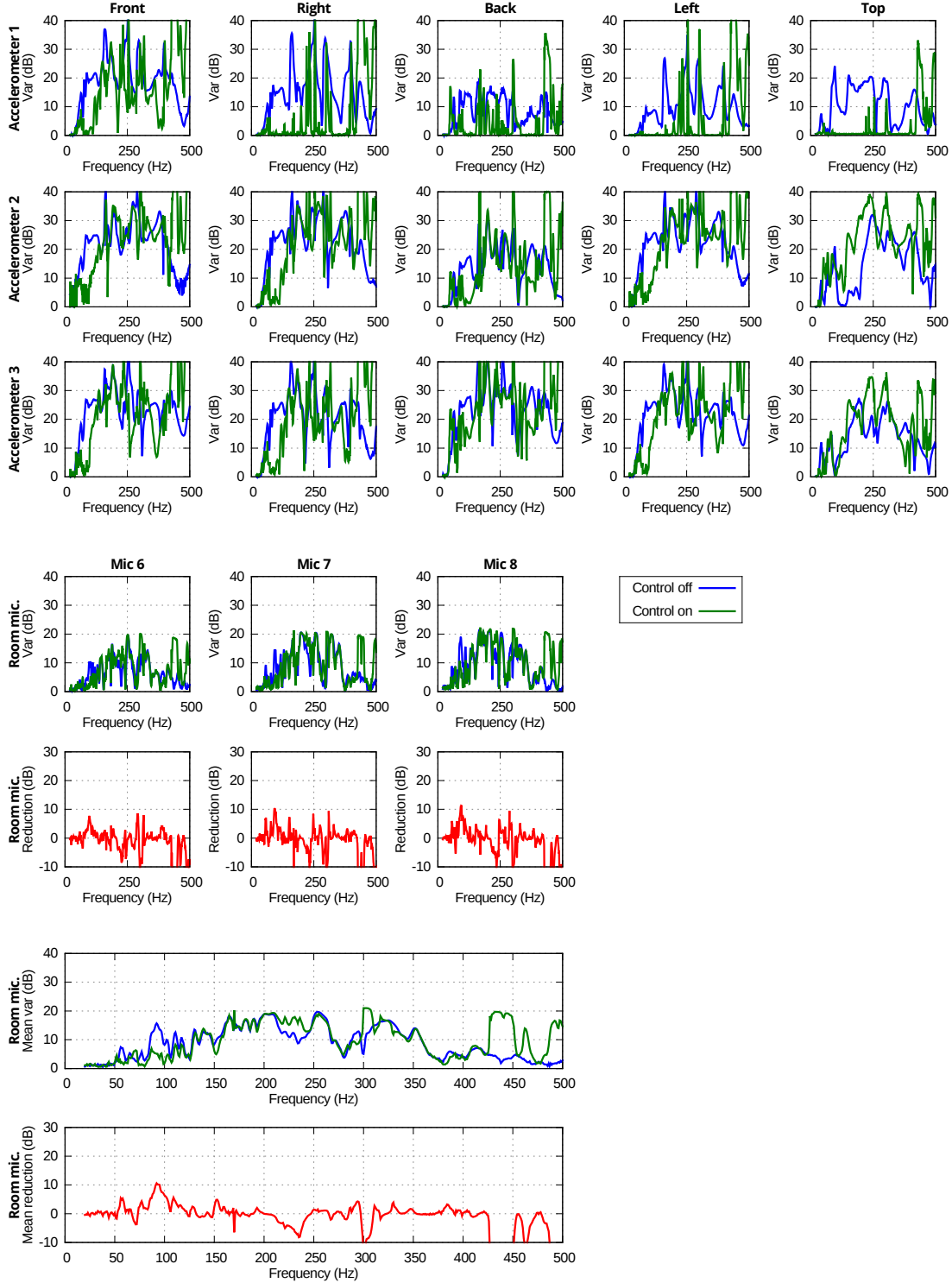


Figure 6.7: Frequency characteristics for the experiment performed for double-panel casing with AVC algorithm. Accelerometers were used as error sensors.

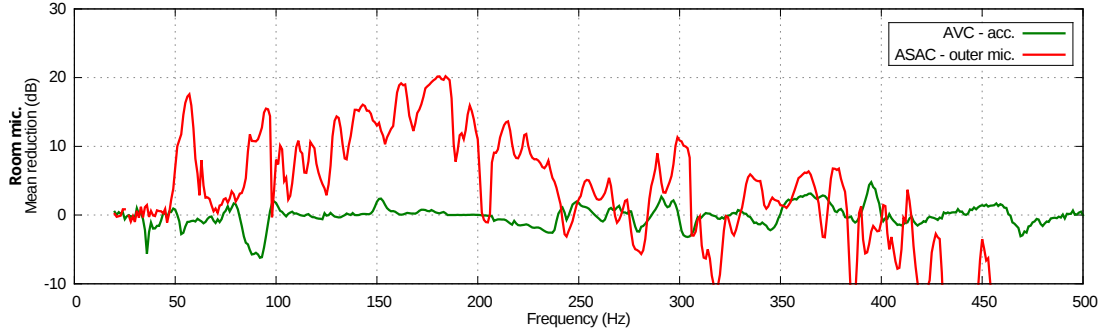


Figure 6.8: Comparison of mean reduction measured by room microphones. Frequency characteristics for experiments performed for single-panel casing.

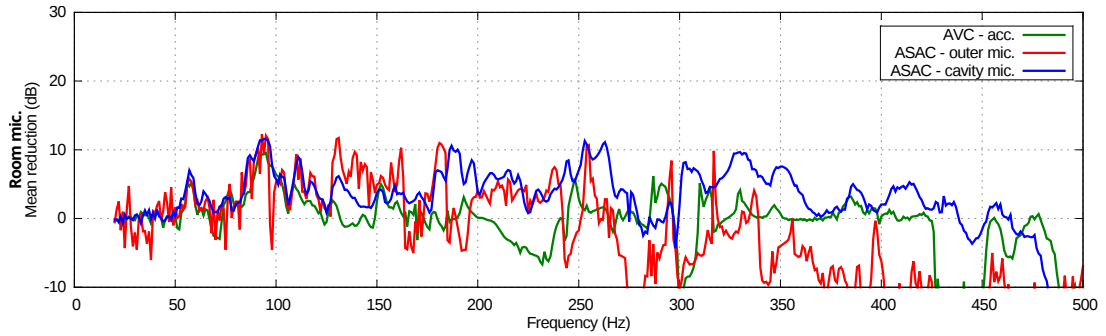


Figure 6.9: Comparison of mean reduction measured by room microphones. Frequency characteristics for experiments performed for double-panel casing.

less vulnerable to external disturbances. Therefore, for double-panel structures cavity microphones are more recommended as error sensors than the outer microphones. Additionally, the switched-error FxLMS algorithm can also be employed with cavity microphones to extend further the operating frequency range.

The performance of configurations using accelerometers to obtain error signals was generally inferior to those using microphones (if the signals are used directly, without any modification). Such approach is efficient in reducing vibrations, but it does not necessarily imply that the noise is reduced most efficiently. However, the Virtual Microphone Control (VMC) approach can be used to appropriately pre-process the error signals obtained by accelerometers to improve noise reduction (Mazur and Pawelczyk, 2016b). Alternatively, other piezoelectric sensors can be applied.

## 6.4 Active control of the light-weight casing

In this Section, the light-weight is evaluated with active control experiments. All walls of the casing are controlled to reduce the noise emission. Due to the strong vibrational and acoustical couplings (see Subsection 2.3.3), two control approaches are evaluated. Firstly, each wall of the casing is controlled separately (analogously as for the rigid casing). Secondly, the switched-error modification is introduced to mitigate the negative influence of cross couplings.

### 6.4.1 Experiments description

The control system uses twenty one inertial actuators (four per front, right, back and left wall, and five for the top wall). The error signal is obtained by the outer microphones. The primary disturbance is generated by a loudspeaker enclosed in the casing. It is a tonal signal of frequency incremented by 4 Hz in the range from 1 Hz to 500 Hz. The considered frequency range includes the low frequencies where the

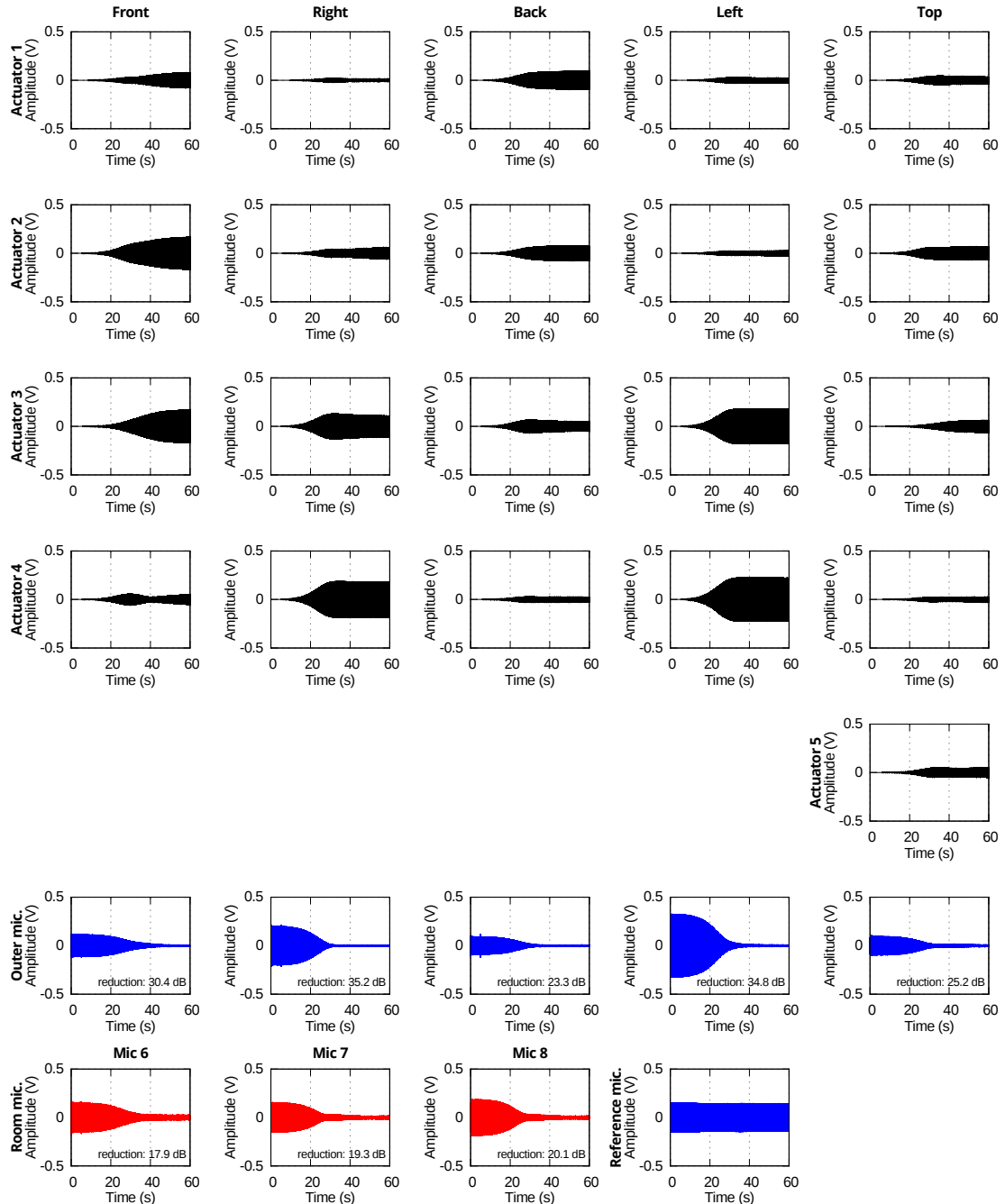


Figure 6.10: Time plots for the experiment performed for primary disturbance of 129 Hz and light-weight casing with ASAC-SE algorithm. The outer microphones were used as error sensors.

speaker starts to transmit sound, up to higher frequencies (above 250 Hz) where the cross-paths between different walls become significant, thus the independent control provides weaker performance than for lower frequencies (even the entire system may become unstable). However, this issue is again mitigated using the switched-error FxLMS algorithm.

The control performance is evaluated by noise reduction level observed by the room microphones. For each frequency of the primary disturbance, a 25 seconds or 60 seconds experiment was performed, for the ASAC and ASAC-SE algorithms, respectively.

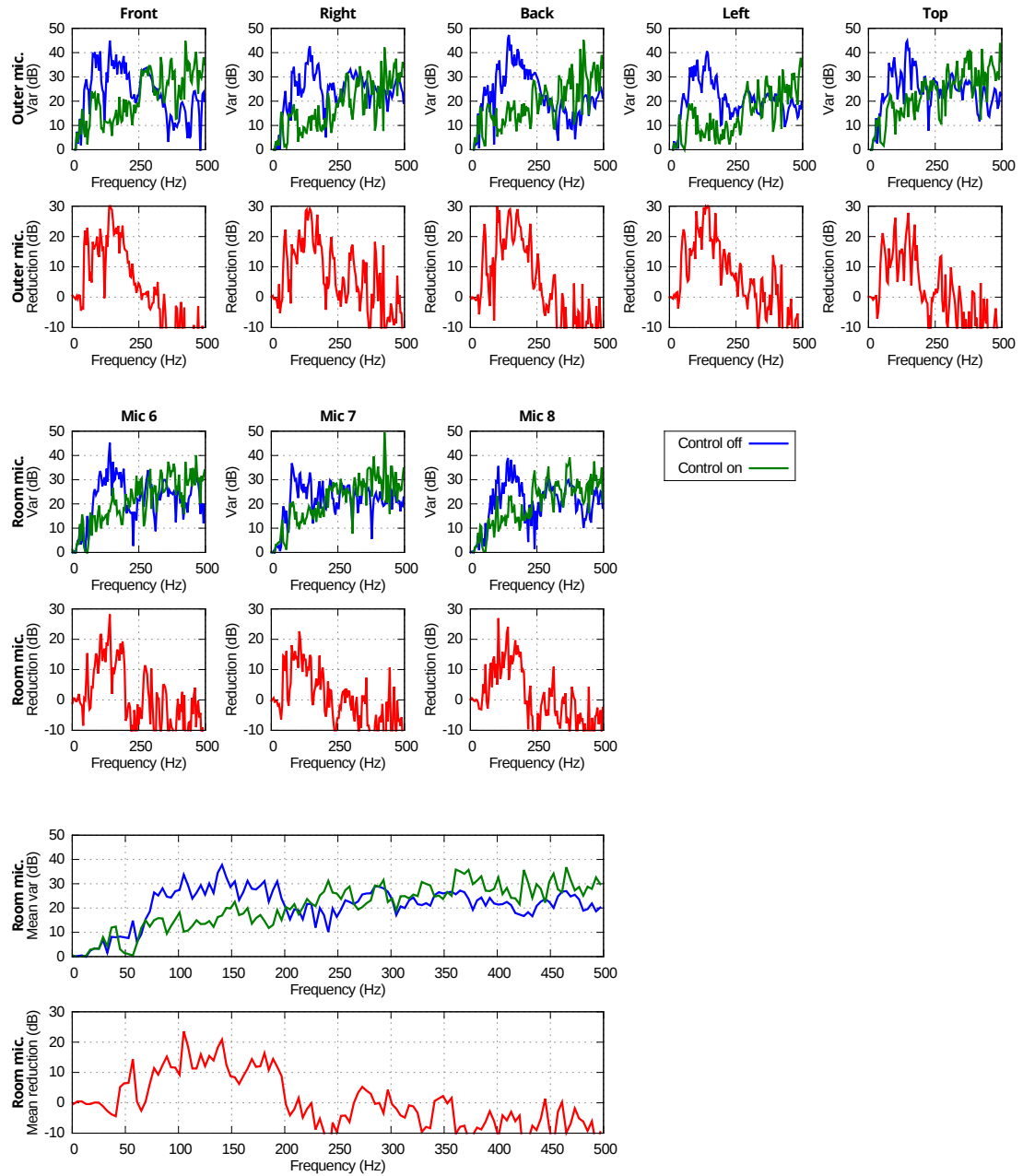


Figure 6.11: Frequency characteristics for the experiment performed for light-weight casing with ASAC algorithm. The outer microphones were used as error sensors.

During its initial 5 seconds the active control was off, and variance of the signal acquired by different sensors was estimated. Then, active control was turned on. When the control algorithm converged, final 5 seconds of the experiment were used to estimate the variance of the signal acquired by corresponding sensors.

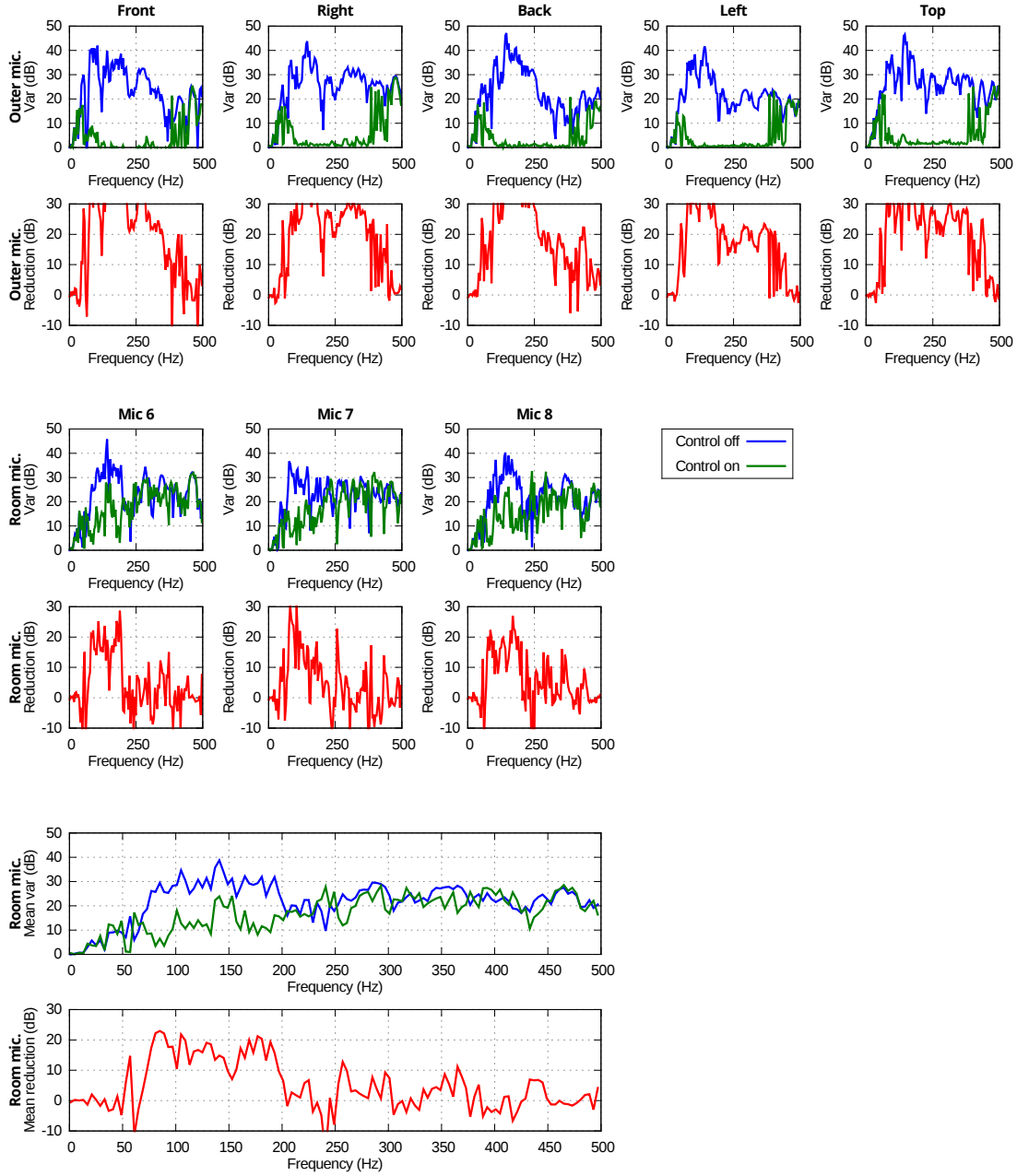


Figure 6.12: Frequency characteristics for the experiment performed for light-weight casing with ASAC-SE algorithm. The outer microphones were used as error sensors.

### 6.4.2 Experiments results and discussion

Results in the time domain of an exemplary experiment for the ASAC-SE algorithm and the frequency of primary disturbance equal 129 Hz are presented in Fig. 6.10 (time-domain results for ASAC algorithm are omitted as they are analogous to those presented in Fig. 6.2). First five rows present control signals, where the convergence rate can be observed. In the sixth row, signals measured by outer microphones used in this experiment as error sensors are shown. In the seventh row of the Figure, signals measured by three room microphones are presented. The reference microphone measurement is also shown for completeness.

In Fig. 6.11 and Fig. 6.12 frequency characteristics of experiments performed with the ASAC and ASAC-SE algorithms are presented. In the last rows of these figures, the mean reduction obtained at the room microphones is shown. It is considered as the main point for evaluation of active control performance. Remaining plots present variances in dB scale of signals acquired by error sensors and individual room microphones, without (blue) and with (green) control. Additionally, below each individual frequency characteristic, a reduction characteristic is also presented, calculated as a difference between noise level without and with control (reduction is marked with red colour). Finally, a comparison of mean reduction levels obtained for the ASAC and ASAC-SE algorithms is presented in Fig. 6.13.

The ASAC algorithm performed well for low frequencies (up to 250 Hz), where the impact of vibrations of one wall due to actuators mounted on another wall is significantly weaker than the impact of actuators mounted directly on the wall. Its performance was reliable and noise enhancement or convergence problems never occurred. Hence, given control strategy achieve significant global noise reduction, with relatively low complexity of the system and high convergence speed, where each wall is controlled separately. However, for frequencies above 250 Hz, the cross-paths between different walls become significant, and hence the independent control provides weaker performance (even the entire system may become unstable). This issue, however, is mitigated by using the ASAC-SE algorithm.

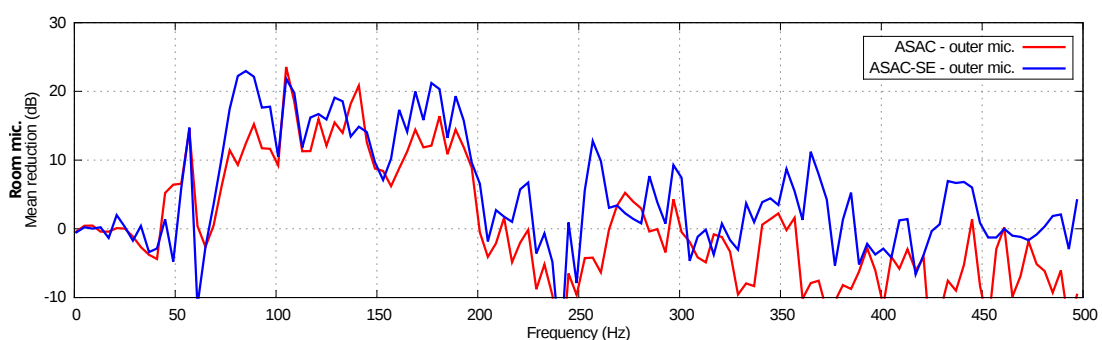


Figure 6.13: Comparison of mean reduction measured by room microphones. Frequency characteristics for experiments performed for light-weight casing.

The ASAC-SE algorithm performed very well for frequencies up to approximately 400 Hz. Beside lowest frequencies, where the inertial actuators were lacking power, the noise at error microphones was reduced to the noise floor level. Above the frequency of 400 Hz the noise reduction was weaker, however, noise enhancement at error microphones practically never occurred. It is also noteworthy to assess noise reduction observed by the room microphones. Although the noise reduction levels were generally better for the ASAC-SE algorithm than for control algorithm without the SE modification, the frequency band of highest global noise reduction was practically the same. One of the plausible reasons is that the arrangement of outer microphones with relation to the wave lengths of the primary disturbance limited the frequency band of the global effect of noise reduction. Hence, more sensors or distributed sensors should be evaluated in the future to extend the frequency band.

## 6.5 Summary

In this Chapter, the active control experimental results have been presented for the developed structures. Initially, the rigid casing has been evaluated for single- and double-panel configurations. Different sensors have been employed to provide the error signals. Then, the light-weight casing has been examined, utilizing the previous experiences to properly configure the control system.

High levels of reduction are obtained, exceeding even 20 dB of mean noise reduction, what confirms high practical potential of the developed active control approach. What is noteworthy, the global noise reduction is obtained (in a whole room). The reduction levels vary in different locations, but usually in a range of several decibels, and zones of noise enhancement never occur.

Examining different active control techniques, a set of recommendations has been formulated for efficient implementation of the active casing approach.

# Chapter 7

## Summary

### 7.1 Conclusions

This dissertation describes the development of an active casing method, as an efficient technique to reduce excessive noise generated by devices and machinery. The research is focused on achieving global noise reduction instead of local zones of quiet. The topics cover a wide range of aspects, varying from the mathematical modelling of the device casing to the practical implementation of an adaptive multi-channel active control system.

Firstly, the laboratory setup for active control experiments consisting of several different device casings has been discussed. To graduate the complexity, initially a rigid casing has been examined, which limits the cross couplings between walls. Then, a light-weight casing has been considered, characterized with strong vibrational coupling between the casing walls. The discussion includes practical application-related aspects of the laboratory stand assembly, vibroacoustic analysis of the introduced structures and selection of sensors and actuators for the active control systems.

The mathematical model of the device casing walls has been developed and experimentally validated for a wide range of cases. The model, although based on available theories, unifies the mathematical formulation of various aspects that were dealt with separately in earlier works available in the literature. These include thin and thick plate theory, elastically restrained boundary conditions, structural thermoelastic damping model, and additional elements mounted to the casing surface—masses, ribs, actuators and sensors. They are integrated in a feasible state space model form, which facilitates further analysis and numerical simulation. In addition, a method of identification of model boundary conditions has been proposed and practically evaluated.

The developed model has been widely used for a series of optimization problems. The memetic algorithm has been employed as an effective optimization algorithm for problems with complex search spaces and multiple optima. It has been used starting with finding efficient locations for actuators and sensors based on controllability and observability measures. Then, a frequency response shaping method of casing walls has been proposed. It has been validated for a set of passive and active control scenarios, including both simulation and a laboratory experiment.

Finally, utilizing the previous analysis and considerations, the developed structures have been used to perform active control experiments. Initially, the rigid casing has been evaluated for single- and double-panel configurations. Different sensors have been employed to provide the error signals. Then, the light-weight casing has been examined, utilizing the previous experiences to properly configure the control system. High levels of reduction have been obtained, exceeding even 20 dB of global noise reduction, what confirms high practical potential of the developed active control approach. Examining different active control techniques, a set of recommendations has been formulated for efficient implementation of the active casing approach.

## 7.2 Author's contribution

The author believes that his contributions are the following:

- Formulation of the mathematical model of the device casing wall, integrating thin and thick plate theory, elastically restrained boundary conditions, structural thermoelastic damping model, and additional elements mounted to the casing surface—masses, ribs, actuators and sensors.
- Development of optimization method for an arrangement of inertial excitors and accelerometers on the device casing surface, utilizing the developed model.
- Development of optimization method for a vibrating structure—development of a frequency response shaping method of a casing wall, according to precisely defined demands.
- Development of identification method of developed model parameters, based on experimental measurements and optimization algorithm.
- Application, real-time implementation, tuning and analysis of adaptive multi-channel active control systems for various device casings, involving simultaneous active control of multiple walls of a casing.

## 7.3 Active casing project and motivation for future research

The presented research is a part of a project entitled "Active reduction of device acoustic noise by controlling vibration of the device casing", supported by the National Science Centre, Poland, decision no. DEC-2012/07/B/ST7/01408. Besides the topics presented in this dissertation, other problem have been also undertaken in the project:

- mathematical modelling of whole device casings, including acoustic field in the enclosure and vibrational couplings between walls;
- analysis of controllability and observability of the obtained active casing models;

- synthesis and analysis of adaptive control algorithms, including stability and convergence analysis;
- synthesis and analysis of control algorithms based on soft computing methods, including artificial neural networks and fuzzy inference system;
- development of passive and semi-active control methods utilizing shunt circuits.

The conclusions following from the presented research motivate to continue the work and develop further the active casing method. A natural continuation is to apply this approach to a real device. Considering the complexity of the vibrating structure, it would be referred to as the third stage of the research (after the rigid casing and the light-weight casing). An example of a real device casing is already under preparation—a common washing machine. There is a number of problems to undertake, among others:

- mathematical modelling of real casing walls with its irregularities (e.g. embossing, internal supports, etc.);
- optimization of the structure, including passive control by frequency response shaping method, and sensors/actuators arrangement optimization for active control purpose;
- synthesis of control algorithms for a real device, e.g. with adaptation to different phases of the device operations.

Each of them constitutes a serious challenge. But they also motivate for further research in the field of active methods to achieve global noise reduction.



# Appendix A

## Stiffness matrix elements

The elements of submatrices of  $\mathbf{K}_p$ ,  $\mathbf{K}_b$  and  $\mathbf{K}_r$  defined in (3.34) are given in this Appendix.

The elements of  $\mathbf{K}_p$  can be derived as:

$$K_{pcc,ij} = \int_0^1 \int_0^1 \left\{ \frac{b}{a} \kappa_x h G_{xz} \left( \frac{\partial \phi_i}{\partial \xi} \frac{\partial \phi_j}{\partial \xi} \right) + \frac{a}{b} \kappa_y h G_{yz} \left( \frac{\partial \phi_i}{\partial \eta} \frac{\partial \phi_j}{\partial \eta} \right) \right\} d\xi d\eta , \quad (\text{A.1a})$$

$$K_{pcd,ij} = \int_0^1 \int_0^1 \left\{ b \kappa_x h G_{xz} \left( \frac{\partial \phi_i}{\partial \xi} \psi_{x,j} \right) \right\} d\xi d\eta , \quad (\text{A.1b})$$

$$K_{pce,ij} = \int_0^1 \int_0^1 \left\{ a \kappa_y h G_{yz} \left( \frac{\partial \phi_i}{\partial \eta} \psi_{y,j} \right) \right\} d\xi d\eta , \quad (\text{A.1c})$$

$$K_{pdd,ij} = \int_0^1 \int_0^1 \left\{ \frac{b}{a} D_x \left( \frac{\partial \psi_{x,i}}{\partial \xi} \frac{\partial \psi_{x,j}}{\partial \xi} \right) + \frac{a}{b} D_{xy} \left( \frac{\partial \psi_{x,i}}{\partial \eta} \frac{\partial \psi_{x,j}}{\partial \eta} \right) + ab \kappa_x h G_{xz} (\psi_{x,i} \psi_{x,j}) \right\} d\xi d\eta , \quad (\text{A.1d})$$

$$K_{pde,ij} = \int_0^1 \int_0^1 \left\{ \frac{1}{2} (D_x \nu_y + D_y \nu_x) \left( \frac{\partial \psi_{x,i}}{\partial \xi} \frac{\partial \psi_{y,j}}{\partial \eta} \right) + D_{xy} \left( \frac{\partial \psi_{x,i}}{\partial \eta} \frac{\partial \psi_{y,j}}{\partial \xi} \right) \right\} d\xi d\eta , \quad (\text{A.1e})$$

$$K_{pee,ij} = \int_0^1 \int_0^1 \left\{ \frac{a}{b} D_y \left( \frac{\partial \psi_{y,i}}{\partial \eta} \frac{\partial \psi_{y,j}}{\partial \eta} \right) + \frac{b}{a} D_{xy} \left( \frac{\partial \psi_{y,i}}{\partial \xi} \frac{\partial \psi_{y,j}}{\partial \xi} \right) + ab \kappa_y h G_{yz} (\psi_{y,i} \psi_{y,j}) \right\} d\xi d\eta , \quad (\text{A.1f})$$

$$i = 1, 2, \dots, N , \quad j = 1, 2, \dots, N .$$

The elements of  $\mathbf{K}_b$  can be derived as:

$$\begin{aligned} K_{bcc,ij} &= b \int_0^1 \left\{ k_{tx0} (\phi_i \phi_j) \Big|_{\xi=0} + k_{tx1} (\phi_i \phi_j) \Big|_{\xi=1} \right\} d\eta \\ &\quad + a \int_0^1 \left\{ k_{ty0} (\phi_i \phi_j) \Big|_{\eta=0} + k_{ty1} (\phi_i \phi_j) \Big|_{\eta=1} \right\} d\xi , \end{aligned} \quad (\text{A.2a})$$

$$K_{bdd,ij} = b \int_0^1 \left\{ k_{rx0} (\psi_{x,i} \psi_{x,j}) \Big|_{\xi=0} + k_{rx1} (\psi_{x,i} \psi_{x,j}) \Big|_{\xi=1} \right\} d\eta \quad (\text{A.2b})$$

$$K_{bee,ij} = a \int_0^1 \left\{ k_{ry0} (\psi_{y,i} \psi_{y,j}) \Big|_{\eta=0} + k_{ry1} (\psi_{y,i} \psi_{y,j}) \Big|_{\eta=1} \right\} d\xi \quad (\text{A.2c})$$

$$i = 1, 2, \dots, N, \quad j = 1, 2, \dots, N.$$

The elements of  $\mathbf{K}_r$  can be derived as:

$$K_{rcr,ij} = \sum_{r=0}^{N_r} \left\{ \frac{G_{r,i} A_{r,i}}{\beta_{r,i}} \int_{\xi_{r0,i}}^{\xi_{r1,i}} \left[ \frac{\cos \alpha_i}{a} \left( \frac{\partial \phi_i}{\partial \xi} \frac{\partial \phi_j}{\partial \xi} \right) + \frac{a \sin^2 \alpha_i}{b^2 \cos \alpha_i} \left( \frac{\partial \phi_i}{\partial \eta} \frac{\partial \phi_j}{\partial \eta} \right) \right. \right. \\ \left. \left. + \frac{\sin \alpha_i}{b} \left( \frac{\partial \phi_i}{\partial \xi} \frac{\partial \phi_j}{\partial \eta} + \frac{\partial \phi_i}{\partial \eta} \frac{\partial \phi_j}{\partial \xi} \right) \right] \Big|_{\eta=g_{r,i}(\xi)} d\xi \right\} \quad (\text{A.3a})$$

$$K_{rcd,ij} = \sum_{r=0}^{N_r} \left\{ \frac{G_{r,i} A_{r,i}}{\beta_{r,i}} \int_{\xi_{r0,i}}^{\xi_{r1,i}} \left[ \cos \alpha_i \left( \frac{\partial \phi_i}{\partial \xi} \psi_{x,j} \right) + \frac{a \sin \alpha_i}{b} \left( \frac{\partial \phi_i}{\partial \eta} \psi_{x,j} \right) \right] \Big|_{\eta=g_{r,i}(\xi)} d\xi \right\} \quad (\text{A.3b})$$

$$K_{rce,ij} = \sum_{r=0}^{N_r} \left\{ \frac{G_{r,i} A_{r,i}}{\beta_{r,i}} \int_{\xi_{r0,i}}^{\xi_{r1,i}} \left[ \sin \alpha_i \left( \frac{\partial \phi_i}{\partial \xi} \psi_{y,j} \right) + \frac{a \sin^2 \alpha_i}{b \cos \alpha_i} \left( \frac{\partial \phi_i}{\partial \eta} \psi_{y,j} \right) \right] \Big|_{\eta=g_{r,i}(\xi)} d\xi \right\} \quad (\text{A.3c})$$

$$K_{rdd,ij} = \sum_{r=0}^{N_r} \left\{ \frac{G_{r,i} A_{r,i}}{\beta_{r,i}} \int_{\xi_{r0,i}}^{\xi_{r1,i}} [a \cos \alpha_i (\psi_{x,i} \psi_{x,j})] \Big|_{\eta=g_{r,i}(\xi)} d\xi \right. \\ \left. + E_{r,i} I_{r,i} \int_{\xi_{r0,i}}^{\xi_{r1,i}} \left[ \frac{\cos^3 \alpha_i}{a} \left( \frac{\partial \psi_{x,i}}{\partial \xi} \frac{\partial \psi_{x,j}}{\partial \xi} \right) + \frac{a \sin^2 \alpha_i \cos \alpha_i}{b^2} \left( \frac{\partial \psi_{x,i}}{\partial \eta} \frac{\partial \psi_{x,j}}{\partial \eta} \right) \right. \right. \\ \left. \left. + \frac{\cos^2 \alpha_i \sin \alpha_i}{b} \left( \frac{\partial \psi_{x,i}}{\partial \xi} \frac{\partial \psi_{x,j}}{\partial \eta} + \frac{\partial \psi_{x,i}}{\partial \eta} \frac{\partial \psi_{x,j}}{\partial \xi} \right) \right] \Big|_{\eta=g_{r,i}(\xi)} d\xi \right. \\ \left. + G_{r,i} J_{r,i} \int_{\xi_{r0,i}}^{\xi_{r1,i}} \left[ \frac{\sin^2 \alpha_i \cos \alpha_i}{a} \left( \frac{\partial \psi_{x,i}}{\partial \xi} \frac{\partial \psi_{x,j}}{\partial \xi} \right) + \frac{a \sin^4 \alpha_i}{b^2 \cos \alpha_i} \left( \frac{\partial \psi_{x,i}}{\partial \eta} \frac{\partial \psi_{x,j}}{\partial \eta} \right) \right. \right. \\ \left. \left. + \frac{\sin^3 \alpha_i}{b} \left( \frac{\partial \psi_{x,i}}{\partial \xi} \frac{\partial \psi_{x,j}}{\partial \eta} + \frac{\partial \psi_{x,i}}{\partial \eta} \frac{\partial \psi_{x,j}}{\partial \xi} \right) \right] \Big|_{\eta=g_{r,i}(\xi)} d\xi \right\} \quad (\text{A.3d})$$

$$\begin{aligned}
K_{rde,ij} = \sum_{r=0}^{N_r} & \left\{ \frac{G_{r,i}A_{r,i}}{\beta_{r,i}} \int_{\xi_{r0,i}}^{\xi_{r1,i}} [a \sin \alpha_i (\psi_{x,i} \psi_{y,j})] \Big|_{\eta=g_{r,i}(\xi)} d\xi \right. \\
& + (E_{r,i}I_{r,i} - G_{r,i}J_{r,i}) \int_{\xi_{r0,i}}^{\xi_{r1,i}} \left[ \frac{\cos^2 \alpha_i \sin \alpha_i}{a} \left( \frac{\partial \psi_{x,i}}{\partial \xi} \frac{\partial \psi_{y,j}}{\partial \xi} \right) + \frac{a \sin^3 \alpha_i}{b^2} \left( \frac{\partial \psi_{x,i}}{\partial \eta} \frac{\partial \psi_{y,j}}{\partial \eta} \right) \right. \\
& \quad \left. \left. + \frac{\sin^2 \alpha_i \cos \alpha_i}{b} \left( \frac{\partial \psi_{x,i}}{\partial \xi} \frac{\partial \psi_{y,j}}{\partial \eta} + \frac{\partial \psi_{x,i}}{\partial \eta} \frac{\partial \psi_{y,j}}{\partial \xi} \right) \right] \Big|_{\eta=g_{r,i}(\xi)} d\xi \right\} \tag{A.3e}
\end{aligned}$$

$$\begin{aligned}
K_{ree,ij} = \sum_{r=0}^{N_r} & \left\{ \frac{G_{r,i}A_{r,i}}{\beta_{r,i}} \int_{\xi_{r0,i}}^{\xi_{r1,i}} \left[ \frac{a \sin^2 \alpha_i}{\cos \alpha_i} (\psi_{y,i} \psi_{y,j}) \right] \Big|_{\eta=g_{r,i}(\xi)} d\xi \right. \\
& + E_{r,i}I_{r,i} \int_{\xi_{r0,i}}^{\xi_{r1,i}} \left[ \frac{\sin^2 \alpha_i \cos \alpha_i}{a} \left( \frac{\partial \psi_{y,i}}{\partial \xi} \frac{\partial \psi_{y,j}}{\partial \xi} \right) + \frac{a \sin^4 \alpha_i}{b^2 \cos \alpha_i} \left( \frac{\partial \psi_{y,i}}{\partial \eta} \frac{\partial \psi_{y,j}}{\partial \eta} \right) \right. \\
& \quad \left. \left. + \frac{\sin^3 \alpha_i}{b} \left( \frac{\partial \psi_{y,i}}{\partial \xi} \frac{\partial \psi_{y,j}}{\partial \eta} + \frac{\partial \psi_{y,i}}{\partial \eta} \frac{\partial \psi_{y,j}}{\partial \xi} \right) \right] \Big|_{\eta=g_{r,i}(\xi)} d\xi \right. \\
& + G_{r,i}J_{r,i} \int_{\xi_{r0,i}}^{\xi_{r1,i}} \left[ \frac{\cos^3 \alpha_i}{a} \left( \frac{\partial \psi_{y,i}}{\partial \xi} \frac{\partial \psi_{y,j}}{\partial \xi} \right) + \frac{a \sin^2 \alpha_i \cos \alpha_i}{b^2} \left( \frac{\partial \psi_{y,i}}{\partial \eta} \frac{\partial \psi_{y,j}}{\partial \eta} \right) \right. \\
& \quad \left. \left. + \frac{\cos^2 \alpha_i \sin \alpha_i}{b} \left( \frac{\partial \psi_{y,i}}{\partial \xi} \frac{\partial \psi_{y,j}}{\partial \eta} + \frac{\partial \psi_{y,i}}{\partial \eta} \frac{\partial \psi_{y,j}}{\partial \xi} \right) \right] \Big|_{\eta=g_{r,i}(\xi)} d\xi \right\} \tag{A.3f}
\end{aligned}$$

$$i = 1, 2, \dots, N, \quad j = 1, 2, \dots, N.$$



## Appendix B

# Mass matrix elements

The elements of submatrices of  $\mathbf{M}_p$ ,  $\mathbf{M}_m$  and  $\mathbf{M}_r$  defined in (3.36) are given in this Appendix.

The elements of  $\mathbf{M}_p$  can be derived as:

$$M_{pcc,ij} = \int_0^1 \int_0^1 \{ab\rho_p h (\phi_i \phi_j)\} d\xi d\eta , \quad (\text{B.1a})$$

$$M_{pdd,ij} = \int_0^1 \int_0^1 \left\{ \frac{1}{12} ab\rho_p h^3 (\psi_{x,i} \psi_{x,j}) \right\} d\xi d\eta , \quad (\text{B.1b})$$

$$M_{pee,ij} = \int_0^1 \int_0^1 \left\{ \frac{1}{12} ab\rho_p h^3 (\psi_{y,i} \psi_{y,j}) \right\} d\xi d\eta , \quad (\text{B.1c})$$

$$i = 1, 2, \dots, N , \quad j = 1, 2, \dots, N .$$

The elements of  $\mathbf{M}_m$  can be derived as:

$$M_{mcc,ij} = \sum_{k=0}^{N_a} \{m_{a,k} (\phi_i \phi_j)\} \Big|_{\substack{\xi=\xi_{a,k} \\ \eta=\eta_{a,k}}} + \sum_{k=0}^{N_s} \{m_{s,k} (\phi_i \phi_j)\} \Big|_{\substack{\xi=\xi_{s,k} \\ \eta=\eta_{s,k}}} + \sum_{k=0}^{N_m} \{m_{m,k} (\phi_i \phi_j)\} \Big|_{\substack{\xi=\xi_{m,k} \\ \eta=\eta_{m,k}}} , \quad (\text{B.2a})$$

$$M_{mdd,ij} = \sum_{k=0}^{N_a} \{I_{ax,k} (\psi_{x,i} \psi_{x,j})\} \Big|_{\substack{\xi=\xi_{a,k} \\ \eta=\eta_{a,k}}} + \sum_{k=0}^{N_s} \{I_{sx,k} (\psi_{x,i} \psi_{x,j})\} \Big|_{\substack{\xi=\xi_{s,k} \\ \eta=\eta_{s,k}}} + \sum_{k=0}^{N_m} \{I_{mx,k} (\psi_{x,i} \psi_{x,j})\} \Big|_{\substack{\xi=\xi_{m,k} \\ \eta=\eta_{m,k}}} , \quad (\text{B.2b})$$

$$M_{mee,ij} = \sum_{k=0}^{N_a} \{I_{ay,k} (\psi_{y,i} \psi_{y,j})\} \Big|_{\substack{\xi=\xi_{a,k} \\ \eta=\eta_{a,k}}} + \sum_{k=0}^{N_s} \{I_{sy,k} (\psi_{y,i} \psi_{y,j})\} \Big|_{\substack{\xi=\xi_{s,k} \\ \eta=\eta_{s,k}}} + \sum_{k=0}^{N_m} \{I_{my,k} (\psi_{y,i} \psi_{y,j})\} \Big|_{\substack{\xi=\xi_{m,k} \\ \eta=\eta_{m,k}}} , \quad (\text{B.2c})$$

$$i = 1, 2, \dots, N , \quad j = 1, 2, \dots, N .$$

The elements of  $\mathbf{M}_r$  can be derived as:

$$M_{rcc,ij} = \sum_{r=0}^{N_r} \left\{ \frac{A_{r,i}\rho_{r,i}a}{\cos \alpha_i} \int_{\xi_{r0,i}}^{\xi_{r1,i}} (\phi_i \phi_j) \Big|_{\eta=g_{r,i}(\xi)} d\xi \right\} \quad (\text{B.3a})$$

$$M_{rdd,ij} = \sum_{r=0}^{N_r} \left\{ \frac{A_{r,i}\rho_{r,i}k_{r,i}a}{\cos \alpha_i} \int_{\xi_{r0,i}}^{\xi_{r1,i}} (\psi_{x,i} \psi_{x,j}) \Big|_{\eta=g_{r,i}(\xi)} d\xi \right\} \quad (\text{B.3b})$$

$$M_{ree,ij} = \sum_{r=0}^{N_r} \left\{ \frac{A_{r,i}\rho_{r,i}k_{r,i}a}{\cos \alpha_i} \int_{\xi_{r0,i}}^{\xi_{r1,i}} (\psi_{y,i} \psi_{y,j}) \Big|_{\eta=g_{r,i}(\xi)} d\xi \right\} \quad (\text{B.3c})$$

$$i = 1, 2, \dots, N, \quad j = 1, 2, \dots, N.$$

# Bibliography

- Amabili, M., Pellegrini, M., Righi, F., and Vinci, F. (2006). Effect of concentrated masses with rotary inertia on vibrations of rectangular plates. *Journal of sound and vibration*, 295(1):1–12.
- Anderson, B. D. and Moore, J. B. (2007). *Optimal control: linear quadratic methods*. Courier Corporation.
- Barrette, M., Berry, A., and Beslin, O. (2000). Vibration of stiffened plates using hierarchical trigonometric functions. *Journal of Sound and Vibration*, 235(5):727–747.
- Batko, W., Pawlik, P., and Stępień, B. (2015). *Non-classical statistical methods in the uncertainty evaluation in acoustic research and modelling* (in Polish: *Nieklasyczne metody statystyczne w ocenie niepewności w badaniach i modelowaniu akustycznym*). Radom, Wydawnictwo Naukowe Instytutu Technologii Eksplotacji - PIB.
- Bismor, D. (2014). Partial update LMS algorithms in active noise control. In *7th Forum Acusticum, Kraków, Poland*.
- Bismor, D. (2015). Extension of LMS stability condition over a wide set of signals. *International Journal of Adaptive Control and Signal Processing*, 29(5):653–670.
- Bismor, D., Czyz, K., and Ogonowski, Z. (2016). Review and comparison of variable step-size LMS algorithms. *International Journal of Acoustics and Vibration*, 21(1):24–39.
- Burgess, J. C. (1981). Active adaptive sound control in a duct: A computer simulation. *The Journal of the Acoustical Society of America*, 70(3):715–726.
- Carneal, J. P. and Fuller, C. R. (2004). An analytical and experimental investigation of active structural acoustic control of noise transmission through double panel systems. *Journal of Sound and Vibration*, 272(3):749–771.
- Chung, J., Chung, T., and Kim, K. (1993). Vibration analysis of orthotropic mindlin plates with edges elastically restrained against rotation. *Journal of Sound and Vibration*, 163(1):151–163.
- Conover, W. B. and Ringlee, R. J. (1955). Recent contributions to transformer audible noise control. *Transactions of the American Institute of Electrical Engineers. Part III: Power Apparatus and Systems*, 3(74):77–90.
- Craig, R. R. and Kurdila, A. J. (2006). *Fundamentals of structural dynamics*. John Wiley & Sons.

- Crocker, M. J. (2007). *Handbook of noise and vibration control*. John Wiley & Sons.
- Dawe, D. (1978). Finite strip models for vibration of mindlin plates. *Journal of Sound and vibration*, 59(3):441–452.
- Dawe, D. and Roufaeil, O. (1980). Rayleigh-ritz vibration analysis of mindlin plates. *Journal of Sound and Vibration*, 69(3):345–359.
- Dozio, L. (2011). On the use of the trigonometric ritz method for general vibration analysis of rectangular kirchhoff plates. *Thin-Walled Structures*, 49(1):129–144.
- Engel, Z. (2010). From the history of the noise control conference. *Archives of Acoustics*, 35(2):133–144.
- Engel, Z., Makarewicz, G., Morzyński, L., and Zawieska, W. M. (2001). *Metody aktywne redukcji hałasu (in Polish)*. CIOP.
- Engesser, F. (1891). Die knickfestigkeit gerader stäbe. *Zentralblatt der Bauverwaltung*, 11:483–486.
- Fahy, F. J. and Gardonio, P. (2007). *Sound and structural vibration: radiation, transmission and response*. Academic press.
- Fuller, C., Hansen, C., and Snyder, S. (1991). Active control of sound radiation from a vibrating rectangular panel by sound sources and vibration inputs: an experimental comparison. *Journal of Sound and Vibration*, 145(2):195–215.
- Fuller, C. R. (1990). Active control of sound transmission/radiation from elastic plates by vibration inputs: I. analysis. *Journal of Sound and Vibration*, 136(1):1–15.
- Garg, P. (2009). A comparison between memetic algorithm and genetic algorithm for the cryptanalysis of simplified data encryption standard algorithm. *International Journal of Network Security and Its Applications*, 1(1):34–42.
- Goldberg, D. E. et al. (1989). *Genetic algorithms in search optimization and machine learning*, volume 412. Addison-wesley Reading Menlo Park.
- Goldsmith, M. (2012). *Discord: The Story of Noise*. OUP Oxford.
- Hansen, C., Snyder, S., Qiu, X., Brooks, L., and Moreau, D. (2012). *Active control of noise and vibration*. CRC Press.
- IEC 60050-801 (1994). *International Electrotechnical Vocabulary—Chapter 801: Acoustics and Electroacoustics*. International Electrotechnical Commission Central Office, Geneva.
- Jones, J. and Fuller, C. R. (1989). Active control of sound fields in elastic cylinders by multicontrol forces. *AIAA journal*, 27(7):845–852.

- Kaiser, O. E. (2001). *Active control of sound transmission through a double wall structure*. PhD thesis, Technische Wissenschaften ETH Zürich, Nr. 14109.
- Keir, J., Kessissoglou, N. J., and Norwood, C. J. (2005). Active control of connected plates using single and multiple actuators and error sensors. *Journal of Sound and Vibration*, 281(1):73–97.
- Kim, K., Kim, B.-H., Choi, T.-M., and Cho, D.-S. (2012). Free vibration analysis of rectangular plate with arbitrary edge constraints using characteristic orthogonal polynomials in assumed mode method. *International Journal of Naval Architecture and Ocean Engineering*, 4(3):267–280.
- Klamka, J. (2013). Controllability of dynamical systems. a survey. *Bulletin of the Polish Academy of Sciences: Technical Sciences*, 61(2):335–342.
- Koko, T. and Olson, M. (1992). Vibration analysis of stiffened plates by super elements. *Journal of Sound and Vibration*, 158(1):149–167.
- Kowal, J., Pluta, J., Konieczny, J., and Kot, A. (2008). Energy recovering in active vibration isolation system—results of experimental research. *Journal of Vibration and Control*, 14(7):1075–1088.
- Krukowicz, T. (2013). Neural fixed-parameter active noise controller for variable frequency tonal noise. *Neurocomputing*, 121:387–391.
- Kurczyk, S. and Pawelczyk, M. (2015). Nonlinear active noise control using partial-update filtered-s LMS algorithm. In *Methods and Models in Automation and Robotics (MMAR), 20th International Conference on*, pages 823–828.
- Latos, M. (2011). *Active noise reducing earplug with speech signal processing*. PhD thesis, Silesian University of Technology, Gliwice, Poland.
- Leissa, A. W. (1969). Vibration of plates. Technical report, DTIC Document.
- Leleu, S., Abou-Kandil, H., and Bonnassieux, Y. (2001). Piezoelectric actuators and sensors location for active control of flexible structures. *Instrumentation and measurement, IEEE transactions on*, 50(6):1577–1582.
- Leniowska, L. and Mazan, D. (2015). MFC sensors and actuators in active vibration control of the circular plate. *Archives of Acoustics*, 40(2):257–265.
- Leniowska, L. and Rdzanek, W. P. (2014). Acoustic pressure of a freely vibrating circular plate without baffle. *Archives of Acoustics*, 17(3):413–423.
- Liew, K., Xiang, Y., Kitipornchai, S., and Lim, M. (1994). Vibration of rectangular mindlin plates with intermediate stiffeners. *Journal of Vibration and Acoustics*, 116(4):529–535.

- Lin, C.-C. (2014). Effect of noise intensity and illumination intensity on visual performance 1, 2. *Perceptual & Motor Skills*, 119(2):441–454.
- Liu, Z., Lee, H., and Lu, C. (2006). Passive and active interior noise control of box structures using the structural intensity method. *Applied Acoustics*, 67(2):112–134.
- Love, A. E. H. (1888). The small free vibrations and deformation of a thin elastic shell. *Philosophical Transactions of the Royal Society of London*, 179:491–546.
- Lueg, P. (1936). Process of silencing sound oscillations. US Patent 2,043,416.
- Mao, Q. and Pietrzko, S. (2013). *Control of Noise and Structural Vibration*. Springer.
- Mazur, K. (2013). *Active Control of Sound with a Vibrating Plate*. PhD thesis, Silesian University of Technology, Gliwice, Poland.
- Mazur, K. and Pawelczyk, M. (2011). Active noise-vibration control using the filtered-reference LMS algorithm with compensation of vibrating plate temperature variation. *Archives of Acoustics*, 36(1):65–76.
- Mazur, K. and Pawelczyk, M. (2015). Multiple-error adaptive control of an active noise-reducing casing. In *Progress of Acoustics*, pages 701–712. Polish Acoustical Society.
- Mazur, K. and Pawelczyk, M. (2016a). Internal model control for a light-weight active noise-reducing casing. *Archives of Acoustics*, 41(2):315–322.
- Mazur, K. and Pawelczyk, M. (2016b). Virtual microphone control for a light-weight active noise-reducing casing. In *Proceedings of 23th International Congress on Sound and Vibration*.
- Mindlin, R. D. (1951). Influence of rotary inertia and shear on flexural motions of isotropic elastic plates. *Journal of applied mechanics*, 18:31–38.
- Mindlin, R. D., Schacknow, A., and Deresiewicz, H. (1956). Flexural vibrations of rectangular plates. *Journal of Applied Mechanics*, 23(3):430–436.
- Morgan, D. R. (1980). An analysis of multiple correlation cancellation loops with a filter in the auxiliary path. *Acoustics, Speech and Signal Processing, IEEE Transactions on*, 28(4):454–467.
- Morzynski, L. and Makarewicz, G. (2003). Application of neural networks in active noise reduction systems. *International Journal of Occupational Safety and Ergonomics*, 9(3):257–270.
- Nelson, P. A. and Elliott, S. J. (1993). *Active control of sound*. Academic press.
- Neri, F., Cotta, C., and Moscato, P. (2012). *Handbook of memetic algorithms*, volume 379. Springer.

- Nicholson, J. and Bergman, L. (1985). Vibration of thick plates carrying concentrated masses. *Journal of Sound and Vibration*, 103(3):357–369.
- Norris, A. N. and Photiadis, D. M. (2005). Thermoelastic relaxation in elastic structures, with applications to thin plates. *The Quarterly Journal of Mechanics and Applied Mathematics*, 58(1):143–163.
- Olson, H. F. and May, E. G. (1953). Electronic sound absorber. *The Journal of the Acoustical Society of America*, 25(6):1130–1136.
- Olson, M. and Hazell, C. (1977). Vibration studies on some integral rib-stiffened plates. *Journal of Sound and Vibration*, 50(1):43–61.
- Pawelczyk, M. (2002). Feedforward algorithms with simplified plant model for active noise control. *Journal of sound and vibration*, 255(1):77–95.
- Pawelczyk, M. (2004). Adaptive noise control algorithms for active headrest system. *Control Engineering Practice*, 12(9):1101–1112.
- Pawelczyk, M. (2013). *Application-Oriented Design of Active Noise Control Systems*. Academic Publishing House Exit.
- Pawelczyk, M. and Wrona, S. (2013). Optimal placement of actuators for active noise-vibration control with spillover effect suppression using a memetic algorithm. In *Proceedings of 20th International Congress on Sound and Vibration*, Bangkok, Thailand, 7-11 July.
- Pawelczyk, M. and Wrona, S. (2016). Impact of boundary conditions on shaping frequency response of a vibrating plate - modeling, optimization, and simulation. *Procedia Computer Science*, 80:1170–1179.
- Pietrzko, S. (2009). *Contributions to noise and vibration control technology*. Akademia Górnictwo-Hutnicza.
- Preumont, A. (2012). *Vibration control of active structures: an introduction*, volume 50. Springer Science & Business Media.
- Rao, S. S. (2007). *Vibration of continuous systems*. John Wiley & Sons.
- Rdzanek, W. P. (2014). Acoustic radiation of circular plate including the attenuation effect and influence of surroundings. *Archives of Acoustics*, 16(3-4):581–590.
- Rdzanek, W. P. and Witkowski, P. (2014). The sound power of a circular membrane for axially-symmetric vibrations. *Archives of Acoustics*, 17(3):433–438.
- Reddy, J. N. (2006). *Theory and analysis of elastic plates and shells*. CRC press.
- Roure, A. (1985). Self-adaptive broadband active sound control system. *Journal of Sound and Vibration*, 101(3):429–441.

- Stokey, W. and Zorowski, C. (1959). Normal vibrations of a uniform plate carrying any number of finite masses. *J. Appl. Mech.*, 26(2):210–216.
- Talbot-Smith, M. (2013). *Audio engineer's reference book*. Taylor & Francis.
- Timoshenko, S. P. and Woinowsky-Krieger, S. (1959). *Theory of plates and shells*. McGraw-hill.
- Widrow, B. and Stearns, S. D. (1985). *Adaptive signal processing*. Prentice-Hall, Inc.
- Wolf, S. and Stanley, N. (2013). *Wolf and Stanley on environmental law*. Routledge.
- Wrona, S. and Pawelczyk, M. (2013a). Application of an memetic algorithm to placement of sensors for active noise-vibration control. *Mechanics and Control*, 32(3):122–128.
- Wrona, S. and Pawelczyk, M. (2013b). Controllability-oriented placement of actuators for active noise-vibration control of rectangular plates using a memetic algorithm. *Archives of Acoustics*, 38(4):529–536.
- Wrona, S. and Pawelczyk, M. (2014a). Active device casings. In *Proceedings of 40th Winter School of Vibroacoustical Hazards Suppressions*, Gliwice-Szczyrk, Poland, 3-7 March.
- Wrona, S. and Pawelczyk, M. (2014b). Active reduction of device multi-tonal noise by controlling vibration of multiple walls of the device casing. In *Proceedings of 19th International Conference On Methods and Models in Automation and Robotics (MMAR)*, IEEE.
- Wrona, S. and Pawelczyk, M. (2015). Active reduction of device narrowband noise by controlling vibration of its casing based on structural sensors. In *Proceedings of 22nd International Congress on Sound and Vibration*, Florence, Italy, 12-16 July.
- Wrona, S. and Pawelczyk, M. (2016a). Employment of double-panel casing for active reduction of device noise. *Solid State Phenomena*, 248:27–34.
- Wrona, S. and Pawelczyk, M. (2016b). Feedforward control of a light-weight device casing for active noise reduction. *Archives of Acoustics*, 41(3).
- Wrona, S. and Pawelczyk, M. (2016c). Identification of elastic boundary conditions of light-weight device casing walls using experimental data. In *Proceedings of 21st International Conference On Methods and Models in Automation and Robotics (MMAR)*, IEEE, Miedzyzdroje, Poland, 29 August - 1 September.
- Wrona, S. and Pawelczyk, M. (2016d). Optimal placement of actuators for active structural acoustic control of a light-weight device casing. In *Proceedings of 23rd International Congress on Sound and Vibration*, Athens, Greece, 10-14 July.

- Wrona, S. and Pawelczyk, M. (2016e). Shaping frequency response of a vibrating plate for passive and active control applications by simultaneous optimization of arrangement of additional masses and ribs. Part I: Modeling. *Mechanical Systems and Signal Processing*, 70-71:682–698.
- Wrona, S. and Pawelczyk, M. (2016f). Shaping frequency response of a vibrating plate for passive and active control applications by simultaneous optimization of arrangement of additional masses and ribs. Part II: Optimization. *Mechanical Systems and Signal Processing*, 70-71:699–713.
- Wrona, S., Pawelczyk, M., and Wyrwal, J. (2014). Optimal placement of elastically mounted vibration actuators on a plate for active noise-vibration control. In et al., K. M., editor, *Current problems of automatic control and robotics*, pages 465–477. Academic Publishing House EXIT, Warszawa.
- Xing, Y. and Liu, B. (2009). New exact solutions for free vibrations of thin orthotropic rectangular plates. *Composite Structures*, 89(4):567–574.
- Young, D. (1950). Vibration of rectangular plates by the ritz method. *Journal of Applied Mechanics-Transactions of the ASME*, 17(4):448–453.
- Zawieska, W. M. and Rdzanek, W. P. (2007). The influence of a vibrating rectangular piston on the acoustic power radiated by a rectangular plate. *Archives of Acoustics*, 32(2):405–415.
- Zawieska, W. M., Rdzanek, W. P., Rdzanek, W. J., and Engel, Z. (2007). Low frequency estimation for the sound radiation efficiency of some simply supported flat plates. *Acta acustica united with acustica*, 93(3):353–363.



# Index

- accelerometers, 14
- active casing, 5
- Active Noise Control, 3
- Active Structural Acoustic Control, 5
- additional masses, 33, 78
- ANSYS, 43, 52
- ASAC, 97, 107
- ASAC-SE, 98, 107
- AVC, 97
- boundary conditions, 29, 76
  - cavity microphone, 12
  - control filters, 96
  - Controllability, 41
  - cost function, 77, 79
  - double-panel casing, 98
  - elastically restrained boundary conditions, 29
  - evolutionary algorithms, 74
  - feedforward control system, 96
  - Finite Elements Method, 43
  - Finite Impulse Response, 97
  - FIR model, 97
  - free boundary conditions, 29
  - frequency response shaping, 61, 83
  - fully-clamped boundary conditions, 29
  - Gramian matrix, 41
  - incident panel, 10
  - inertial excitors, 12
  - Internal Model Control, 96
  - isotropic plate, 25
- Kirchhoff–Love plate theory, 24
- laser vibrometer, 14
- leakage coefficient, 97
- light-weight casing, 9, 16, 65, 82, 105
- LNFxLMS, 95
- mass matrix, 38
- memetic algorithm, 74
- microphones, 12
- Mindlin–Reissner plate theory, 26
- observability, 41
- orthotropic plate, 26
- outer microphone, 12
- partial update, 97
- primary paths, 96
- radiating panel, 10
- Rayleigh–Ritz method, 36
- reference microphone, 12
- reference path, 96
- reference signal, 96
- ribs, 33, 78
- rigid casing, 9, 55, 80, 98
- room microphones, 12
- secondary paths, 14, 19, 96
- simply-supported boundary conditions, 29
- single-panel casing, 98
- state space model, 39
- step-size, 97
- stiffness matrix, 37
- switched-error, 98
- trial functions, 36
- Virtual Microphone Control, 105